

DE TTK



1949

Top predictions at high precision for the LHC

PhD Thesis
Egyetemi Doktori (PhD) értekezés

Ádám Kardos

Supervisor/Témavezető
Dr. Zoltán Trócsányi
University of Debrecen
PhD School in Physics

Debreceni Egyetem
Természettudományi Doktori Tanács
Fizikai Tudományok Doktori Iskolája
Debrecen, 2012

Ezen értekezést a Debreceni Egyetem Természettudományi Doktori Tanács Fizikai Tudományok Doktori Iskolája Részecskefizika programja keretében készítettem a Debreceni Egyetem természettudományi doktori (PhD) fokozatának elnyerése céljából.

Debrecen, 2012

Kardos Ádám

Tanúsítom, hogy Kardos Ádám doktorjelölt 2009-2012 között a fent megnevezett Doktori Iskola Részecskefizika programjának keretében irányításommal végezte munkáját. Az értekezésben foglalt eredményekhez a jelölt önálló alkotó tevékenységével meghatározóan hozzájárult. Az értekezés elfogadását javasolom.

Debrecen, 2012

Dr. Trócsányi Zoltán
témavezető

Top predictions at high precision for the LHC

Értekezés a doktori (PhD) fokozat megszerzése érdekében
a fizika tudományágban

Írta: Kardos Ádám okleveles fizikus
Készült a Debreceni Egyetem Fizikai Tudományok Doktori Iskolája
Részecskefizika programja keretében

Témavezető: Dr. Trócsányi Zoltán

A doktori szigorlati bizottság:

elnök: Dr.
tagok: Dr.
Dr.

A doktori szigorlat időpontja: 2012

Az értekezés bírálói:

Dr.
Dr.

A bírálóbizottság:

elnök: Dr.
tagok: Dr.
Dr.
Dr.
Dr.

Az értekezés védésének időpontja: 2012

"... We choose to go to the moon in this decade and do the other things, not because they are easy, but because they are hard..."

John F. Kennedy

Acknowledgements

I am grateful to my advisor, Zoltán Trócsányi, who introduced me to particle physics and helped me with all his skillful advices in the past, long years. He taught me so much, and I am still learning. He always tried and succeeded to find me comfortable workplace and environment.

I thank Costas Papadopoulos, my tutor and coauthor who accepted to be my tutor, when I stayed in Athens within the HEPtools program. He gave me help and support in our work.

I thank Giuseppe Bevilacqua, my coauthor and friend, who helped me so much. He taught me a great deal of the HELAC programs and gave me company for so many conversations over various meals.

I thank Maria Vittoria Garzelli, my coauthor and colleague for all those delightful conversations, discussions and arguments, which provided perfect inspiration for work.

I am also grateful to my friends: István Halász, Sándor Nagy and István Nándori for those inspiring professional and not so professional conversations.

Finally, my warmest thanks go to my family, who helped, encouraged and gave me support. They all helped me to enjoy the ups and endure the downs of these years.

I gratefully acknowledge the following financial supports: the LHCPHenoNet network PITN-GA-2010-264564, the Swiss National Science Foundation Joint Research Project SCOPES IZ73Z0 1/28079, the TÁMOP 4.2.1./B-09/1/KONV-2010-0007 and 4.2.2/B-10/1-2010-0024 projects, the Hungarian Scientific Research Fund grant K-101482.

List of Notations

| | |
|---------------------------|---|
| ΔR_{ij} | R separation between particle i and j , $\Delta R_{ij} = \sqrt{\Delta\phi_{ij}^2 + \Delta y_{ij}^2}$ |
| $\Delta(t_1, t_2)$ | Sudakov-form-factor |
| η | Pseudorapidity, $\eta = -\log \tan \theta/2$, where θ is the enclosed angle between the particle and beam direction |
| Γ_t | Top quark width |
| \hat{R} | Real-emission part minus subtraction terms, flux factor included |
| \mathcal{M}_B | Born matrix element |
| \mathcal{M}_R | Real-emission matrix element |
| \mathcal{M}_V | One-loop matrix element |
| μ | Nonphysical-scale, when used $\mu_R = \mu_F = \mu$ |
| Φ_{rad} | One-particle, radiation phase space |
| Φ_B | Born phase space |
| Φ_R | Real-emission phase space |
| A_{FB} | Forward-backward asymmetry |
| $f_{p/H}$ | Parton distribution function for parton type-p in hadron type-H |
| G_{\oplus}, G_{\ominus} | Finite remainders of the integrated initial state collinear counterterms |
| G_F | Fermi-constant |

| | |
|-------------------------|--|
| J_n | Jet function for n partons |
| m_\perp | Transverse mass, $m_\perp = \sqrt{m^2 + p_\perp^2}$ |
| N_c | Number of color charges |
| O | General, physical observable |
| V | Virtual part, containing flux-factor and integrated subtraction terms |
| V_{q_i, q_j} | CKM matrix element |
| y | Rapidity, $y = \frac{1}{2} \log \frac{E+p_z}{E-p_z}$ |
| α_s | Strong coupling |
| \cancel{E}_\perp | Missing transverse energy, $\cancel{E}_\perp = \sqrt{p^2 + p_\perp^2}$, where p is the missing momentum |
| H_\perp | Integer sum of transverse momenta, for definition see Eq. (5.2) |
| m_b | Bottom quark mass |
| m_H | Higgs mass |
| m_t | Top quark mass |
| μ_F | Factorization-scale |
| μ_R | Renormalization-scale |
| m_W | W mass |
| m_Z | Z mass |
| p_\perp | Transverse momentum |
| $p_\perp^{\text{t.c.}}$ | Technical cut in transverse momentum, for details see Sect. 3.1 |
| $p_{\perp, \text{min}}$ | Minimal transverse momentum, used in the definition of the NLO Sudakov-factor, below this value only unresolved emission takes place |
| \cancel{p}_\perp | Missing transverse momentum |
| CKM | Cabibbo Kobayashi Maskawa |

| | |
|-----|------------------------------|
| LHE | Les Houches Event |
| LO | Leading Order |
| NLO | Next to Leading Order |
| PDF | Parton Distribution Function |
| QCD | Quantum ChromoDynamics |
| QFT | Quantum Field Theory |
| SM | Standard Model |

Contents

| | |
|--|-----------|
| I Preliminaries | 1 |
| 1 Introduction | 3 |
| 1.1 Importance of being Top | 6 |
| 2 Methods | 11 |
| 2.1 NLO calculations | 11 |
| 2.2 Parton showers | 19 |
| 2.3 NLO matched parton showers | 22 |
| II Applications | 27 |
| 3 $t\bar{t}+j$ production | 29 |
| 3.1 Implementation and checks | 29 |
| 3.2 Phenomenology | 32 |
| 3.3 Secondary leptons in hadronic final states | 35 |
| 4 $t\bar{t}+H$ production | 43 |
| 4.1 Implementation and checks | 44 |
| 4.2 Phenomenology | 50 |
| 5 $t\bar{t}+Z$ production | 57 |
| 5.1 Implementation and checks | 58 |
| 5.2 NLO predictions for the LHC | 58 |
| 5.3 Phenomenology | 66 |

| | | |
|----------|---|------------|
| 6 | $t\bar{t} + W^\pm$ production | 77 |
| 6.1 | Implementation and checks | 78 |
| 6.2 | Phenomenology | 84 |
| 6.2.1 | Inclusive analysis | 85 |
| 6.2.2 | Trilepton-channel analysis | 89 |
| 6.2.3 | Dilepton-channel analysis | 95 |
| 7 | Summary and outlook | 103 |
| 8 | Magyar nyelvű összefoglaló | 105 |

Part I

Preliminaries

Chapter 1

Introduction

Quantum Chromodynamics (QCD) is the theory of the strong interaction acting between *partons*, the constituents of hadrons. QCD is a quantum field theory of Dirac-fields coupled to a non-Abelian gauge-field. In other words QCD is a consistent quantum field theory of fermions with spin one-half and bosons with spin one. These bosons are the quantum fluctuations of a non-Abelian gauge field. The symmetry group is $SU(N_c)$, where the choice $N_c = 3$ yields remarkable agreement with experiments. Due to the non-Abelian nature of the gauge-field, it also carries a charge (color) and because of this peculiar effect, it is self-interacting. We collectively call the strongly interacting particles partons, the fermions are referred to as *quarks*, while the mediators are called *gluons*. We label gluons by g , while the six different quark flavors are denoted by u, d, c, s, t, b . In nature only the first two flavors can be found in the proton and neutron, all the others can only be observed in high-energy scattering experiments. The mass range of quarks spans more than four orders of magnitude, while the u and d quark masses are in the order of a few MeV, the heaviest quark, the top, has a mass comparable to the mass of a gold atom.

QCD is rooted in the parton model [1], which made its first triumph by explaining the hadron multiplets. In the early 1960's the observed baryons and mesons could be organized into octets and decuplets using strangeness and charge. These structures could have only been explained if three different type of quarks (u , d and s) had been defined such that the baryons were considered as the bound states of three quarks, while mesons were defined as the bound states of quark-antiquark pairs. Although the quark model turned out to explain successfully the hadron

substructure, these constituents were only seen in deep-inelastic-scattering (DIS) of electrons on protons at SLAC. The finite size of the proton was suggested by inelastic electron scattering, as Mott-scattering (electron scattering on a pointlike charge) was unable to describe data. Agreement can be found when finite size effects are taken into account by form factors. The found proton radius turned out to be surprisingly large. Further experiments lead to the conclusion of three pointlike constituents. The parton model could describe the various hadron multiplets and experimental results could be interpreted by it, though it failed to elucidate, for example, the Δ^{++} baryon. It is the bound state of three u quarks with the spin of three-halves. Hence all three quarks seem to be in the same state, and without introducing additional degrees of freedom or quantum numbers, this baryon contradicts to Pauli's exclusion principle, which however should be true for all fermions. This contradiction is resolved by the introduction of color [2, 3]. The colored parton model furnished the ground for QCD, by the knowledge, that quarks are spin one-half fermions with three possible color charges. The quantum field theoretical description became possible.

The running of the coupling, α_s , is governed by the renormalization group equation. In QCD the self-interacting gauge-field, the number of color charges and flavors result in a negative β -function, hence producing asymptotic freedom. If the renormalization scale is denoted by Q , due to asymptotic freedom $\alpha_s(Q^2) \xrightarrow{Q^2 \rightarrow \infty} 0$. This enables QCD to be treated perturbatively at sufficiently high energies, ensured by the smallness of the running coupling.

In an actual experiment such as the ATLAS or CMS at the LHC the highly sophisticated detector apparatus detects hadrons. The initially created highly energetic partons due to their color charge can radiate further partons, just like an electron in the presence of an electromagnetic field creating a radiation cascade. Radiation continues until all the partons reach low energies, where hadronization occurs. Since the radiation produces soft (less energetic) and/or collinear (emitted into the direction of movement of the emitter) partons, collimated hadrons, jets, are observed. Physical observables are assigned for jets. In perturbative QCD we calculate matrix elements at the parton level, which means partons are considered as in-coming¹ and out-going particles in contrast to experiments, where both in-coming and out-going particles are hadrons. Connection between initial state hadrons and partons can be made by the parton distribution functions². According

¹Only when a hadron collider is considered.

²A parton distribution function, $f_{p/H}(x, Q^2)$, expresses the probability density of finding a parton-type p inside a hadron-type H , which carries x fraction of the momentum of the hadron

to the factorization theorem [4] the cross section with hadronic initial states can be obtained by a convolution of the parton distribution function(s) (PDF) with a cross section calculated on the parton level. Hence the factorization theorem enables us to construct the cross section at any given order in perturbation theory from a non-perturbative (PDF's) and a perturbative part (partonic cross section). Factorization theorem states how initial state hadrons can be incorporated, but cannot solve the problem that arises in the final state, namely, predictions are made for partons, while experiments observe hadrons. The predictive power of the partonic final state is provided by the local parton-hadron duality [5, 6]. The hypothesis of local parton-hadron duality states that the hadronic momentum flow obeys a Gaussian distribution around the initial partonic one. The hadrons, appearing in the final state, are collimated into jets. The jet momentum flow mirrors the initial partonic one.

Jets as collimated hadrons consist of $\mathcal{O}(10)$ hadrons, and showing a rich jet substructure, while in a calculation a jet is modeled by $\mathcal{O}(1)$ partons. In the lowest order of perturbation theory, one jet is approximated by exactly one parton, as going beyond the lowest order, the possible number of partons per jets increases with only one parton from order to order. Hence to reach the same level of jet substructure at the parton level several orders should be taken into account in the perturbative series, which due to the complexity of QCD calculations is unreachable. One possible and widely used solution to the problem is the use of parton shower programs [7, 8]. These take the hard scattering process with limited number of partons in the final state, and by using a probabilistic description add more partons in the final state by the so-called showering procedure. Beginning with a few highly energetic partons coming from the hard scattering process the parton shower algorithm produces further emissions from these partons using a prescription derived from the collinear factorization of QCD cross sections. The parton shower algorithm approximates the effect of higher order corrections in the collinear region. The emitted partons tend to be in the collinear region with respect to the emitter ones.

The application of parton shower to a calculation can introduce jet substructure into it, but the approach lacks one important feature. While the experiment observes hadrons, the parton shower can only increase the number of partons in the prediction. Thus hadronization should be included to bring the theoretical prediction as close as possible to the experiment from the point of view of particle content. As can be shown [9] the effect of hadronization is $\mathcal{O}(1/Q^p)$, where Q is at a scale Q .

the nominal energy scale of the hard scattering and $p \geq 1$, hence at sufficiently large energies we cannot expect too large corrections to infrared safe observables. An observable is said to be infrared safe, if it is insensitive to soft and/or collinear parton emissions. In the past several hadronization models were created [10–16] to simulate confinement, but these are only phenomenological models including parameters which are fixed by measurements.

When we make predictions we pursue high accuracy and we would like to get as close to the experimental observation as possible. The naive remedy seems to be including more and more terms in the perturbative expansion of the differential cross section and applying parton showering and one of the available hadronization models on the final state. The naive approach, although, cannot work. Beyond lowest order in perturbative QCD the hard scattering process, without the application of the parton shower, can have soft and/or collinear partons, which can also be produced during parton showering. This causes a double-counting of radiation, which should be avoided. In other words the same parton configuration can be produced both in hard scattering and in parton showering, hence resulting in a double-counting. This double-counting renders the merging of beyond leading order calculations to parton showers a non-trivial task.

In this thesis we will make NLO predictions at the hadron level for processes, which include a top quark-pair in the final state with one additional particle, which can be a vector boson, a (pseudo)scalar or a jet.

1.1 Importance of being Top

The mass range of the known quarks spans more than four orders of magnitude, but this hierarchy remains still unexplained. The heaviest among them is the top quark, with mass $m_t = (172.9 \pm 0.6 \pm 0.9)\text{GeV}$ and width $\Gamma_t = (2.0_{-0.6}^{+0.7})\text{GeV}$, obtained from recent PDG-live data [17]. The quark content of the Standard Model is organized into generations as $SU(2)_L$ doublets by the electroweak interaction. These generations are enlisted in Table 1.1. The top quark mass is so large, that it cannot be neglected even for LHC energies. Due to its large mass the first top quark-pair was only observed in 1995 at the TeVatron [18, 19]. The top quark, because of its large mass, serves an important role in particle physics, for instance, in measuring Standard Model parameters, providing discovery channels to the Higgs-boson, and as a possible final state it might open a door to BSM and SUSY physics. For instance, exotic mediators could create top pairs in various

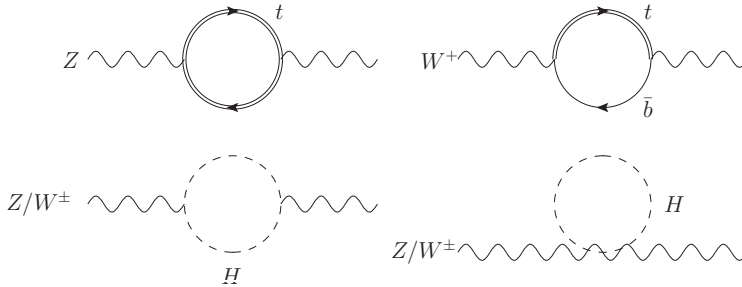


Figure 1.1: Radiative corrections coming from the top quark and the Higgs to the masses of the electroweak vector bosons.

BSM models and also the top could decay into exotic particles, such as a charged Higgs boson.

Though the top quark was only observed in 1995 its mass was already predicted from global electroweak data fits [20–23], for the reason that the electroweak vector boson masses get finite corrections coming from top quark loops as illustrated on Fig. 1.1. On this figure we also depicted the corrections coming from coupling to the Higgs. The top mass from indirect measurements was predicted [23] $m_t = (162 \pm 15_{-5}^{+25})\text{GeV}$, while from the latest TeVatron direct measurements $m_t = (173.2 \pm 0.9)\text{GeV}$ [24]. The same indirect analysis predicts the SM Higgs mass to be $m_H = (390_{-280}^{+750})\text{GeV}$. The large uncertainty band is a consequence of the logarithmic dependence of m_W on m_H .

The electroweak fits suggest an SM Higgs mass around 90GeV, hence the closest lying particle to this value is the top quark, this closeness suggests, that the top quark has the most natural mass among the observed particles. We would like to note, that during writing this thesis both the ATLAS and CMS collaborations found a new boson with a mass of 125GeV [25, 26].

$$\begin{pmatrix} u \\ d' \end{pmatrix} \begin{pmatrix} c \\ s' \end{pmatrix} \begin{pmatrix} t \\ b' \end{pmatrix}$$

Table 1.1: Three generations of quarks arranged into doublet. The lower quarks are primed, since the electroweak eigenstates do not coincide with the mass eigenstates.

The coupling of fermions to the SM Higgs is proportional to their mass, thus

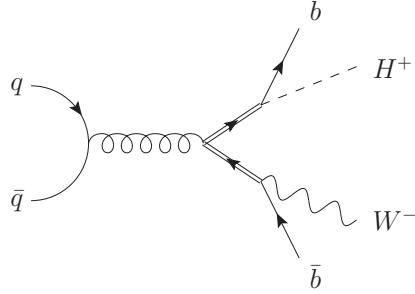


Figure 1.2: This figure shows a top quark-pair decaying into a charged Higgs and a W^- .

the top quark has the highest one. Naively this feature could make the $t\bar{t} + H$ final state a possible discovery channel for the Higgs, but the cross section of this process is small, since the final state is composed of three particles with large mass (the sum of the masses is more than 400GeV). Hence the $t\bar{t} + H$ process cannot be used as a discovery channel, but it is important because it allows for measuring the coupling of the Higgs to the top. At the LHC sufficient luminosity will be collected so that the top- V (V can be W^\pm or Z) coupling will become measurable too, which could provide yet another testing ground for the Standard Model. The top quark is also interesting for beyond Standard Model physics, for example on Fig. 1.2 the creation of a top quark pair is illustrated, where the top decays into a BSM Higgs boson, while the antitop decays into a W^- . In BSM physics the top quark can have two different roles, as a signal, or as a background. On Fig. 1.2 the top quark-pair production and decay act as a signal, while the $t\bar{t} + j$ and $t\bar{t} + V$ processes are important as backgrounds in BSM searches. To take a definite example, we can consider same-signed lepton-pair production, which is quite rare in SM but highly favorable in several BSM models [27–35].

Since the weak interaction mixes the quark states, the heavy quarks can decay into several other ones by means of the weak force. The level of mixing and possible decay modes are governed by the CKM matrix, which can be written as

$$V = \begin{pmatrix} V_{ud} & V_{us} & V_{ub} \\ V_{cd} & V_{cs} & V_{cb} \\ V_{td} & V_{ts} & V_{tb} \end{pmatrix}, \quad (1.1)$$

using the CKM matrix elements the probability of the $t \rightarrow bW^+$ decay is $|V_{tb}|^2$, the conservation of probability is satisfied by

$$\sum_{q_i \in \{d, s, b\}} |V_{tq_i}|^2 = 1. \quad (1.2)$$

The experimental value for $|V_{tb}|^2$ is close to one, thus rendering the $t \rightarrow bW^+$ decay mode the dominant one. As the branching ratio ($t \rightarrow bW^+$) is close to one, measuring the probability of the other two modes is extremely difficult. These can be better measured in single top production.

The total width of the top has recently been measured by the D0 collaboration at the TeVatron in single top and top-pair production: $\Gamma_t = (1.99_{-0.55}^{+0.69})\text{GeV}$ [36]. In a theoretical calculation one can choose between several approaches to calculate the width, for instance, we can neglect the b mass and W width, or we can take into account the width of the W , or we can calculate the width with LO, NLO or even with NNLO accuracy [37–41]. In any case due to the large mass of the top quark it decays well before hadronization, so the quantum numbers of the top quark are much more accessible compared to the other quarks that form bound states due to confinement prior to decay.

It was already shown, that the top quark earned a special status among those particles, that are collectively called quarks. There is one more property making the top quark special, the charge asymmetry [42], manifesting in forward-backward asymmetry at a proton-antiproton collider such as the TeVatron, studied recently [43]. This asymmetry can be defined in the laboratory frame as [42]:

$$A_{\text{FB}} = \frac{N_t(\cos\theta \geq 0) - N_{\bar{t}}(\cos\theta \geq 0)}{N_t(\cos\theta \geq 0) + N_{\bar{t}}(\cos\theta \geq 0)}, \quad (1.3)$$

where $N_{t(\bar{t})}(\cos\theta \geq 0)$ is the number of (anti)top quarks, for which the cosine of the enclosed angle with the incoming antiproton is greater than zero. In perturbation theory A_{FB} is identically zero at LO accuracy. At the NLO accuracy the asymmetry comes from the real-emission and also from the virtual part, but with opposite signs. In the real-emission part, the effect originates in the interference between initial- and final-state gluon emission, and it is a negative contribution. This means the top quarks are most favorably emitted in the hemisphere of the incoming quark, while the contribution of the box diagrams in the virtual part is positive, meaning that the top quark is preferably emitted in the hemisphere of the antiquark in the initial state. As shown in Ref. [42] the positive contribution coming from the virtual part overcomes the negative one, thus the forward-backward

asymmetry is positive. This asymmetry can be detected at the TeVatron, since this collider is of the proton-antiproton type, the incoming direction of the proton and antiproton is fixed, and due to the parton distribution functions quarks are more likely to come from the protons, while antiquarks from the antiprotons.

In the case of the LHC the initial state is symmetric, therefore the previous reasoning cannot be used to define an asymmetry for this type of collider. One possible escape is provided by the fact, that the colliding particles are protons, hence all the valance partons are quarks, antiquarks can only come as sea-antiquarks. In QCD the top has the tendency to be emitted in the direction of the initial state quark, and because quarks can have higher momenta³, hence the top tends to acquire much larger rapidities compared to the antitop [44, 45]. Since for the LHC the $g g$ initial state is the most probable one, this asymmetry is suppressed compared to the forward-backward asymmetry at the TeVatron.

Regardless of the type of asymmetry being studied, it can serve as an important test of the SM, and it is important for new physics searches, since the asymmetries can be sensitive to new heavy vector bosons, scalars, color states or even to gravitons.

³The PDF allows much larger momenta for valance quarks as to sea-antiquarks.

Chapter 2

Methods

2.1 NLO calculations

In perturbative QCD we consider the cross section as an expansion in the strong coupling¹. Hence the cross section can be written as

$$\sigma = \sigma^{\text{LO}} + \sigma^{\text{NLO}} + \sigma^{\text{NNLO}} + \dots, \quad (2.1)$$

where LO, NLO and NNLO stand for the Leading-Order, Next-to-Leading-Order and Next-to-Next-to-Leading-Order contribution respectively. The validity of this expansion is guaranteed at sufficiently high energies by asymptotic freedom [46, 47].

The truncation of the expansion introduces a dependence upon non-physical parameters, the renormalization- and factorization-scales (μ_R , μ_F). This dependence decreases as more terms are considered in the expansion. Thus the precision of the theoretical prediction can be enhanced by introducing more terms in the expansion, but the calculational complexity increases rapidly from order to order.

In the beginning of the 21st century there were only two high-energy colliders, which could be used for studying the highest energy regime, these were the TeVatron and the LHC. These state-of-the-art machines were both hadron-hadron colliders, where the high-energy regime was investigated by proton-antiproton (TeVatron) and proton-proton (LHC) collisions at various energies. The calculation of

¹More precisely an expansion in α_s , with $\alpha_s = \frac{g_s^2}{4\pi}$, where g_s is the strong coupling constant.

the cross section at these machines are provided by the factorization theorem [4], which gives the cross section for the collision of hadrons A and B as a convolution,

$$\sigma_{AB} = \sum_{a,b} \int_0^1 dx_a f_{a/A}(x_a, \mu_F^2) \int_0^1 dx_b f_{b/B}(x_b, \mu_F^2) \sigma_{ab}(x_a p_A, x_b p_B; \mu_F^2) \quad (2.2)$$

of the parton density functions (PDF's) $f_{p/P}(x_p, \mu_F^2)$ ($p \in \{a, b\}$, $P \in \{A, B\}$), with the partonic cross section for the collision of partons a and b , $\sigma_{ab}(p_a, p_b; \mu_F^2)$. The PDF represents the probability of finding a parton type- p inside a hadron type- P with momentum fraction x_p .

The perturbative expansion of the cross section is applied to the partonic one,

$$\sigma_{ab}(p_a, p_b; \mu_F^2) = \sigma^{\text{LO}}(p_a, p_b) + \sigma^{\text{NLO}}(p_a, p_b; \mu_F^2) \equiv \sigma_{\text{NLO}}(p_a, p_b; \mu_F^2), \quad (2.3)$$

where we keep only the first two terms in the expansion. The first contribution, the LO term,

$$\sigma^{\text{LO}}(p_a, p_b) = \frac{1}{2s} \int d\Phi_B \overline{|\mathcal{M}_B|^2} \quad (2.4)$$

is the integral of the color- and spin-averaged squared Born matrix element over the Born phase space, divided by the conventional flux factor, $s = x_a x_b S$, where $S = (p_A + p_B)^2$ is the square of the hadronic center-of-mass energy. \mathcal{M}_B is the matrix element, which contains all contributing Feynman-diagrams at Born-level. For example if we consider $t\bar{t}$ production in hadron-hadron collision the diagrams are listed on Fig. 2.1, where the double line is used to illustrate a propagating massive fermion. The matrix element can be calculated from the Feynman-diagrams by means of Feynman-rules, see e.g. in Ref. [9], or in Ref. [48–50]. The partons in the final state form jets, hence not only the inclusive cross section, but one related to some jet quantity can be computed. The cross section for a jet quantity can be written for the Born contribution as

$$\sigma_J^{\text{LO}}(p_a, p_b) = \frac{1}{2s} \int d\Phi_B \overline{|\mathcal{M}_B|^2} J_n(p_a, p_b; p_1, \dots, p_n), \quad (2.5)$$

where J_n is the jet measuring function defined for n partons in the final state. In perturbation theory predictions can only be made for IR-finite quantities, hence the jet measuring function should fulfill the following properties:

$$\begin{aligned} \lim_{p_i, p_j \rightarrow 0} J_n(p_a, p_b; p_1, \dots, p_i, \dots, p_j, \dots, p_n) &= 0, \quad \forall i, j \in \{1, \dots, n\}, \\ \lim_{p_i, p_k \rightarrow 0} J_n(p_a, p_b; p_1, \dots, p_i, \dots, p_n) &= 0, \quad \forall i \in \{1, \dots, n\}, \quad k \in \{a, b\}, \end{aligned} \quad (2.6)$$

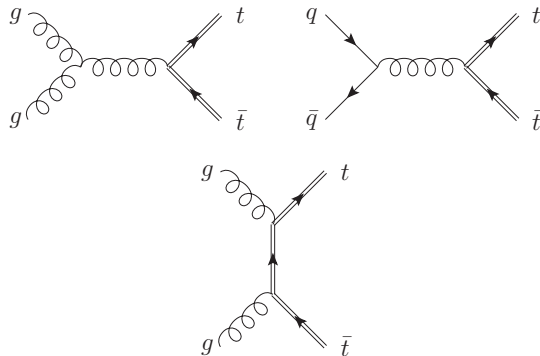


Figure 2.1: Born-level contributions to $t\bar{t}$ production in hadron-hadron collision.

these properties ensure the cross section to be finite even if one or more partons in the final state become soft and/or collinear with any other parton in the initial and final state. A parton is defined soft if its energy vanishes, while a parton is defined collinear with respect to another, if and only if the enclosed angle is zero.

For better understanding of softness and collinearity we consider the example of gluon radiation off a massless quark. If the emitted gluon and the recoiling quark are on-shell, their momenta squared are zero, the denominator of the quark propagator before emission is $E_g E_q (1 - \cos \theta_{gq})$, where E_g and E_q are the energies of the gluon and quark respectively, while θ_{gq} is the enclosed angle. As $E_g \rightarrow 0$ and/or $\cos \theta_{gq} \rightarrow 0$ the propagator factor diverges². If the process under consideration contains massless partons at the Born-level, the jet function eliminates the divergences associated with IR regions, and makes the corresponding cross section finite.

At the Born-level a one-loop running strong coupling is used, hence a dependence upon a non-physical scale is introduced³. The dependence of the cross section on these unphysical parameters turns out to be large, returning to the example of $t\bar{t}$ production, we plotted the Born-level (LO level) cross section on

²As can be shown, when $E_q \rightarrow 0$ it only produces a sub-leading, integrable divergence.

³More precisely dependence is introduced on two non-physical parameters, one is the renormalization scale (μ_R), which enters the strong coupling, while the other one is the factorization scale (μ_F), which enters the parton distribution functions, hence only present at hadron colliders. In this thesis we use $\mu_R = \mu_F = \mu$.

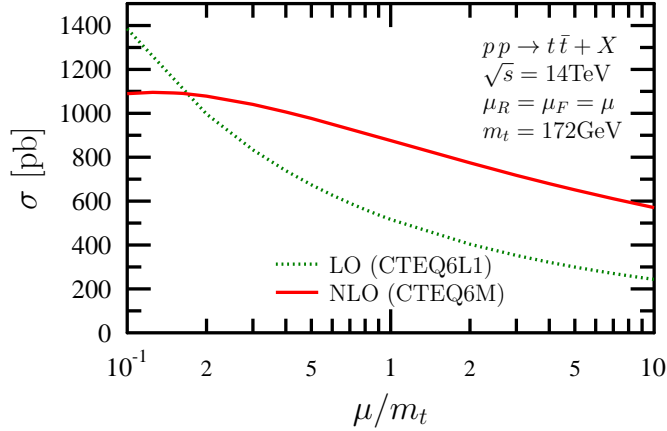


Figure 2.2: The $t\bar{t}$ production inclusive cross section as a function of the unphysical μ parameter, used for both the renormalization and factorization scales. The dotted green line shows the Born-level prediction, while the solid red one the corresponding NLO one.

Fig. 2.2 with a green dotted line. From this plot it is apparent, that the dependence on μ is large. The dependence is introduced by truncating the series expansion of the cross section as a function of the strong coupling. We expect less dependence on unphysical parameters as more and more terms are considered in this expansion.

The NLO contribution to the inclusive cross section can be written as the sum of three contributions:

$$\sigma^{\text{NLO}}(p_a, p_b) = \frac{1}{2s} \int d\Phi_B \left\{ \int d\Phi_{\text{rad}} |\overline{\mathcal{M}_R}|^2 + 2\text{Re}(\overline{\mathcal{M}_V^*} \cdot \mathcal{M}_B) \right\} + \sigma^{\text{count}}(p_a, p_b), \quad (2.7)$$

where the first term in the curly parentheses is called the real-emission part, while the second one is the virtual part. The real part contains one more parton in the final state, hence an additional integration is needed for the extra parton, denoted by $d\Phi_{\text{rad}}$, the real emission phase space is constructed from Φ_{rad} and Φ_B , $\Phi_R = \Phi_R(\Phi_B, \Phi_{\text{rad}})$. The second term is constructed as an interference of the Born matrix element with the one-loop amplitude. The third term is the collection

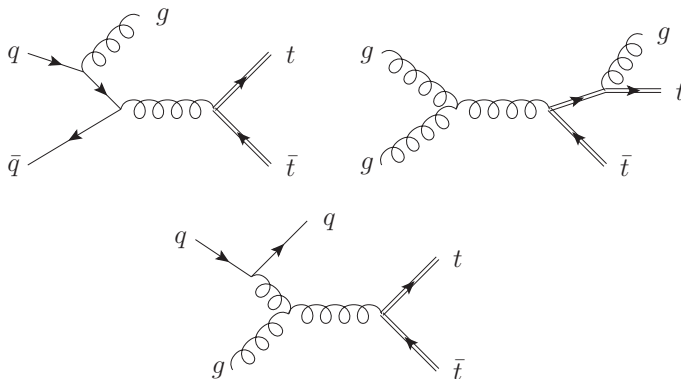


Figure 2.3: Sample Feynman-diagrams contributing to the real emission part of $t\bar{t}$ production at NLO.

of counterterms for the initial state collinear singularities [51].

In the case of $t\bar{t}$ production the real-emission part contains one additional parton in the final state along with the top quark-pair, a sample of contributing Feynman-diagrams can be found on Fig. 2.3. On these diagrams the extra parton in the final state is apparent. This extra parton can be emitted from various partons, hence introducing various IR-regions in the real-emission phase space. The presence of singular regions in the real emission phase space renders the real-emission part divergent. This divergence only rises computational problems, but not conceptual ones, since physical meaning can only be assigned to the sum of the real-emission, the virtual part and the counterterms of initial state collinear singularities. The inclusive cross section is well-defined for this process, thus singularities are expected from the virtual part, such that they cancel with those present in the real-emission part ⁴ making the sum of these two finite. It is already mentioned, that the virtual part is defined as an interference of one-loop amplitudes with the Born matrix element. Some one-loop Feynman-diagrams are depicted on Fig. 2.4 for $t\bar{t}$ production. By investigating the partons along the loop, even on the depicted diagrams, there are one or more partons, which

⁴This statement is not true in collisions with hadron(s) in the initial state. If hadronic initial states are considered, the singularities associated with final state partons collinear with initial state ones are absorbed into the redefinition of the parton distribution function.

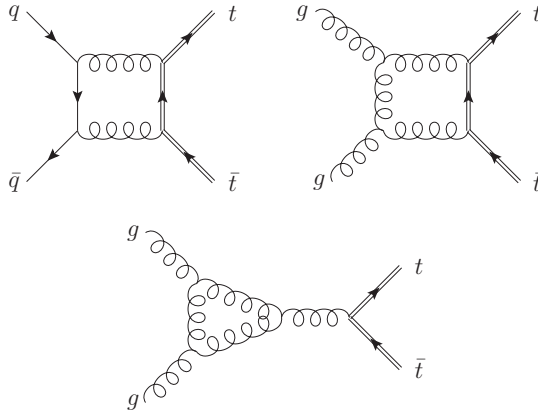


Figure 2.4: Same as the previous figure, but for the virtual part.

show IR divergence [52–54]. These divergences become manifest as $1/\epsilon$ and $1/\epsilon^2$ poles, as a consequence of performing the integration over the loop momentum in $d = 4 - 2\epsilon$ dimensions. Hence the dimensional regularization has two distinct roles in QCD: one is to regularize the UV divergences, while the other to regularize the IR divergences as well. The $1/\epsilon$ poles are partially removed by the renormalization procedure, while the remaining $1/\epsilon$ and $1/\epsilon^2$ poles are cancelled by the singularities presented in the real-emission part. The phase space integration is cumbersome computationally for complicated processes. Our aim is to make the real and virtual part separately numerically integrable in four dimensions. This can be achieved, if a subtraction method is applied to the real-emission part.

The idea of a subtraction method can be illustrated with the following example [55]. Consider the expression

$$I = \lim_{\epsilon \rightarrow 0} \left[\int_0^1 \frac{dx}{x^{1-\epsilon}} F(x) - \frac{1}{\epsilon} F(0) \right], \quad (2.8)$$

where the first term has the resemblance of the real-emission part, while the second term has an explicit ϵ pole just like the virtual part. The two terms are separately divergent, but when combined the result is finite. The problem arises in the integrand of the first term, the integrand is divergent as $x \rightarrow 0$, the integral can be made finite, if $x^{-(1-\epsilon)} F(0)$ is subtracted. We don't want to change the

result, hence the integral of this subtraction is added back, which results in

$$I = \lim_{\epsilon \rightarrow 0} \left[\int_0^1 \frac{dx}{x^{1-\epsilon}} (F(x) - F(0)) + \int_0^1 \frac{dx}{x^{1-\epsilon}} F(0) - \frac{1}{\epsilon} F(0) \right]. \quad (2.9)$$

With this subtraction the first and last two terms become separately finite, thus the $\epsilon \rightarrow 0$ operation can be carried out before the integration, and the resulting integral become finite:

$$I = \int_0^1 \frac{dx}{x} (F(x) - F(0)). \quad (2.10)$$

This example clearly illustrates the role of the subtraction schemes used in QCD to make the NLO calculation feasible numerically. In all subtraction methods we are adding zero to the NLO contribution, but in such a clever way to get rid of the singularities present in the real-emission part. Nowadays several subtraction methods exist, the interested reader can find these in Refs. [56–63].

The NLO contribution to the inclusive cross section with a suitably chosen subtraction scheme can be written as

$$\begin{aligned} \sigma^{\text{NLO}}(p_a, p_b; \mu_F^2) &= \sigma^{\text{NLO}\{R\}}(p_a, p_b) + \sigma^{\text{NLO}\{V\}}(p_a, p_b) + \\ &+ \int_0^1 dx \left[\sigma^{\text{NLO}\{C\}}(x; xp_a, p_b; \mu_F^2) + \sigma^{\text{NLO}\{C\}}(x; p_a, xp_b; \mu_F^2) \right], \end{aligned} \quad (2.11)$$

where $\sigma^{\text{NLO}\{R\}}$ is the real-emission part minus the subtraction terms, $\sigma^{\text{NLO}\{V\}}$ is the virtual part plus the integrated subtractions. The last term is the finite remainder of the integrated subtractions for the initial state collinear singularities. These terms can be expressed with the usual POWHEG terminology [64]:

$$\sigma^{\text{NLO}\{V\}}(p_a, p_b) = \int d\Phi_B V(\Phi_B), \quad \sigma^{\text{NLO}\{R\}}(p_a, p_b) = \int d\Phi_R \hat{R}(\Phi_R), \quad (2.12)$$

where Φ_R is used for the real-emission phase space, while the last term of Eq. (2.11) can be written as

$$\begin{aligned} \sigma^{\text{NLO}\{C\}}(x; xp_a, p_b; \mu_F^2) &= \int d\Phi_B \frac{1}{x} G_{\oplus}(\Phi_B), \\ \sigma^{\text{NLO}\{C\}}(x; p_a, xp_b; \mu_F^2) &= \int d\Phi_B \frac{1}{x} G_{\ominus}(\Phi_B), \end{aligned} \quad (2.13)$$

where x is the parton-in-parton momentum fraction, the reader should note that $\sigma^{\text{NLO}\{C\}}$ has an explicit dependence on x , and the integration of it is performed for $\sigma^{\text{NLO}\{C\}}$. The role of x comes from collinear parton splitting, since when the i th final state parton becomes collinear with one of the initial state partons, say with p_a , there exists a ratio x , with which we can re-express p_i , such that $p_i = (1-x)p_a$.

These formulae enable us to calculate the NLO contribution to the inclusive cross section. If this program is carried out the NLO inclusive cross section in most cases shows a decreased dependence on unphysical scales. On Fig. 2.2 we plotted also the NLO cross section as well for $t\bar{t}$ production with a solid red line. The plot shows a milder dependence on non-physical scales if the NLO contributions are added, hence enhancing the predictive power of the theoretical calculation.

It is possible to declare the NLO cross section of a jet function. The jet function has to fulfill further properties compared to Eq. (2.6). If at the Born-level the final state is composed of n partons, at the NLO level the same jet function is defined for $n+1$ partons in the final state with the following properties.

$$\begin{aligned} \lim_{p_i \cdot p_j \rightarrow 0} J_{n+1}(p_a, p_b; p_1, \dots, p_i, \dots, p_j, \dots, p_{n+1}) &= \\ &= J_n(p_a, p_b; p_1, \dots, p_i + p_j, \dots, p_{n+1}), \\ \lim_{p_i \rightarrow (1-x)p_k} J_{n+1}(p_a, p_b; p_1, \dots, p_i, \dots, p_{n+1}) &= \\ &= \begin{cases} J_n(xp_a, p_b; p_1, \dots, p_{i-1}, p_{i+1}, \dots, p_{n+1}), & k = a \\ J_n(p_a, xp_b; p_1, \dots, p_{i-1}, p_{i+1}, \dots, p_{n+1}), & k = b \end{cases} \end{aligned} \quad (2.14)$$

If the jet function is defined this way, it is called IR-safe, which is mandatory to define a finite NLO cross section for this observable. If n partons are present in the final state at the Born-level, the corresponding NLO contribution can be written as

$$\begin{aligned} \sigma_J^{\text{NLO}}(p_a, p_b, \mu_F^2) &= \\ &= \int d\Phi_B d\Phi_{\text{rad}} \left[|\overline{\mathcal{M}}_R(\Phi_R)|^2 J_{n+1}(\Phi_R) - C(\Phi_B, \Phi_{\text{rad}}) J_n(\Phi_B) \right] + \\ &+ \int d\Phi_B \left[2\text{Re}(\overline{\mathcal{M}}_V^* \cdot \mathcal{M}_B) J_n(\Phi_B) + \int d\Phi_{\text{rad}} C(\Phi_B, \Phi_{\text{rad}}) J_n(\Phi_B) \right] + \\ &+ \int_0^1 dx \left[\sigma_J^{\text{NLO}\{C\}}(x; xp_a, p_b; \mu_F^2) + \sigma_J^{\text{NLO}\{C\}}(x; p_a, xp_b; \mu_F^2) \right], \end{aligned} \quad (2.15)$$

where the real-emission phase space is given as a function of the Born and radiation phase spaces, $\Phi_R = \Phi_R(\Phi_B, \Phi_{\text{rad}})$, for brevity $J_{n+1}(\Phi_R)$ and $J_n(\Phi_B)$ mean the

$n + 1$ and n parton jet function evaluated on the real-emission and Born phase space, respectively, $C(\Phi_{\text{rad}}, \Phi_B)$ is used as a shorthand for the subtraction terms. The finite remainders of the collinear counterterms are defined accordingly

$$\begin{aligned}\sigma_J^{\text{NLO}\{C\}}(x; x\rho_a, \rho_b; \mu_F^2) &= \int d\Phi_B \frac{1}{X} G_{\oplus}(\Phi_B) J_n(\Phi_B), \\ \sigma_J^{\text{NLO}\{C\}}(x; \rho_a, x\rho_b; \mu_F^2) &= \int d\Phi_B \frac{1}{X} G_{\ominus}(\Phi_B) J_n(\Phi_B).\end{aligned}\quad (2.16)$$

2.2 Parton showers

In perturbative QCD the cross section and also all physical observables are considered as a series of the strong coupling (α_s). As already discussed the truncation introduces dependence on unphysical parameters. To reduce this dependence more and more terms ought to be calculated in this expansion, which is very tedious.

There is however, a more severe problem. Investigating the possible set of physical observables, regions can be found where a fixed order calculation will always result in a poor description because that all order terms can be enhanced.

To take an explicit example we consider the p_{\perp} -spectrum of the W -boson observed at the TeVatron. At leading order the p_{\perp} of the W is exactly zero, since the final state is only composed of the W without any recoiling particle. By adding an NLO correction, W production with non-zero p_{\perp} becomes possible because the σ^{R} part of the NLO correction contains one additional parton. By plotting $p_{\perp, W}$, we can see that in the low- p_{\perp} region the increasing tendency is changed in the first bin where it is large and negative. This is a consequence of the virtual contributions since they have only the W in the final state, thus contribute only to the $p_{\perp, W} = 0$ bin. While in the large- p_{\perp} region the NLO prediction is reliable it is not so when $p_{\perp, W} \ll m_W$. This is a corollary of terms divergent as $p_{\perp, W} \rightarrow 0$. For instance, we can find a term in the real-emission contribution which contains a factor of $\frac{\alpha_s}{p_{\perp, W}^2} \log \frac{p_{\perp, W}^2}{m_W^2}$ as compared to the LO. In the region of $p_{\perp, W} \ll m_W$ these kind of terms will enhance all order contributions. Due to this fact the predictive power of the NLO calculation is lost in this particular region.

To regain predictive power we have to take into account these contributions at all orders. There are two possible ways to do this, either by all-order *resummation* [9, 65, 66], or by a *parton shower* algorithm [8]. In this section we briefly review the main idea behind parton shower algorithms.

We consider the leading collinear emission for timelike particle splitting in a

| | |
|---------------------------------|-----------------------------------|
| $P_{q \rightarrow qg}(z)$ | $C_F \frac{1+z^2}{1-z}$ |
| $P_{g \rightarrow gg}(z)$ | $N_c \frac{(1-z(1-z))^2}{z(1-z)}$ |
| $P_{g \rightarrow q\bar{q}}(z)$ | $T_R(z^2 + (1-z)^2)$ |

Table 2.1: Angular averaged splitting kernels for QCD. N_c , C_F and T_R are related to the $SU(N_c)$ group, such as N_c is the number of color charges, while $C_F = \frac{N_c^2-1}{2N_c}$ and $T_R = 1/2$.

process containing $n + 1$ partons in the final state. In this case the differential cross section with the appropriate phase space measure can be approximated as

$$d\sigma_{n+1}(\Phi_{n+1}) \approx d\sigma_n(\Phi_n) \mathcal{P}(\Phi_{\text{rad}}), \quad (2.17)$$

where we factorized the phase space to an n -particle and a radiation one, while the probability of the splitting is expressed through \mathcal{P} . The radiation phase space can be written in the small angle approximation as:

$$d\Phi_{\text{rad}} = dt dz \frac{d\phi}{2\pi}, \quad (2.18)$$

where t is called the virtuality, $t = (p_i + p_{n+1})^2$, if the splitting occurs on the i th parton line, with $i \in \{1, \dots, n\}$ and $z = E_{n+1}/E_i$. This form for the phase space enables us to write the radiation probability in the form,

$$\mathcal{P}(\Phi_{\text{rad}}) = \frac{\alpha_s}{2\pi} P(z, \phi) \frac{dt}{t} dz \frac{d\phi}{2\pi}, \quad (2.19)$$

where $P(z, \phi)$ is the so-called splitting-kernel, its form depends on the type of splitting. The angular averaged splitting kernels can be found in Table 2.1.

Eq. (2.19) represents the probability of one splitting in the collinear region with respect to the emitter. This can be iterated ending up with the *Sudakov form-factor*

$$\Delta(t_1, t_2) = \exp \left[- \int_{t_2}^{t_1} \frac{dt}{t} \int_{z_0}^{1-z_0} dz \frac{\alpha_s(t)}{2\pi} P(z) \right], \quad (2.20)$$

which expresses the probability of no emission between t_1 and t_2 virtualities ($t_2 < t_1$). A minimal virtuality (t_0) has to be defined, below t_0 resolvable emission is not allowed. The minimal energy fraction z_0 is determined through t_0 , $z_0 = \frac{t_0}{E_i^2}$.

At this point it is worth noting, that the splitting introduced in Eq. (2.19) can be defined in other forms. When parton showering is introduced on the base of Eq. (2.19) the virtuality becomes the ordering variable of the shower. Common other ordering variables are the relative transverse momentum, k_{\perp} , and the enclosed angle, θ . These variables can be equally used in the collinear region provided by

$$\frac{dt}{t} = \frac{dk_{\perp}^2}{k_{\perp}^2} = \frac{d\theta^2}{\theta^2}, \quad (2.21)$$

these ordering variables in the collinear region are equivalent to each other, but outside it they give different finite contributions. z_0 is defined as an independent parameter when the enclosed angle is chosen as the ordering parameter.

This definition of the Sudakov form factor establishes ground for *Monte Carlo event generators*. The case of spacelike splitting can be found in Refs. [8, 9, 67].

If we would like to construct a parton shower using the model Sudakov form factor defined previously by Eq. (2.20) for a final state shower, we have to define an initial t_0 virtuality to start the parton shower. As we discuss time-like branching, the virtuality has to decrease as our event evolves in time. By running the parton shower we need virtualities where resolvable emissions take place. In order to find these we generate a random number \mathcal{R} between 0 and 1, and if the previous branching took place at virtuality t_1 , that of the second branching can be obtained by solving the following equation

$$\frac{\Delta(t_0, t_2)}{\Delta(t_0, t_1)} = \mathcal{R}. \quad (2.22)$$

The parton shower evolution stops when the resulting virtuality reaches or goes beyond the scale where *hadronization* takes place. Since the parton shower approximation sums up leading logarithms Sudakov damped regions appear in the distributions, for instance, at small p_{\perp} . But as we go away from those regions where the leading logarithmic contributions are enhanced the parton shower approximation goes wrong. Going back to our example of W production, the Sudakov-region at the very beginning of $p_{\perp, W}$ can be seen, but at scales at the order of m_W the $p_{\perp, W}$ -distribution breaks down, because when a hard, non-collinear emission takes place the parton shower approximation fails. We can improve the description if we use a *matrix element corrected shower* [8, 67].

If we consider only the first emission of a parton shower algorithm, the differ-

ential cross section can be written as

$$d\sigma = d\Phi_B B \left[\Delta(p_{\perp, \min}) + \Delta(p_{\perp}) \frac{R}{B} d\Phi_{\text{rad}} \right]. \quad (2.23)$$

In the parton shower approximation $p_{\perp} \rightarrow 0$ and

$$d\Phi_{\text{rad}} \frac{R}{B} \xrightarrow{p_{\perp} \rightarrow 0} \frac{\alpha_s}{2\pi} dz \frac{dt}{t} \frac{d\phi}{2\pi} P(z, \phi). \quad (2.24)$$

By using the $\frac{R}{B}$ factor in the first emission instead of its approximation in the $p_{\perp} \rightarrow 0$ limit, the first emission will be exact in the whole available phase space. Changing the formula for first radiation implies a change in the Sudakov factor also,

$$\Delta(p_{\perp}) = \exp \left\{ - \int d\Phi_{\text{rad}} \frac{R}{B} \Theta(p_{\perp}(\Phi_{\text{rad}}) - p_{\perp, \min}) \right\}. \quad (2.25)$$

This Sudakov-factor expresses the probability of no-emission with transverse momentum larger than p_{\perp} . The Heaviside-function in the argument restricts the phase space to that region, where the p_{\perp} is larger than a $p_{\perp, \min}$ value. Under this value only unresolved emissions take place. Hence if the first emission is wanted to be correct in the available phase space and not only in the collinear limit Eq. (2.25) should be used to generate it, while for the subsequent emissions Eq. (2.20) should be used. In the next section we will further investigate this formula, since it plays an important role in NLO matched parton showers.

2.3 NLO matched parton showers

In the following we only focus on the POWHEG [64] approach, since the POWHEG-BOX [68] uses this technique. In the previous section it was demonstrated how to extend the concept of the parton shower approximation to correctly model the first hard emission and reproduce the LO cross section. The idea behind an NLO matched parton shower is the same, for instance, generate the first emission with NLO accuracy and only after the first *hardest* emission apply parton shower approximation, but in such a way, that the observables resemble NLO accuracy. To obtain NLO accuracy at the first emission level, B should be replaced by \bar{B} in Eq. (2.23). Hence the differential cross section reads

$$d\sigma_{\text{LHE}} = d\Phi_B \bar{B} \left[\Delta(p_{\perp, \min}) + \Delta(p_{\perp}) \frac{R}{B} d\Phi_{\text{rad}} \right], \quad (2.26)$$

where Φ_B is used for the Born and Φ_{rad} for the extra radiation phase space, with $\Delta(p_\perp)$ defined by Eq. (2.25). In matching NLO calculations to SMC (Standard Monte Carlo) programs the aim is to generate events (in the standard Les Houches event format) and make these events ready for further processing by the SMC programs. In practice Eq. (2.26) is used to generate events in the Les Houches Event format, hence the LHE subscript. In the subsequent chapters for brevity we will always use LHE as a shorthand for Les Houches Event. In this NLO Sudakov form factor the Heaviside-function restricts the integration only to those configurations where the emitted parton has at least $p_{\perp, \text{min}}$ transverse momentum, while \bar{B} is given by

$$\bar{B}(\Phi_B) = B(\Phi_B) + V(\Phi_B) + \int d\Phi_{\text{rad}} \hat{R}(\Phi_R(\Phi_B, \Phi_{\text{rad}})), \quad (2.27)$$

where V is the virtual part also including the integrated subtraction terms and \hat{R} is the real-emission part minus the subtraction terms. The real-emission phase space, as we saw earlier, is constructed from the Born and a one-particle radiation phase space, hence formally $\Phi_R = \Phi_R(\Phi_B, \Phi_{\text{rad}})$. By construction

$$\sigma_{\text{NLO}} = \int d\Phi_B \bar{B}(\Phi_B). \quad (2.28)$$

Furthermore, the NLO Sudakov form factor satisfies

$$\frac{d\Delta(p_\perp)}{dp_\perp} = \Delta(p_\perp) \int d\Phi_{\text{rad}} \frac{R}{B} \delta[p_\perp(\Phi_{\text{rad}}) - p_\perp] = \frac{R}{B} \Delta(p_\perp), \quad (2.29)$$

by which one can prove the unitarity relation,

$$\begin{aligned} & \int_{p_{\perp, \text{min}}}^{\infty} dp_\perp \left[\Delta(p_{\perp, \text{min}}) \delta(p_\perp - p_{\perp, \text{min}}) + \frac{R}{B} \Delta(p_\perp) \right] = \\ & = \Delta(p_{\perp, \text{min}}) + \int_{p_{\perp, \text{min}}}^{\infty} \frac{d\Delta(p_\perp)}{dp_\perp} dp_\perp = \Delta(\infty) = 1, \end{aligned} \quad (2.30)$$

hence

$$\int d\sigma_{\text{LHE}} = \sigma_{\text{NLO}}. \quad (2.31)$$

So at the first emission level the NLO accuracy is restored. It is also informative to know the accuracy of a differential distribution of an observable O . This differential

distribution in an NLO calculation can be calculated as

$$\frac{d\sigma_{\text{NLO}}}{dO} = \int d\Phi_{\text{B}} \bar{B} \delta(O(\Phi_{\text{B}}) - O). \quad (2.32)$$

This differential distribution can be obtained from the LHE's, in such a case the achieved accuracy can be calculated as follows. By using Eq. (2.26) the differential distribution of observable O is written

$$\begin{aligned} \frac{d\sigma_{\text{LHE}}}{dO} = & \int d\Phi_{\text{B}} \bar{B}(\Phi_{\text{B}}) \left\{ \Delta(p_{\perp, \text{min}}) \delta(O(\Phi_{\text{B}}) - O) + \right. \\ & \left. + \int d\Phi_{\text{rad}} \Delta(p_{\perp}) \frac{R}{B} \Theta(p_{\perp} - p_{\perp, \text{min}}) \delta(O(\Phi_{\text{R}}) - O) \right\}, \end{aligned} \quad (2.33)$$

to exploit unitarity of the first-emission formula (Eq. (2.30)) we add and subtract the same term:

$$\begin{aligned} \frac{d\sigma_{\text{LHE}}}{dO} = & \int d\Phi_{\text{B}} \bar{B}(\Phi_{\text{B}}) \delta(O(\Phi_{\text{B}}) - O) \cdot \\ & \cdot \underbrace{\left\{ \Delta(p_{\perp, \text{min}}) + \int d\Phi_{\text{rad}} \Delta(p_{\perp}) \frac{R}{B} \Theta(p_{\perp} - p_{\perp, \text{min}}) \right\}}_1 + \\ & + \int d\Phi_{\text{R}} \Delta(p_{\perp}) R \frac{\bar{B}}{B} \Theta(p_{\perp} - p_{\perp, \text{min}}) \left(\delta(O(\Phi_{\text{R}}) - O) - \delta(O(\Phi_{\text{B}}) - O) \right), \end{aligned} \quad (2.34)$$

by using the following expansion in α_s

$$\Delta(p_{\perp}) \frac{\bar{B}}{B} = 1 + \mathcal{O}(\alpha_s), \quad (2.35)$$

the differential distribution is

$$\begin{aligned} \frac{d\sigma_{\text{LHE}}}{dO} = & \int d\Phi_{\text{B}} \bar{B}(\Phi_{\text{B}}) \delta(O(\Phi_{\text{B}}) - O) + \\ & + (1 + \mathcal{O}(\alpha_s)) \int d\Phi_{\text{R}} \Delta(p_{\perp}) R \frac{\bar{B}}{B} \left(\delta(O(\Phi_{\text{R}}) - O) - \delta(O(\Phi_{\text{B}}) - O) \right) \cdot \\ & \cdot \Theta(p_{\perp} - p_{\perp, \text{min}}). \end{aligned} \quad (2.36)$$

By dropping the $\Theta(p_{\perp} - p_{\perp, \text{min}})$ function, which effect is suppressed by $p_{\perp, \text{min}}$ [64], we can arrive at

$$\frac{d\sigma_{\text{LHE}}}{dO} = \frac{d\sigma_{\text{NLO}}}{dO} + \mathcal{O}(\alpha_s) \int d\Phi_{\text{R}} R \left(\delta(O(\Phi_{\text{R}}) - O) - \delta(O(\Phi_{\text{B}}) - O) \right). \quad (2.37)$$

Although the accuracy is formally NLO, we can expect sizeable deviations from the NLO predictions if the K-factor of the O observable is big. As a concrete example, when $t\bar{t} + W^\pm$ production is considered [69] the $p_{\perp, t\bar{t}}$ -distribution started to visibly deviate from the NLO prediction, when the differential K-factor reached the value of 2.

In the first-emission Sudakov-factor (Eq. (2.25)) the real-emission – underlying Born ratio is exponentiated. If the underlying Born vanishes in some kinematical configurations such that the real-emission part is still non-zero, the Sudakov-factor vanishes making this Born phase space point one, from where no event can be generated, since in Eq. (2.26) both terms in the parentheses vanishes. To circumvent these cases in POWHEG the concept of remnant real contributions is introduced [68, 70]. With a suitably chosen \mathcal{F} factor the real-emission part can be separated to two pieces as

$$R^s = \mathcal{F}R, \quad R^f = (1 - \mathcal{F})R, \quad (2.38)$$

and instead of $\frac{R}{B}$, only $\frac{R^s}{B}$ is exponentiated. In general \mathcal{F} is process-dependent, though chosen such a way, that as any of the singular regions is approached $\mathcal{F} \rightarrow 1$. This guarantees exponentiation in all kinematically degenerate regions of the real-emission phase space. With these modifications the Sudakov-factor, the \bar{B} function, the differential cross section for the LHE's and the differential distribution for an observable can be written in the following form:

$$\begin{aligned} \Delta(p_\perp) &= \exp \left\{ - \int d\Phi_{\text{rad}} \frac{R^s}{B} \Theta(p_\perp(\Phi_{\text{rad}}) - p_{\perp, \text{min}}) \right\}, \\ \bar{B}(\Phi_B) &= B(\Phi_B) + V(\Phi_B) + \int d\Phi_{\text{rad}} \hat{R}^s(\Phi_R(\Phi_B, \Phi_{\text{rad}})), \\ d\sigma_{\text{LHE}} &= d\Phi_B \bar{B} \left[\Delta(p_{\perp, \text{min}}) + \Delta(p_\perp) \frac{R^s}{B} d\Phi_{\text{rad}} \right] + d\Phi_{\text{rad}} R^f, \\ \frac{d\sigma_{\text{LHE}}}{dO} &= \frac{d\sigma_{\text{NLO}}}{dO} + \mathcal{O}(\alpha_s) \int d\Phi_R R^s \left(\delta(O(\Phi_R) - O) - \delta(O(\Phi_B) - O) \right), \end{aligned} \quad (2.39)$$

where \hat{R}^s is obtained from \hat{R} by replacing R with R^s .

In this subsection we only considered the POWHEG method to match NLO calculations with parton showers. There exists yet another matching technique, MC@NLO, details on this method can be found in Ref. [67].

Part II

Applications

Chapter 3

$t\bar{t} + j$ production

In this chapter we show the first application to a $2 \rightarrow 3$ process of the combination of the POWHEG-BOX and the HELAC [71] frameworks (the resulting code is called POWHE1) for producing showered events of the $t\bar{t} + j$ final state that can be used to make distributions with correct perturbative expansion up to NLO accuracy. Due to the large collision energy at the LHC, $t\bar{t}$ pairs with large transverse momentum will be copiously produced and the probability for the top quarks to radiate gluons will be sufficiently large to make the $t\bar{t} + j$ final state measurable with high statistics. Therefore, we make first predictions for such events at the TeVatron and the LHC.

This process plays an important role in the Standard model, since it has a contribution to the $t\bar{t}$ pair production inclusive cross section, and it serves as a background when the Z coupling to the top quark is considered [72]. Asymmetry studies [44, 45, 73, 74] can be used to search for beyond Standard Model physics, since these observables can be sensitive to new color states, heavy vector bosons, scalars or even gravitons.

3.1 Implementation and checks

To implement a new process within the POWHEG-BOX all subprocesses have to be provided. These subprocesses can be represented by flavor structures, which are presented in Table 3.1 and Table 3.2 for the Born- and real-emission-level, respectively. For phase space generation we generate two massive and one massless mo-

| | | | |
|----------------------------|----------------------------------|--|--|
| $qg \rightarrow t\bar{t}q$ | $gq \rightarrow t\bar{t}q$ | $\bar{q}g \rightarrow t\bar{t}\bar{q}$ | $g\bar{q} \rightarrow t\bar{t}\bar{q}$ |
| $gg \rightarrow t\bar{t}g$ | $q\bar{q} \rightarrow t\bar{t}g$ | $\bar{q}q \rightarrow t\bar{t}g$ | |

Table 3.1: Flavour structures of the Born processes, $q = u, d, c, s, b$.

| | | |
|---|---|---|
| $qg \rightarrow t\bar{t}qg$ | $qg \rightarrow t\bar{t}qg$ | $q\bar{q} \rightarrow t\bar{t}q\bar{q}$ |
| $gq \rightarrow t\bar{t}qg$ | $\bar{q}\bar{q} \rightarrow t\bar{t}\bar{q}\bar{q}$ | $\bar{q}q \rightarrow t\bar{t}q\bar{q}$ |
| $\bar{q}g \rightarrow t\bar{t}\bar{q}g$ | $q\bar{q} \rightarrow t\bar{t}gg$ | $q\bar{q} \rightarrow t\bar{t}q'\bar{q}'$ |
| $g\bar{q} \rightarrow t\bar{t}\bar{q}g$ | $\bar{q}q \rightarrow t\bar{t}gg$ | $\bar{q}q \rightarrow t\bar{t}q'\bar{q}'$ |
| $qq' \rightarrow t\bar{t}qq'$ | $q\bar{q}' \rightarrow t\bar{t}q\bar{q}'$ | $gg \rightarrow t\bar{t}gg$ |
| $\bar{q}q' \rightarrow t\bar{t}\bar{q}q'$ | $\bar{q}\bar{q}' \rightarrow t\bar{t}\bar{q}\bar{q}'$ | $gg \rightarrow t\bar{t}g\bar{q}$ |

Table 3.2: Flavour structures of the real-emission processes, $q, q' = u, d, c, s, b$.

menta using one two-particle invariant and three angles. HELAC-1LOOP was used to calculate the tree-level amplitudes corresponding to the Born-level $t\bar{t}ggg \rightarrow 0$, $t\bar{t}q\bar{q}g \rightarrow 0$ and to the real-emission-level $t\bar{t}q\bar{q}q'\bar{q}' \rightarrow 0$, $t\bar{t}gggg \rightarrow 0$ and $t\bar{t}q\bar{q}gg \rightarrow 0$. All other amplitudes are obtained from these by the method of crossing¹. The color-correlated matrix elements are generated with the help of HELAC-Dipoles [75]. To construct the spin-correlated matrix elements the polarization vectors are used to project the helicity amplitudes to the Lorentz basis. The one-loop amplitudes are obtained from HELAC-1LOOP which uses CUTTOOLS [76] to obtain the one-loop amplitudes using unitarity techniques [77–84]. It not only provides the cut-constructable part of the amplitudes but the rational terms as well [83, 84].

In order to ensure the correctness of the calculations we performed the following checks relevant to any fixed order calculation at the NLO accuracy:

- Compared the cross section at LO to the prediction of the public code MADGRAPH [85] and found complete agreement.
- Checked the virtual correction obtained from the HELAC-1LOOP program

¹Crossing means: an initial state particle can be moved to the final state by replacing the in-coming wave function by the out-going one, while a change in the particle ordering can be made by momenta reshuffling.

in several randomly chosen phase space points to that obtained from the implementation in PowHel.

- Checked in several randomly chosen phase-space regions that the ratio of the soft- and collinear limits of the real-emission matrix elements and subtractions tend to one in all possible unresolved limits.

There is an important technical issue related to the way of calculation organized in the POWHEG-BOX. The selection cuts are applied on the events obtained after hadronization. However, when computing the $t\bar{t}+j$ production cross section at fixed order, the cuts are applied at the parton level. At LO this means a cut on the transverse momentum of the only massless parton in the final state. At NLO the virtual contribution has the same event configuration as the Born one, but the real emission contribution has two massless partons in the final state, that have to be combined into a jet before the physical cut can be applied. In the POWHEG-BOX such a separation of the real and virtual contributions is not possible because the event-generation starts with an underlying Born configuration from which further parton emissions are generated. In order to make the parton-level calculation finite, we can apply a technical cut on the transverse momentum of the single massless parton in the Born configuration. With a given set of selection cuts, one has to check that the chosen technical cut is sufficiently loose such that it does not influence the physical cross section. Typically we find that for jet transverse momentum cuts of several tens of GeV, a several GeV technical cut on the transverse momentum of the massless parton at Born level is sufficiently loose. Another way of treating the same problem, also implemented in the POWHEG-BOX, is to use a suppression factor on the underlying Born configuration [86, 87].

The first calculation of the $t\bar{t}+j$ production cross section was conducted by Dittmaier, Uwer and Weinzierl [88, 89]. In order to further check our implementation, we calculated the production cross section at NLO accuracy using the same physical parameters as in Ref. [89]. Due to the technical cut, the PowHel framework is not optimal for a fixed-order computation, nevertheless our prediction, $\sigma^{\text{NLO}} = (1.78 \pm 0.01)\text{pb}$ is in agreement with the cross section quoted in Ref. [89], $\sigma^{\text{NLO}} = (1.791 \pm 0.001)\text{pb}$, within the uncertainty of our integration. Our prediction is independent of the technical cut below $p_{\perp}^{\text{t,c}} \lesssim 5\text{GeV}$ as shown in Table 3.3.

In order to check the predictions obtained with Born-suppression, we computed the distributions published in Ref. [89] at NLO accuracy and we found agreement. Examples are shown in Fig. 3.1 for the case of the transverse momentum and rapidity distributions of the jet. The lower panels show the ratio of the PowHel-

| $p_{\perp}^{\text{t.c.}}$ [GeV] | σ^{LO} [pb] | σ^{NLO} [pb] |
|---------------------------------|---------------------------|----------------------------|
| 20 | 1.583 | 1.773 ± 0.003 |
| 5 | 1.583 | 1.780 ± 0.006 |
| 1 | 1.583 | 1.780 ± 0.010 |

Table 3.3: Dependence of the NLO cross section on the technical cut $p_{\perp}^{\text{t.c.}}$.

NLO predictions to the predictions of Ref. [89]. The error bars in the lower panel represent the combined statistical uncertainty of the two computations.

We also compared distributions obtained from LHE's, including the first radiation only, to predictions at NLO. For the distributions of the transverse momenta of the jet (see also in Fig. 3.1) and the top as well as for the rapidity distribution of the top we found agreement. The rapidity distribution of the jet is slightly more central from the LHE's than from NLO.

3.2 Phenomenology

The production of $t\bar{t} + j$ final state at the NLO accuracy together with decay of the heavy quarks in the narrow-width approximation (at LO accuracy) has been published by Melnikov and Schulze in [90]. In our NLO+PS computation decays of heavy quarks are implemented in the PS, therefore, spin correlations are not included. In contrast, the narrow-width approximation allows for taking into account the spin correlations. Thus, in order to see the effect of the parton shower, we first generated distributions without the shower, but with decays (we just included on-shell decays of t -quarks, and further decays of their decay products, if unstable, turning off any shower and hadronization effect, marked as 'Decay'), then with the full shower Monte Carlo (marked with the name of the SMC). We compared the total cross section as well as several distributions to those predictions made for collisions at the TeVatron, $\sqrt{s} = 1.96\text{TeV}$, valid at the NLO accuracy. We generated two million events with PowHe1, which were showered with PYTHIA-6.4.25 [91] and HERWIG-6.5.20 [92] subsequently. For the comparison, we used the semileptonic decay channel and the following parameters and selection cuts from Ref. [90]: (i) mass of the top quark $m_t = 172\text{GeV}$; all other Standard Model

parameters as implemented in the PS programs, (ii) CTEQ6M parton distribution functions, (iii) k_{\perp} -clustering algorithm with $R = 0.5$ and four-momentum recombination scheme [93], (iv) $\mu_R = \mu_F = m_t$, (v) $p_{\perp}^{\ell^+} > 20\text{GeV}$, (vi) $\cancel{E}_{\perp} > 20\text{GeV}$, (vii) $p_{\perp}^j > 20\text{GeV}$, (viii) $|y_j| < 2$, (ix) minimum five jets, (x) $H_{\perp} > 220\text{GeV}$, where H_{\perp} is the scalar sum of transverse momenta in the event,

$$H_{\perp} = p_{\perp}^{\ell^+} + \cancel{E}_{\perp} + \sum_j p_{\perp}^j. \quad (3.1)$$

In addition, if the final state after these selection cuts contained one or more charged leptons, we rejected the event if the transverse momentum of this lepton was above 20GeV . This latter requirement is not needed in a fixed order calculation, but necessary in ours to select the semileptonic channel. The technical cut was chosen to $p_{\perp}^{\text{t.c.}} = 5\text{GeV}$.

The predicted SMC cross sections are very sensitive to the details of the analysis. We kept the leptons and neutral pions stable, while all other particles were allowed to be stable or to decay according to the default implementation in each SMC. Quark masses, as well as W , Z masses and total decay widths, were tuned to the same values in PYTHIA and HERWIG. On the other hand, each of the two codes was allowed to compute autonomously partial branching fractions in different decay channels for all unstable particles and hadrons. Multiparticle interaction effects were neglected (default in HERWIG). Additionally, the intrinsic p_{\perp} spreading of valence partons in incoming hadrons in HERWIG was assumed to be 2.5 GeV .

Considering this setup, we always found agreement between PYTHIA and HERWIG predictions within 3%, which is also the effect of including versus neglecting negative weight events in the analysis. For instance, using our selection cuts and taking into account the negative weight events, we obtained the cross sections $\sigma^{\text{PowHel+HERWIG}} = 146.9\text{fb}$ and $\sigma^{\text{PowHel+PYTHIA}} = 143.2\text{fb}$, while without the negative weight events, we obtain $\sigma^{\text{PowHel+PYTHIA}} = 147\text{fb}$. The corresponding value for the PowHel+decay case is $\sigma^{\text{PowHel+decay}} = 144.2\text{fb}$ (with negative weight events included). These numbers cannot be compared directly to the fixed-order prediction $\sigma^{\text{NLO}} = 33.6\text{fb}$ quoted in Ref. [90] for two reasons. On the one hand in Ref. [90] only one lepton family was considered in the decay of the t-quarks, while our prediction contains all three families. We checked that taking into account only one lepton family in the decay we obtain a factor of three reduction of the cross section as expected. On the other hand the authors of Ref. [90] also observed that there is a large contribution to the cross section from the emission of a hard jet from the top decay products (estimated an additional 60% at LO [94]), which is included

in our calculation, but not in their value. As this effect is not known at the NLO accuracy, in order to compare only the shapes of distributions with only decays included, we multiply the NLO predictions² with $r = \sigma^{\text{PowHel+decay}}/\sigma^{\text{NLO}} = 4.29$ (shown as ‘NLO+decay’ in Figs. 3.2 and 3.3). The lower panels show the ratio of the various predictions to the PowHel+PYTHIA one. In order to exhibit the size of the statistical uncertainty (corresponding to two million LHE’s), avoiding at the same time a very confusing plot, we show the uncertainty of only the PowHel+decay prediction with error bars.

In Fig. 3.2 we compare the transverse momentum and rapidity distributions of the antilepton at several different levels. We observe on these plots some general features: (i) the two PowHel+SMC predictions are very close except in bins with low statistics; (ii) the PowHel+decay predictions are very close to the NLO ones in the central rapidity region and for the whole p_{\perp} range. Looking more closely, we find that the spin correlations make the NLO rapidity distribution slightly wider. The addition of the parton shower makes the rapidity distribution a little even more central due to soft leptons emitted by the shower in central regions. (For jet rapidities, not shown here, the NLO and PowHel+decay predictions coincide, but the shower effect is much more pronounced.) The p_{\perp} -distributions of the leptons becomes much softer for the same reason. The same applies to the p_{\perp} spectra of the jets.

We find even larger shower effects in the comparison of the H_{\perp} -distributions in Fig. 3.3 at the decay and SMC levels. The shower makes the distribution softer, readily understood as the effect of unclustered soft hadrons in the event, that appear only in the shower.

We now turn our attention to the LHC and make some predictions for the inclusive $t\bar{t} + j$ production at the low-energy run, $\sqrt{s} = 7\text{TeV}$ in the dileptonic final state channel. We apply the following selection criteria: (i) at least three jets are reconstructed with the anti- k_{\perp} -clustering algorithm with $R = 0.5$ and four-momentum recombination scheme [95], (ii) $p_{\perp}^j > 30\text{GeV}$, (iii) $|y_j| < 2.5$, (iv) $\cancel{E}_{\perp} > 30\text{GeV}$ for e^+e^- and $\mu^+\mu^-$ pairs, while $\cancel{E}_{\perp} > 20\text{GeV}$ for $e^{\pm}\mu^{\mp}$ pairs, (v) $p_{\perp}^{\ell^-}, p_{\perp}^{\ell^+} > 20\text{GeV}$ for exactly one ℓ^+ and one ℓ^- .

For default scales we used two different choices: (i) the mass of the t-quark, m_t , and (ii) the transverse mass of the harder top, $\mu_R = \mu_F = m_{\perp}$, where $m_{\perp} = \sqrt{m_t^2 + \max\{p_{\perp,t}^2, p_{\perp,\bar{t}}^2\}}$. We expect the latter scale better interpolates between

²In the NLO predictions only one lepton family was considered, while in our calculation all three families were taken into account. We attribute the additional factor of 1.43 due to QCD radiation.

near-threshold and hard events.

In Fig. 3.4 we plot the transverse momentum distributions of the hardest, second hardest and third hardest jet. These p_{\perp} spectra are insensitive to the version of the parton shower within the statistical uncertainty of the computations, which suggests that the effect of the missing truncated shower is small. Also they are rather robust against the choice of the default scale (2–6 % variation, not shown here), suggesting small scale dependence in general. The same features are also true for the rapidity distribution of the antilepton as seen in Fig. 3.5, where we also exhibited the prediction at the decay level. The lower panel shows the ratios of the predictions to the PowHel+HERWIG case. The error bars represent the statistical uncertainty of the latter only. We find large (almost 20 %) and almost uniform effect of the shower and hadronization. In the case of the transverse momentum distribution of the antilepton the various predictions agree over the whole spectrum except that we see a large increase from the decay level to the full SMC at small p_{\perp} , see Fig. 3.6. We attribute this increase to the numerous secondary antileptons generated in the hadronization phases.

Finally, we plot the invariant mass distribution of the $\ell^+\ell^-$ pairs in Fig. 3.7. Here again the full SMC predictions are all the same. During hadronization additional (anti)leptons with $p_{\perp} > 20$ GeV may appear and such events are dropped due to our selection cut (v), resulting in a softer spectrum.

3.3 Secondary leptons in hadronic final states

At hadron colliders due to possible large QCD backgrounds experiments try to focus on analyses, where the signal contains at least one non-QCD particle, for instance, a lepton. The leptons occurring in the final state can come from the hard scattering process, or from elsewhere.

If PYTHIA is used for parton showering and hadronization, a QED shower is also present by default, which means photon emissions are also simulated from electrically charged particles. The emitted photons can turn into lepton-pairs, thus making an enriched lepton content. Although this effect is small, provided by the size of the fine-structure constant (α), and the fact that among leptons the radiation from muons and taus are highly limited, due to the associated dead-cone sizes. Thus photon radiation is mostly expected from electrons.

Extra leptons can also come from hadronization, since several low-lying neutral hadrons can be created, which can decay electromagnetically into lepton-pairs.

The first few lowest lying neutral hadrons are listed in Table 3.4. The leptonic decay of these provides low- p_{\perp} leptons and lepton-pairs with small invariant mass. Hence the rise in the first bin of p_{\perp, ℓ^+} in Fig. 3.6 can be accounted for leptons coming from low-lying meson decays.

| | Mass(MeV) | $c\tau$ | Stability |
|------------------|-----------|---------|-----------|
| π^0 | 135 | 25nm | unstable |
| K_S^0 | 498 | 2.7cm | unstable |
| K_L^0 | 498 | 15.3m | stable |
| K^0, \bar{K}^0 | 498 | NDL | unstable |
| η | 548 | 0.2nm | unstable |
| ρ | 776 | 1.4fm | unstable |
| η' | 958 | 1pm | unstable |
| ϕ | 1020 | 48fm | unstable |
| ω | 1400 | 20fm | unstable |
| D^0 | 1865 | 0.1mm | unstable |
| B^0 | 5280 | 0.5mm | unstable |

Table 3.4: This table summarizes the low-lying neutral mesons which by means of electromagnetic decay can contribute to the lepton content of the final state. All the mass and lifetimes are taken from PDG [96]. In the table NDL means No Definite Lifetime. The last column shows the default stability in PYTHIA.

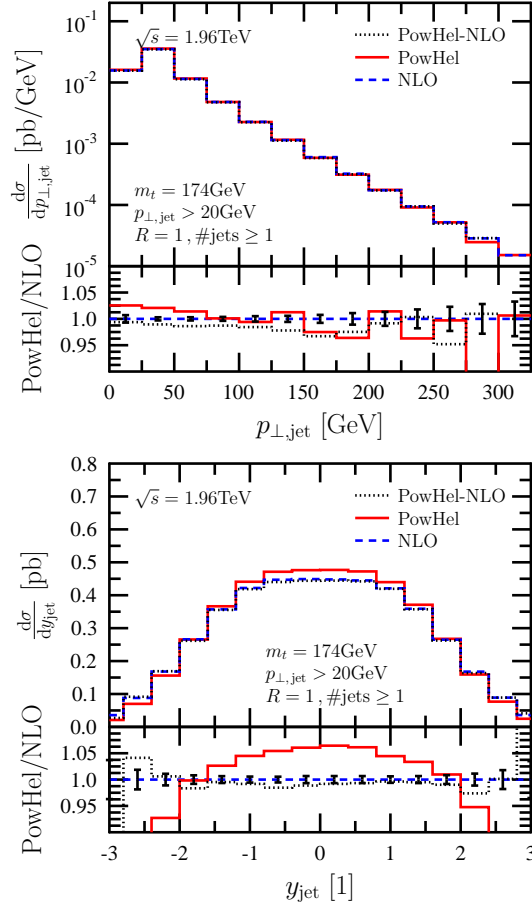


Figure 3.1: Transverse momentum and rapidity distributions of the jet.

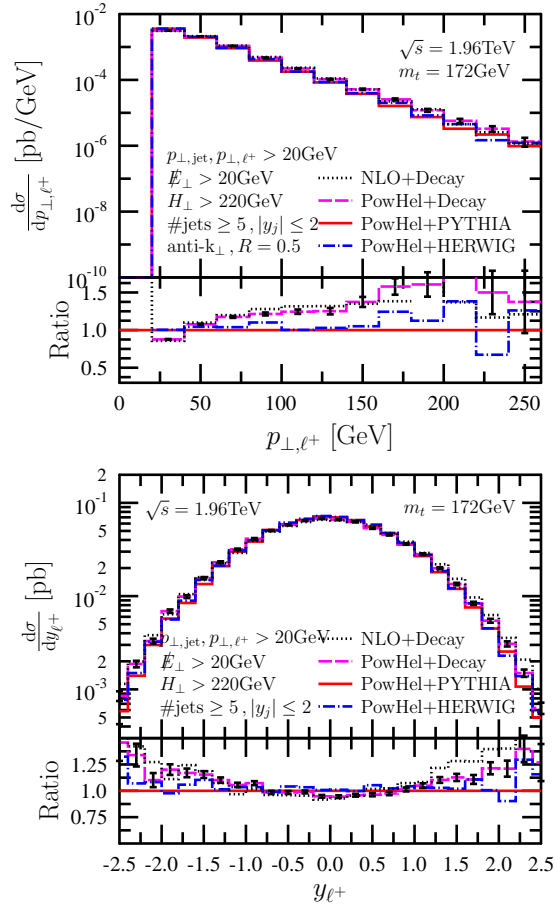


Figure 3.2: Transverse momentum and rapidity distributions of the antilepton.

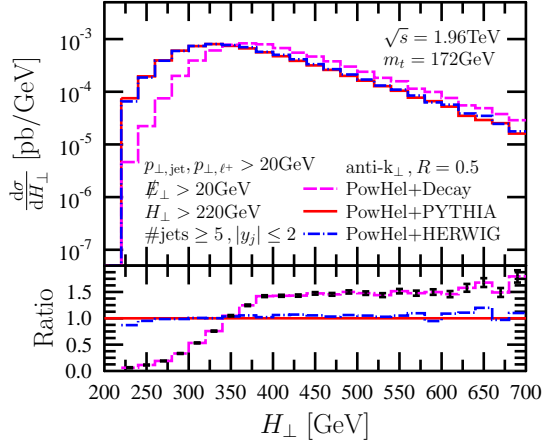


Figure 3.3: Distribution of the scalar sum of transverse momenta.

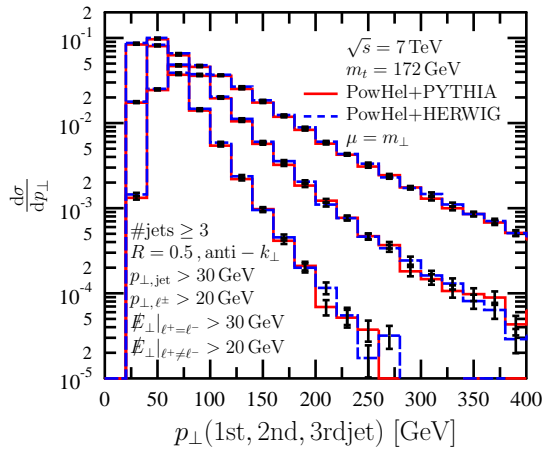


Figure 3.4: Transverse momentum distributions of the first, second and third hardest jet.

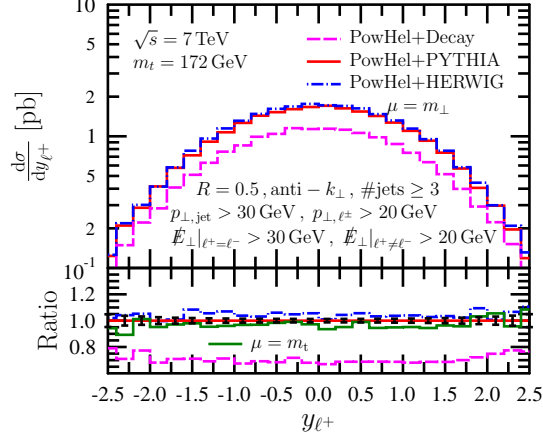


Figure 3.5: Rapidity distribution of the antilepton. The lower plot also includes the ratio of the cross section obtained with $\mu = \mu_R = \mu_F = m_t$ to that obtained with $\mu = \mu_R = \mu_F = m_\perp$ (PowHel+PYTHIA).

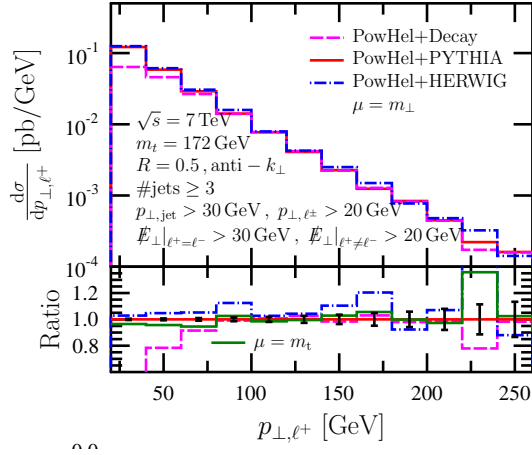


Figure 3.6: Transverse momentum distribution of the antilepton. The lower plot also includes the ratio of the cross section obtained with $\mu = \mu_R = \mu_F = m_t$ to that obtained with $\mu = \mu_R = \mu_F = m_\perp$ (PowHel+PYTHIA).

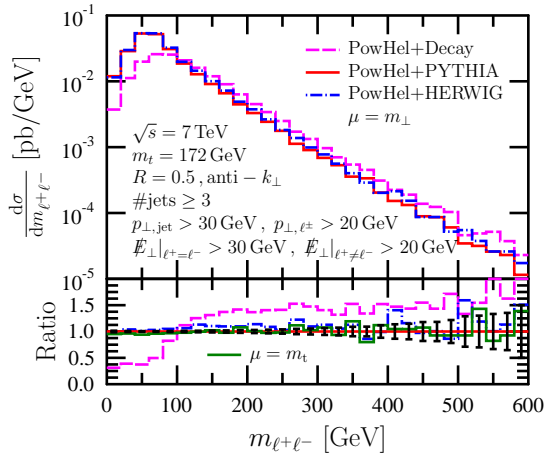


Figure 3.7: Invariant mass distribution of the lepton-antilepton pair. The lower plot also includes the ratio of the cross section obtained with $\mu = \mu_R = \mu_F m_t$ to that obtained with $\mu = \mu_R = \mu_F = m_{\perp}$ (PowHel+PYTHIA).

Chapter 4

$t\bar{t} + H$ production

The Standard Model of particle physics is a Quantum Field Theory (QFT) of fermions and gauge groups of $SU_L(2) \times U_\gamma(1) \times SU_C(3)$. Introducing masses into the $SU_L(2) \times U_\gamma(1)$ gauge-sector, the resulting mass terms will violate gauge symmetry. Hence a method is needed to *create* mass for the elementary particles. One possible way to create mass is the Higgs mechanism based upon spontaneous symmetry breaking. If this is the method used by nature to create mass for elementary particles, a spin-0 particle, the Higgs-boson, should exist. In the Standard Model of elementary particles this is the only particle, which has not been detected yet. By finding the Higgs-boson we could understand the origin of masses of elementary particles.

Recent findings at the LHC [25,26,97,98] and indirect constraints coming from electroweak fits [99] suggest a light-weighted Higgs-boson with a mass around 125GeV. For such a light-weighted Higgs-boson the possible decay channels are the $\gamma\gamma$, $\tau\tau$, $b\bar{b}$, WW and ZZ -production. The $t\bar{t} + H$ final state plays an important role in the investigation of the properties of the Higgs-boson, in particular the Higgs-boson coupling to the top quark, which serves as an important test for the Standard Model. In the recent past an enormous work was devoted to calculate the NLO QCD cross section for the $t\bar{t} + H$ process by various groups [100–104]. In this chapter we describe our matching of the NLO calculation to the parton shower [105].

4.1 Implementation and checks

Since this was the first process calculated by PowHel with a non-QCD particle in the final state, we conducted extensive checks to validate our code. We compared the Born and real-emission matrix elements in several randomly chosen phase space points with the original ones in HELAC-PHEGAS [106] to test correct parameter setup, helicity configurations and the subprocesses. The same technique was applied for the one-loop amplitude, but this time we performed the check against HELAC-1LOOP [71], and also independently check against MADLOOP using the input parameters and phase space point listed in Ref. [107], and at various renormalization scale choices [108]. When compared to MADLOOP the agreement was at least 5-6 digits. As usual the setup of the color- and spin-correlated matrix elements was tested by investigating the limiting behavior in various kinematically degenerate regions of phase space.

We also checked our predictions at the LO and NLO accuracy to independent calculations. We computed the LO cross section with different PDF sets, running strong couplings, different Higgs masses, and checked against MADEVENT [109], using the following setup: MRST2001lo PDF set, with corresponding α_s taken from LHAPDF, the other needed parameters were as listed: $m_H = 120\text{GeV}$, $m_t = 174\text{GeV}$, $m_W = 80.45\text{GeV}$, $m_Z = 91.18\text{GeV}$ and $G_F = 1.16639 \cdot 10^{-5}\text{GeV}^{-2}$. The renormalization and factorization scale were chosen to coincide with μ , where μ was varied between $2(2m_t + m_H)$ and $(2m_t + m_H)/8$. The calculations were performed at the planned LHC energy of $\sqrt{s} = 14\text{TeV}$. For later convenience we defined a scale-related parameter as $\mu_0 = 2m_t + m_H$. The results for this comparison are given in Table 4.1.

| μ | $\sigma_{\text{MAD}}^{\text{LO}}$, fb | $\sigma_{\text{PH}}^{\text{LO}}$, fb |
|-----------|--|---------------------------------------|
| $\mu_0/8$ | 1041.0 ± 1.7 | 1042.5 ± 1.5 |
| $\mu_0/4$ | 764.1 ± 2.3 | 765.6 ± 1.0 |
| $\mu_0/2$ | 576.8 ± 1.7 | 577.5 ± 0.7 |
| μ_0 | 445.3 ± 1.6 | 445.6 ± 0.5 |
| $2\mu_0$ | 349.6 ± 0.9 | 350.9 ± 0.4 |

Table 4.1: Predictions coming from MADEVENT (MAD) and our code (PH) with parameters mentioned in the text at LO.

We also made comparison to the results of [101]. For this purpose we used the same set of parameters as listed in the previous case, but this time we set $\mu_R = \mu_F = \mu_0/2$ and we varied the Higgs mass instead. The original and our results can be seen on Table 4.2.

| | m_H , GeV | $\sigma_{\text{lit}}^{\text{LO}}$, fb | $\sigma_{\text{PH}}^{\text{LO}}$, fb |
|----------|-------------|--|---------------------------------------|
| TeVatron | 120 | 5.846(2) | 5.840(4) |
| | 140 | 3.551(1) | 3.547(2) |
| | 160 | 2.205(1) | 2.203(2) |
| | 180 | 1.393(1) | 1.393(1) |
| LHC | 120 | 577.3(4) | 577.5(7) |
| | 140 | 373.4(3) | 373.5(5) |
| | 160 | 251.6(2) | 251.7(4) |
| | 180 | 176.0(1) | 176.3(3) |

Table 4.2: LO cross section checks with different Higgs masses and colliders, against [101].

As for the radiative corrections, we decided to reproduce the NLO cross sections listed in [101]. To this end we used the MRST2002n1o PDF set (taken from LHAPDF [110]), 2-loop running α_s with $\Lambda_5^{\overline{\text{MS}}} = 239\text{MeV}$, $m_t = 174\text{GeV}$, $G_F = 1.16639 \cdot 10^{-5}\text{GeV}^{-2}$, and finally the renormalization and factorization scales were set to $\mu = m_t + m_H/2$. The cross section data can be found on Table 4.3, as the reader can see we compared the cross sections for several different Higgs masses, and two different colliders (TeVatron at $\sqrt{2}\text{TeV}$, and at the planned LHC energy $\sqrt{s} = 14\text{TeV}$).

The second comparison was performed against [111]. This time we used the CTEQ5M PDF set, 2-loop running α_s with $\alpha_s(M_Z) = 0.118$, the other parameters coincide with those used above. The numerical values are listed in Table 4.4. In all these cases we found agreement with the cross section values listed in the literature.

The next step in validating our code is to compare distributions. This time we compared the predictions based on the Les Houches events to the exact NLO calculation. Although in this case we cannot expect exact agreement, as the events at the first emission level can have higher order effects as well. However,

| | m_H , GeV | $\sigma_{\text{lit.}}^{\text{NLO}}$, fb | $\sigma_{\text{PH}}^{\text{NLO}}$, fb |
|----------|-------------|--|--|
| TeVatron | 120 | 4.857(8) | 4.851(3) |
| | 140 | 2.925(4) | 2.918(2) |
| | 160 | 1.806(2) | 1.797(2) |
| | 180 | 1.132(1) | 1.128(1) |
| LHC | 120 | 701.5(18) | 701.3(8) |
| | 140 | 452.3(12) | 452.8(5) |
| | 160 | 305.6(8) | 305.0(4) |
| | 180 | 214.0(6) | 213.9(3) |

Table 4.3: NLO cross sections compared to those in [101].

| m_H , GeV | μ | $\sigma_{\text{lit.}}^{\text{NLO}}$, fb | $\sigma_{\text{PH}}^{\text{NLO}}$, fb |
|-------------|---------------|--|--|
| 120 | m_t | 718.6 ± 3.7 | 718.2 ± 0.3 |
| | $2m_t$ | 662.7 ± 3.2 | 660.8 ± 1.5 |
| | $m_t + m_H/2$ | 697.3 ± 3.2 | 695.2 ± 1.5 |
| | $2m_t + m_H$ | 634.4 ± 2.4 | 632.5 ± 1.4 |
| 150 | m_t | 381.0 ± 1.8 | 381.5 ± 0.7 |
| | $2m_t$ | 352.7 ± 1.4 | 353.3 ± 1.1 |
| | $m_t + m_H/2$ | 367.4 ± 1.5 | 368.9 ± 0.6 |
| | $2m_t + m_H$ | 334.5 ± 1.2 | 334.9 ± 0.5 |
| 180 | m_t | 221.6 ± 1.0 | 222.3 ± 0.5 |
| | $2m_t$ | 206.6 ± 0.8 | 206.7 ± 0.4 |
| | $m_t + m_H/2$ | 214.1 ± 0.9 | 214.4 ± 0.4 |
| | $2m_t + m_H$ | 194.4 ± 0.7 | 194.3 ± 0.4 |

Table 4.4: NLO cross sections of [111] compared to our predictions, The renormalization and factorization scales equal to μ at the planned LHC energy $\sqrt{s} = 14\text{TeV}$.

as suggested by the finite Born contribution and the moderate K -factor we can-

not expect large higher-order terms. The Born contribution is finite, since we only have massive particles in the final state, and the K -factor at the energy of the comparison is between 0.7 – 0.9 [103]. For the comparison we included four plots in Fig. 4.1. We chose the TeVatron setup of Ref. [101]. The first plot shows the p_{\perp} -distribution of the top quark, and as it can be seen the agreement between the calculation is better than 10%, the deviation from the original NLO calculation can be accounted for low statistics as it is suggested by the fact that ratio fluctuates around one. The distribution obtained from the Les Houches events for the rapidity of the top quark shows an almost uniform 3-5% excess compared to the NLO prediction. The p_{\perp} -distribution of the Higgs-boson shows an excess of 5%. These differences can come from different sources: the uncertainties of the NLO distributions are unknown, the weight used for the LHE's is the result of an NLO calculation, which bears the uncertainty of the MC integration, and finally higher order terms. Finally the rapidity distribution of the Higgs-boson shows exactly the same behavior as the one for the top quark. Since we were able to reproduce the cross sections for several different configurations (collider-type, Higgs mass, scale choices) we can conclude with great confidence that the excesses seen on Fig. 4.1 are effects of contributing higher-order terms. Since higher-order terms turn up at the first-emission level the question naturally raises: can the predictions be trusted? As discussed in Ref. [112] these higher-order terms are expected to make the prediction more reliable, as the prediction tends towards the NNLO one. From these various cross section and distribution comparisons we can conclude that our NLO implementation and the generation of first emission events are correct.

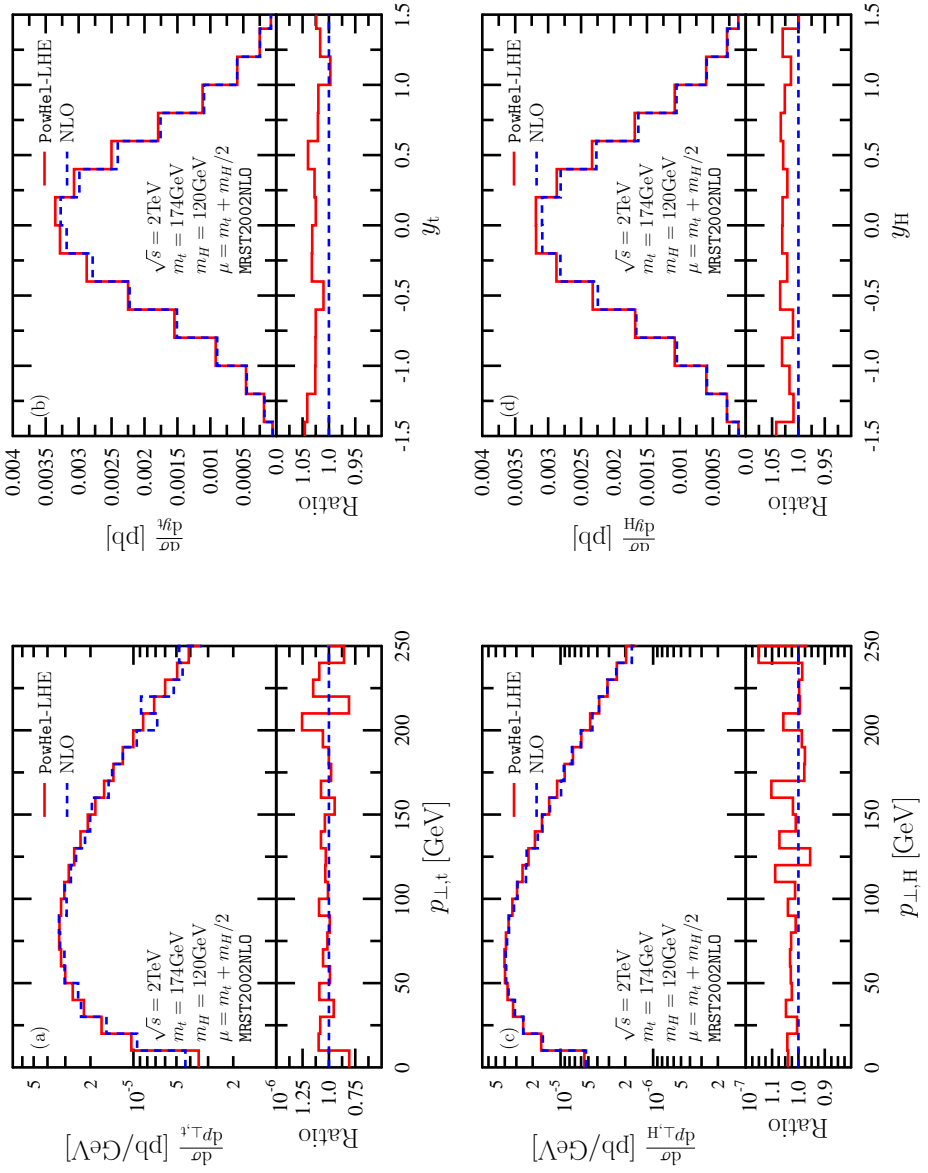


Figure 4.1: Distributions obtained from the LHE's compared to the predictions at NLO with the Tevatron setup of Ref. [101].

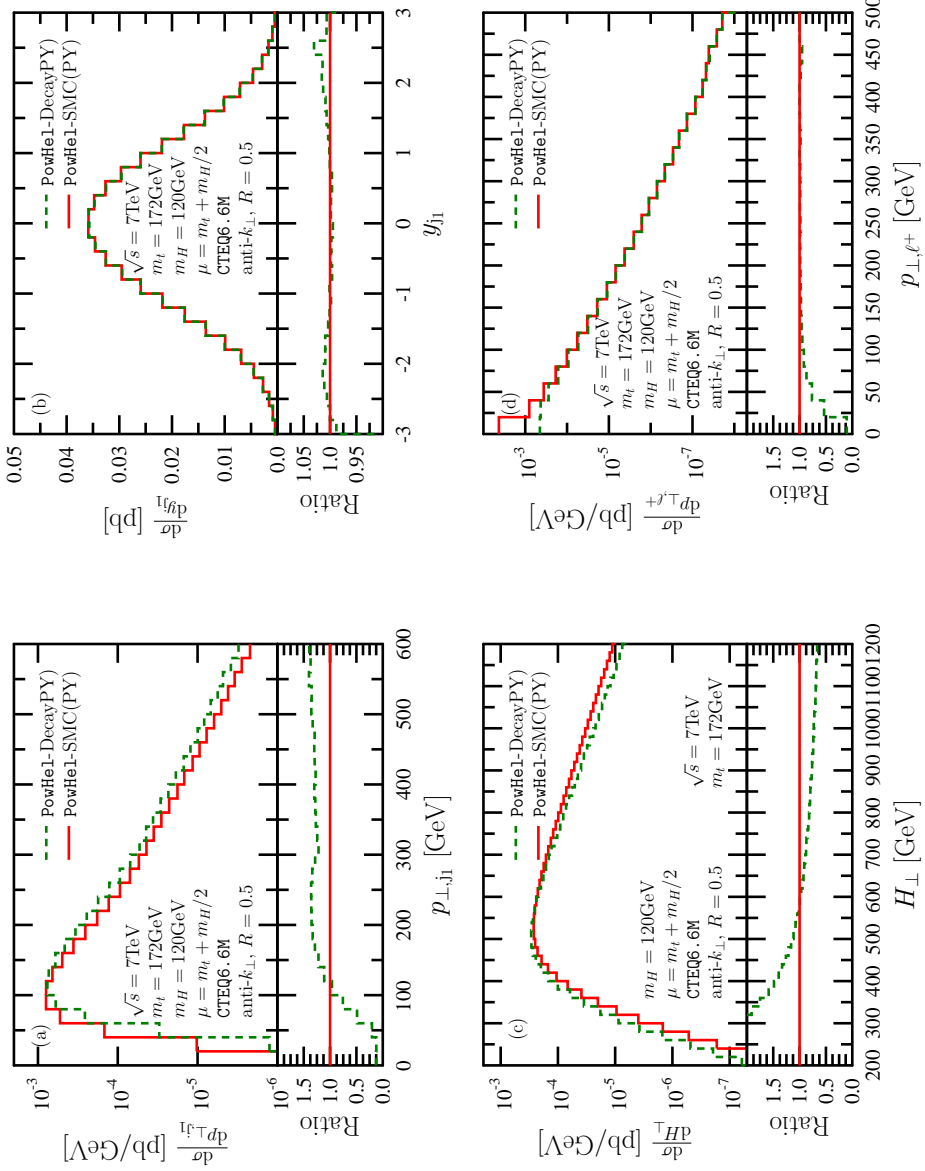


Figure 4.2: Predictions at the Decay and hadronization level at the 7TeV LHC with PYTHIA (PY).

4.2 Phenomenology

In interfacing NLO calculations to SMC programs we mainly aim at estimating the effects of showers and hadronization, therefore, we analyzed the events at two different stages of evolution:

Decay: starting from the events collected in LHEF produced by PowHe1, we just included on-shell decays of top quarks and the Higgs boson, as implemented in PYTHIA, and further decays of their decay products, like charged leptons (the τ is assumed to be unstable), W and Z , turning off any shower and hadronization effect.

Full SMC: decays, showering evolution and hadronization have been included in our simulations, using both PYTHIA and HERWIG.

In both SMC setup muons and neutral pions were assumed as stable particles. All other particles and hadrons were allowed to be stable or decay according to the default implementation of each SMC. Quark and Higgs masses, as well as W , Z masses and total decay widths, were tuned to the same values in PYTHIA and HERWIG. Each of the two codes was allowed to compute autonomously partial branching fractions in different decay channels for all unstable particles and hadrons. Multiparticle interaction effects were neglected (default in HERWIG). Additionally, the intrinsic p_{\perp} -spreading of valence partons in incoming hadrons in HERWIG was assumed to be 2.5 GeV. Considering this setup, we found agreement between PYTHIA and HERWIG predictions within 5%, except in bins where the statistics is small. Beside the conceptual differences in the parton shower and hadronization algorithms between the two SMC generators, written on the basis of different theoretical ideas (p_{\perp} vs. angular ordering, string model vs. cluster hadronization and preconfinement), a possible origin of this overall small discrepancy is the absence of the truncated shower in the HERWIG prediction. We cannot check the last point within the POWHEG-BOX framework, but the modest size of the discrepancy suggests that the effect of the truncated shower, not included in our analysis, is small.

In our computation, we adopted the following parameters: $\sqrt{s} = 7\text{TeV}$, CTEQ6.6M PDF set from LHAPDF, with a 2-loop running α_s , 5 light flavors and $\Lambda_{\overline{\text{MS}}} = 226\text{MeV}$, $m_t = 172\text{GeV}$, $m_H = 120\text{GeV}$, $G_F = 1.16639 \cdot 10^{-5}\text{GeV}^{-2}$. The renormalization and factorization scales were chosen equal to $\mu_0 = m_t + m_H/2$. We decided to switch on all possible decay channels of the Higgs boson, imple-

mented in the SMC programs.¹ We used the last version of the SMC codes: PYTHIA 6.425 and HERWIG 6.520.

We studied the effect of the full SMC by comparing distributions at the decay and SMC level. As the number of particles is very different at the end of the two stages, we first made such a comparison without any selection cut, in order to avoid the introduction of any bias. This way the cross-section at all levels is indeed exactly the same. We found $\sigma_{\text{PowHel}} = \sigma_{\text{PowHel+DECAY}} = \sigma_{\text{PowHel+SMC}} = 95.872 \pm 0.007$ fb (here and in all following σ predictions the quoted uncertainties are the statistical ones only). As an illustrative example, we present the distributions of the transverse momentum and rapidity of the hardest jet, p_{\perp,j_1} , y_{j_1} , the H_{\perp} and the antilepton p_{\perp} -distribution on Fig. 4.2. For the H_{\perp} -distribution, the definition of Eq. (5.2) was adopted. The jets are reconstructed through the anti- k_{\perp} algorithm with $R = 0.5$, by using FASTJET 2.4.3 [113]. One can observe a rather significant softening in the transverse momentum spectrum as going from results at the decay level to full SMC ones. On the other hand, the effect of the shower on the rapidity of the hardest jet is almost negligible and rather homogeneous. We distinguished several classes of jets including final state emissions, according to their origin: jets that can be traced back to (i) first radiation emissions, (ii) the decay products of the Higgs boson, (iii) the decay products of the top and antitop quarks, (iv) a mixing of the previous ones. In particular, main contributions to the p_{\perp,j_1} spectrum shown in Fig. 4.2 are due to jets of the (iv) and (iii) class. Also on the H_{\perp} -distribution the effect of softening is visible, which is accompanied by the distortion of the distribution. The antilepton p_{\perp} -distribution remains the same as before parton showering since only photon showering can change its transverse momentum, but the small value of the fine structure only allows for a reduced amount of photon radiation. Hence the p_{\perp} -distribution can hardly be affected by the showering. As for the y_{j_1} -distribution, the tails are dominated by jets of the (iv), (i) and (iii) classes.

In Ref. [107] the invariant mass, m_{BB} , and the separation in the rapidity–azimuthal-angle plane of the two hardest lowest-lying B-hadrons, ΔR_{BB} , were studied, by choosing a dynamical scale for the generation of the hard-scattering events and by taking into account only the $H \rightarrow b\bar{b}$ decay channel. In that calculation the renormalization and factorization scales were chosen equal to

$$\mu = (m_{\perp,t} \cdot m_{\perp,\bar{t}} \cdot m_{\perp,H})^{\frac{1}{3}}, \quad (4.1)$$

¹In PYTHIA there are two more decay channels than in HERWIG, and partial decay fractions in each leptonic, bosonic and partonic channel differ in the two codes.

where m_{\perp} is the transverse momentum defined through the mass (m) and transverse momentum (p_{\perp}) of the particle as $m_{\perp} = \sqrt{m^2 + p_{\perp}^2}$. To make the comparison we considered the lowest lying B hadrons just before they decay. Besides computing all p_{\perp} -distributions already presented in that paper, always finding agreement, we also computed the aforementioned B -hadron distributions reproducing the same simulation setup and without applying any cut. We considered only the $H \rightarrow b\bar{b}$ decay channel, as well as all channels. In the former, we found agreement with the predictions of Ref. [107]. The effect of the remaining channels, not studied in that work, produces an increase in the region below 80 GeV in the m_{BB} spectrum and only for large ΔR_{BB} , as shown in Figs. 4.3 and 4.4. Pairs of B -hadrons both including quarks that can be traced back to Higgs decays only populate the region of the m_{BB} spectrum below m_H . The region above m_H is instead dominated by pairs with at least one B -hadron that can be traced back to a (anti)top decay.

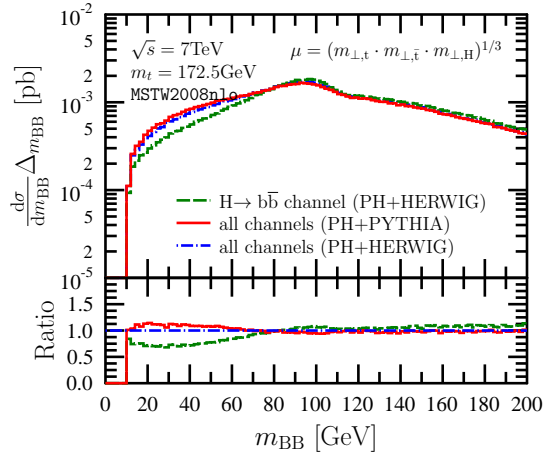


Figure 4.3: Invariant mass distribution of the two hardest lowest-lying B hadrons at the SMC level. These results are presented in sigma per bin, just to allow an easier comparison with the results of Ref. [107], having been obtained in the same setup, without applying any cut. The effects of including all H decay channels, with respect to the case of a single $H \rightarrow b\bar{b}$ channel (dashed line), were computed by interfacing PowHel to both PYTHIA (solid line) and HERWIG (dash-dotted line).

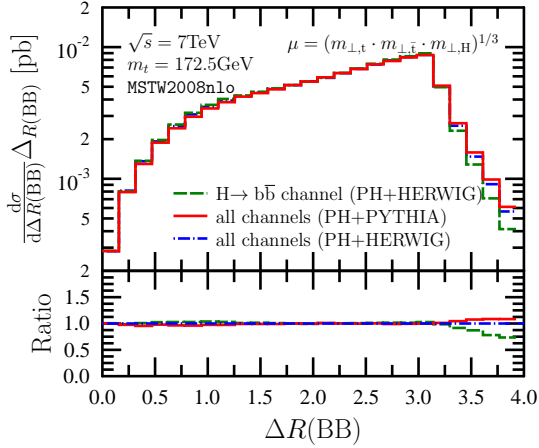


Figure 4.4: The same as Fig. 4.3, for the azimuth-rapidity distance correlations of the two hardest lowest-lying B hadrons.

The effects of the decay and shower also depend on the selection cuts. While the typical selection cuts include both leptons and hadrons, we started with a restricted set, not involving any leptonic cut, in particular as for the number of leptons. This is motivated by the fact that this number can be quite different at the decay and shower level, as the shower (including hadronization) produces many secondary leptons, for possible sources see Sect. 3.3. Thus, coming back to our setup, we considered and implemented cuts only on jet variables:

- (i) For each jet $p_{\perp}^j > 20\text{GeV}$.
- (ii) We demand on our jets to situate in the central region: $|y^j| \leq 2.5$.
- (iii) The minimal number of jets presented in the event should be 4, otherwise the event is discarded.

We show the distribution of the scalar sum of all transverse momenta in the event, H_{\perp} in Fig. 4.5. We can see that the spectrum becomes softer due to showering effects, with respect to that computed at the decay level, as expected. The same is true and even more evident if one singles out the hadronic component

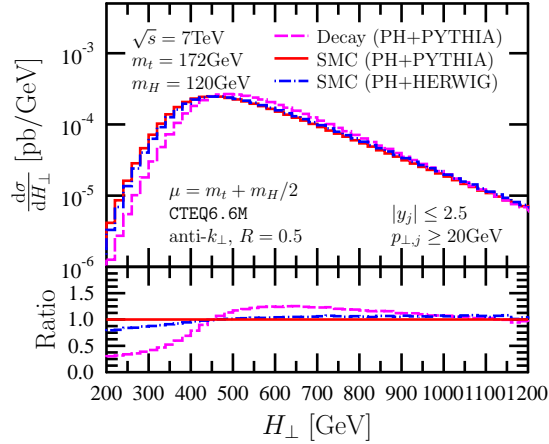


Figure 4.5: Distribution of the sum of the transverse momenta of all particles, at the decay level (dashed line) and at the SMC level, as obtained by interfacing PowHel to PYTHIA (solid line) and HERWIG (dash-dotted line). Only hadronic cuts were applied.

of H_{\perp} (not shown). On the other hand, the effects of the shower on the (anti-)lepton transverse momentum, p_{\perp, ℓ^-} , and the missing transverse momentum, \cancel{p}_{\perp} , as shown in Figs. 4.6 and 4.7, are small and rather uniform, except for a significant increase for small values, which is due to secondary leptons produced in the shower and during hadronization. The cross-sections at the decay and at the SMC level, after the hadronic cuts listed above, amount to $\sigma_{\text{PowHel}+\text{DECAY}} = 92.29 \pm 0.01$ fb, $\sigma_{\text{PowHel}+\text{PYTHIA}} = 90.46 \pm 0.01$ fb and $\sigma_{\text{PowHel}+\text{HERWIG}} = 90.99 \pm 0.01$ fb.

In the following we present further predictions for $t\bar{t} + H$ production with parton shower and hadronization effects at LHC. In addition to the jet cuts (i–iii) mentioned above, we also applied selection cuts on the leptonic variables²: (iv) we focused on the dileptonic channel, with exactly one ℓ^+ and one ℓ^- in the final state with p_{\perp} greater than (v) $p_{\perp, \min}^{\ell^{\pm}} = 20\text{GeV}$ and (vi) $|y_{\ell^{\pm}}| \leq 2.5$, whereas the transverse missing energy of the event was constrained to (vii) $\cancel{E}_{\perp, \min} \geq 30\text{GeV}$.

In Fig. 4.8 we present the distribution of the invariant mass of all jet pairs. Here the effect of the shower is again quite significant. In particular, there is a

²Similar cuts are applied by the LHC experiments.

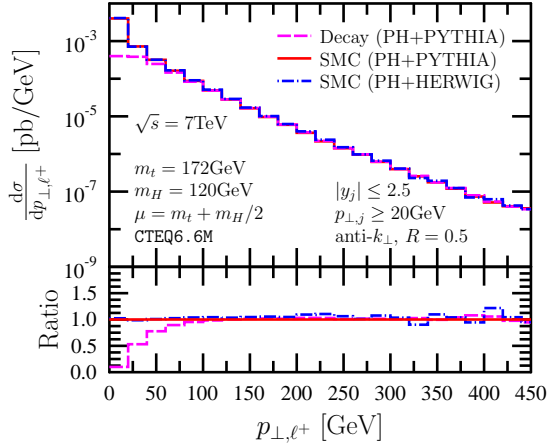


Figure 4.6: The same as Fig. 4.5, for the transverse momentum of all antileptons.

small bump around the Higgs mass, as already noticed in [114], visible in the data at the decay level, which is completely washed out when PS is included. The same is true for the invariant mass distribution of the two hardest jets (not shown). The cross-section after cuts, at the SMC level, are $\sigma_{\text{PowHel+PYTHIA}} = 5.376 \pm 0.010$ fb and $\sigma_{\text{PowHel+HERWIG}} = 5.521 \pm 0.011$ fb.

One of the biggest differences in the results produced by PYTHIA and HERWIG interfaced to the POWHEG-BOX noticed in Ref. [115] in the study of a different process was the observation that HERWIG gives rise to hard jets more central than PYTHIA. We observe the same trend in our results, but by far to a lesser extent. In particular, in the bins around zero rapidity the ratio between the rapidity distributions of PowHel + HERWIG and PowHel + PYTHIA found in our study amounts to maximum 1.05, both in case of the hardest and the second hardest jet. On the other hand, the agreement between the two SMC, as for the rapidity distributions of leptons and antileptons, was found to be even closer.

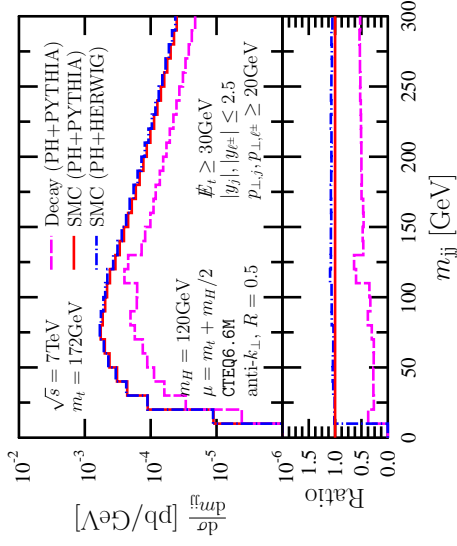


Figure 4.8: Invariant mass distribution of all jet pairs. Results at the decay level (dashed line) are shown together with results after showering and hadronization, obtained by interfacing PowHel1 predictions to both the PYTHIA (solid line) and HERWIG (dash-dotted line) SMC. The full set of hadronic and leptonic cuts was applied.

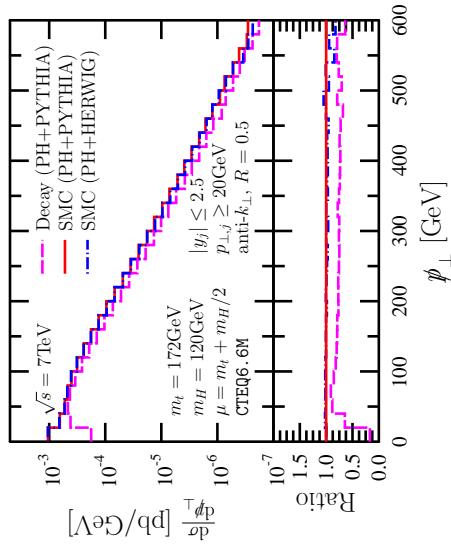


Figure 4.7: The same as Fig. 4.5, as for the total missing transverse momentum.

Chapter 5

$t\bar{t} + Z$ production

In this chapter we discuss $t\bar{t} + Z$ production. We will not only focus upon the NLO+PS predictions, but we would like to analyze the scale dependence at the NLO level as well for various observables, since in the literature no publication considered the scale variations on observables other than the cross section and the p_{\perp} -distribution for the Z [116,117]. The Z , as an uncharged, heavier brother of the γ mediates the electroweak interactions (along with W^{\pm}), but along with the γ , its coupling to the top quark never been measured experimentally [72]. This could be a possible additional verification of the Standard-Model and it serves as a possible indicator for BSM physics, since if a large deviation is found it could be accounted for beyond Standard Model physics. Although the final state is quite massive, by increasing luminosity this process will be available even for precision studies in the near-future at the LHC. This process also serves an important role as a possible background for various BSM and SUSY searches. In the SM those events, where like-sign¹ leptons, missing energy and jets come from decaying b-quarks are seldom observed, while in various BSM models [27–35] the number of these events can be enhanced, thus serving as a possible way to investigate the boundaries of the SM. Although in the case of $t\bar{t} + Z$ in the dileptonic top decay-channel two opposite signed leptons are produced, the charge of one of the leptons can be misreconstructed² resulting in like-sign leptons in the final state.

The authors of [117] presented prediction for the $p_{\perp,Z}$ -distribution only. In this chapter we repeated the NLO calculation in [117] and investigated the scale de-

¹Same-sign.

²In the literature this case are also called *q-flips* [118].

pendence for various observables. Furthermore we used our PowHel framework not only to repeat the NLO calculation, but to perform the first NLO+PS matching for this process.

5.1 Implementation and checks

For this process we have to follow a different path for validating our calculation, since we were unable to reproduce the cross sections of the original publication [117], nor the published distributions. Although two calculations were carried out in the past, we can only report on the full one, where we consider all possible initial states. We cannot limit our calculation to only gluon-gluon initial state, as the organization of POWHEG-BOX does not allow such a computation.

We compared the Born and real-emission squared matrix elements against MADEVENT [109] in several randomly chosen phase space points. We also made a check upon the color- and spin-correlated matrix elements by carefully investigating the various soft- and collinear limits of all contributing subprocesses. For the virtual part we made a comparison with GoSam [119,120] in several randomly chosen phase space points also, and we found agreement in all terms of the Laurent-series of ϵ . For the $\mathcal{O}(\epsilon^0)$ term the agreement was at least 6 digits for each phase space point. We made an additional check by implementing the $t\bar{t} + \gamma$ process, which has the same subtraction terms as this one.

Before we go on with our predictions we show on Fig. 5.1, that the $p_{\perp,Z}$ -distributions obtained by [117] even at the tree-level differs from the one calculated by MADEVENT and also from our one. We report a difference between our NLO calculation respect to [117], since our NLO cross section was $\sigma_{\text{NLO}} = (1.121 \pm 0.002)\text{pb}$, while in their calculation they found $\sigma_{\text{NLO}} = 1.09\text{pb}$ [121]. We carefully chose the related parameters to coincide the ones used within [117], supported by the same prediction for the leading order cross section 0.808pb . For this configuration we report of $K_{\text{inc}} = 1.39$, instead of $K_{\text{inc}} = 1.35$ calculated by [117].

5.2 NLO predictions for the LHC

From the almost constant value of the K-factor for the p_{\perp} -distribution of the Z-boson the authors of Ref. [117] speculated that other distributions behave similarly at NLO accuracy. In our calculation we found a different behaviour, that is, important distributions changes if NLO corrections are included. For a definite

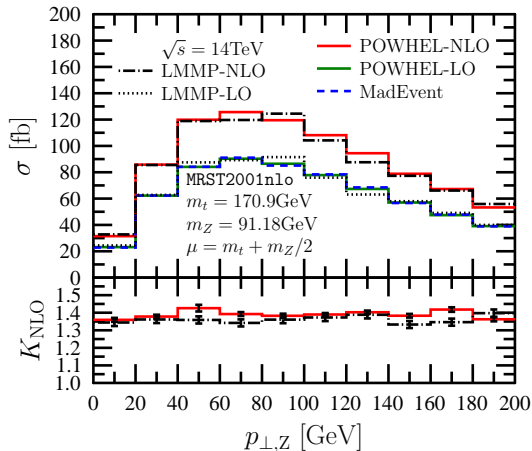


Figure 5.1: This figure shows the p_{\perp} -distribution for the Z, LMMP stands for the result of [117], POWHEL stands for ours, finally we added the tree-level calculation performed by MADEVENT. The lower panel shows the K -factors for the LMMP and PowHel calculations with black and red lines respectively.

example on Fig. 5.2 we plotted the p_{\perp} -distribution for the top-quark using the same setup as Ref. [117], where we see that for this distribution the K -factor is not constant.

We turn to making predictions for the LHC, for which we chose the CTEQ6.6M PDF set from LHAPDF, two-loop running α_s , with $\Lambda_5^{\overline{MS}} = 226\text{MeV}$, $m_t = 172.9\text{GeV}$, $m_Z = 91.1876\text{GeV}$, $m_W = 80.399\text{GeV}$, $G_F = 1.16639 \cdot 10^{-5}\text{GeV}^{-2}$, the renormalization and factorization scales were chosen equal to $\mu_0 = m_t + m_Z/2$. For three different LHC energies (7, 8 and 14TeV) the total LO and NLO cross sections are listed on Table 5.1. To obtain the cross sections no cut was needed Because at the Born-level the contributing matrix elements are finite.

For the 14TeV LHC our predictions can be found on Fig. 5.3 and on Fig. 5.4. On Fig. 5.3 the p_{\perp} and rapidity distributions are depicted for the Z-boson and the top. The blue and red bands illustrate the scale dependence at LO and NLO. To analyze the scale dependence we varied the renormalization (μ_R) and factorization scale (μ_F) between $\mu_0/2$ and $2\mu_0$ with $\mu_F = \mu_R$ throughout. At the NLO level the scale dependence, as it can be readily seen from the size of the band, is

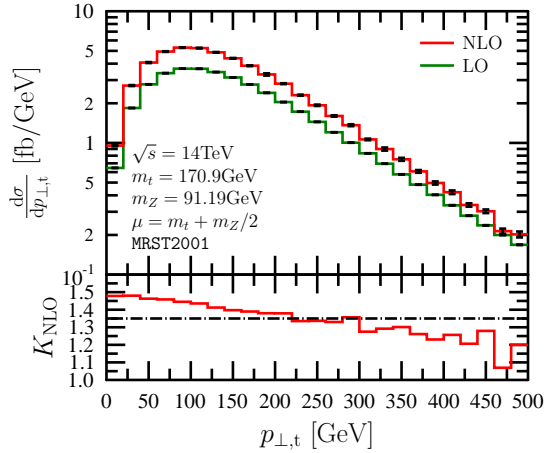


Figure 5.2: On this plot we illustrate the p_{\perp} -distribution for top quark in exactly the same setup used by [117]. On the lower panel we plotted the NLO K -factor calculated by ourselves, and the inclusive one obtained from [117].

greatly decreased. The K -factor changes in each case, the change is the slightest for the Z -boson p_{\perp} and increased for the top p_{\perp} . For both particles further away from the central region the K -factor dramatically increases, hence the NLO predictions become unreliable. If an observable in a perturbative expansion gets a large contribution from the NLO correction it can be expected that the NNLO corrections are large (though smaller than the NLO). Hence to gain predictive power higher order terms should be included as well.

On Fig. 5.4 ΔR and the rapidity separations are depicted. For the ΔR separation the following definition was used

$$\Delta R_{ij} = \sqrt{\Delta\phi_{ij}^2 + \Delta y_{ij}^2}, \quad (5.1)$$

where ΔR_{ij} is the ΔR separation between particle i and j , $\Delta\phi_{ij}$ is the azimuthal angle difference, and Δy_{ij} is the difference in the two rapidities. As in the previous set of plots the scale dependence is reduced if NLO corrections are added. The K -factor changes rapidly even in the central region.

On Fig. 5.5 and on Fig. 5.6 plots are shown for the 7TeV LHC. From the lower panels it is apparent, that the inclusive K -factor is decreased compared to the

| \sqrt{s} | $\sigma^{\text{LO}}(\text{fb})$ | $\sigma^{\text{NLO}}(\text{fb})$ | $K\text{-fact}$ |
|------------|---------------------------------|----------------------------------|-----------------|
| 7TeV | 104.76 ± 0.02 | 138.73 ± 0.02 | 1.32 |
| 8TeV | 155.74 ± 0.02 | 208.4 ± 0.1 | 1.33 |
| 14TeV | 747.5 ± 0.2 | 1018.3 ± 0.5 | 1.36 |

Table 5.1: Various cross sections obtained for different energies at the LHC.

14TeV LHC case. At 7TeV the K -factor shows larger dependence on the p_{\perp} of Z compared to the 14TeV case. It seems that in the high rapidity region of the top-quark the K -factor is increased and at $|y_t| = 2.5$ it reaches the value of 2. On the other hand the dependence of the K -factor on the p_{\perp} of the Z is more flat as compared to the previous setup. In the NLO corrections one more parton can be present in the real radiation part, hence the emission of a sufficiently hard extra parton can soften the p_{\perp} spectra of the top quark and even the Z -boson. This softening at 7TeV makes the p_{\perp} spectra of the top go beyond the LO prediction resulting in a K -factor less than one in the high p_{\perp} region. Since this extra radiation cannot come from the produced Z -boson, its p_{\perp} spectra is less affected. On Fig. 5.6 the same tendency can be seen as in the case of the 14TeV LHC with one exception, in the case of ΔR_{tZ} the NLO correction seems flatter, resulting in a more constant K -factor.

Considering both the 14TeV and 7TeV predictions in general it can be said, that the NLO corrections tend to be in the range of 30 – 40% making the NLO predictions widely reliable, the K -factor only tends to be larger than 1.5 in the edges of the kinematically available regions. The dependence upon unphysical scale choices is decreased in each case making the theoretical predictions reliable.

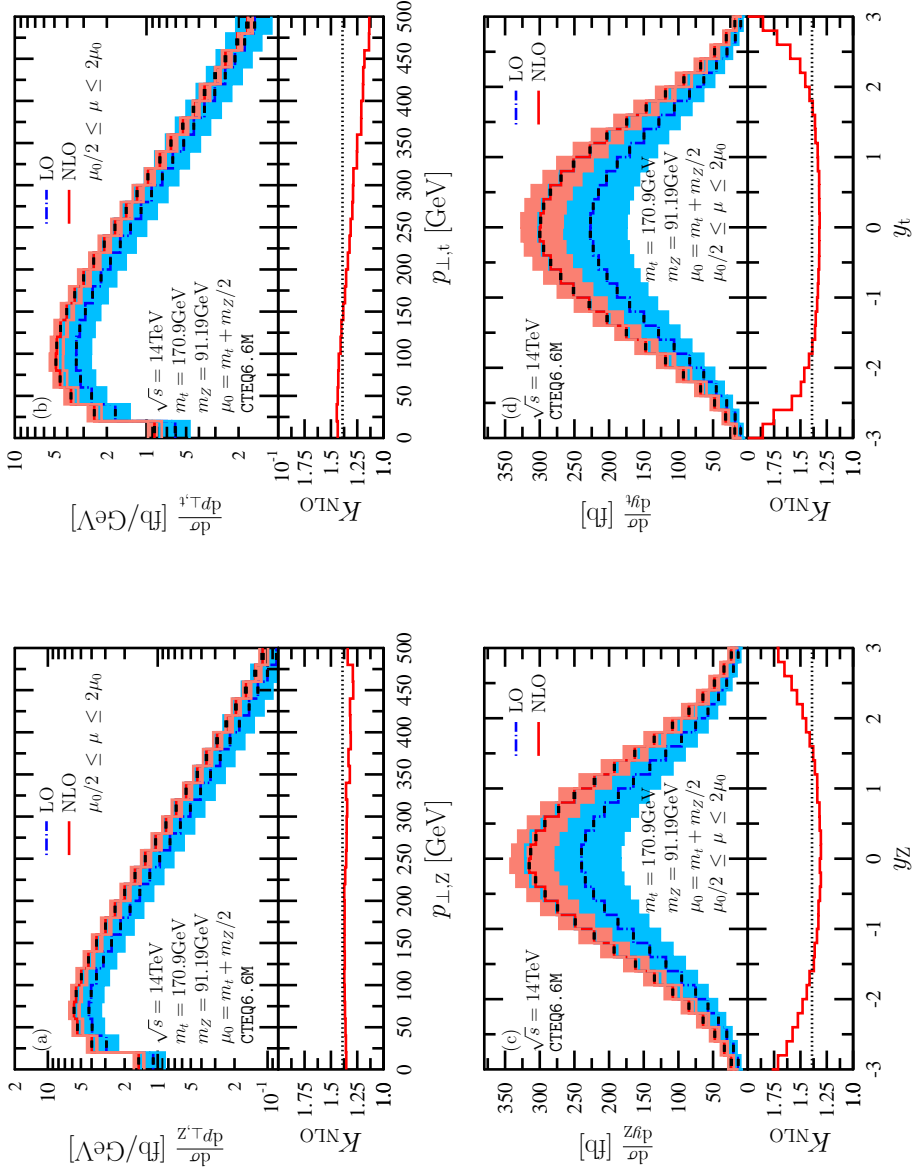


Figure 5.3: This figure shows p_{\perp} and rapidity distributions for the Z and top at 14TeV LHC. The lower panel shows the NLO K -factor compared to the inclusive one $K_{\text{inc}} = 1.39$.

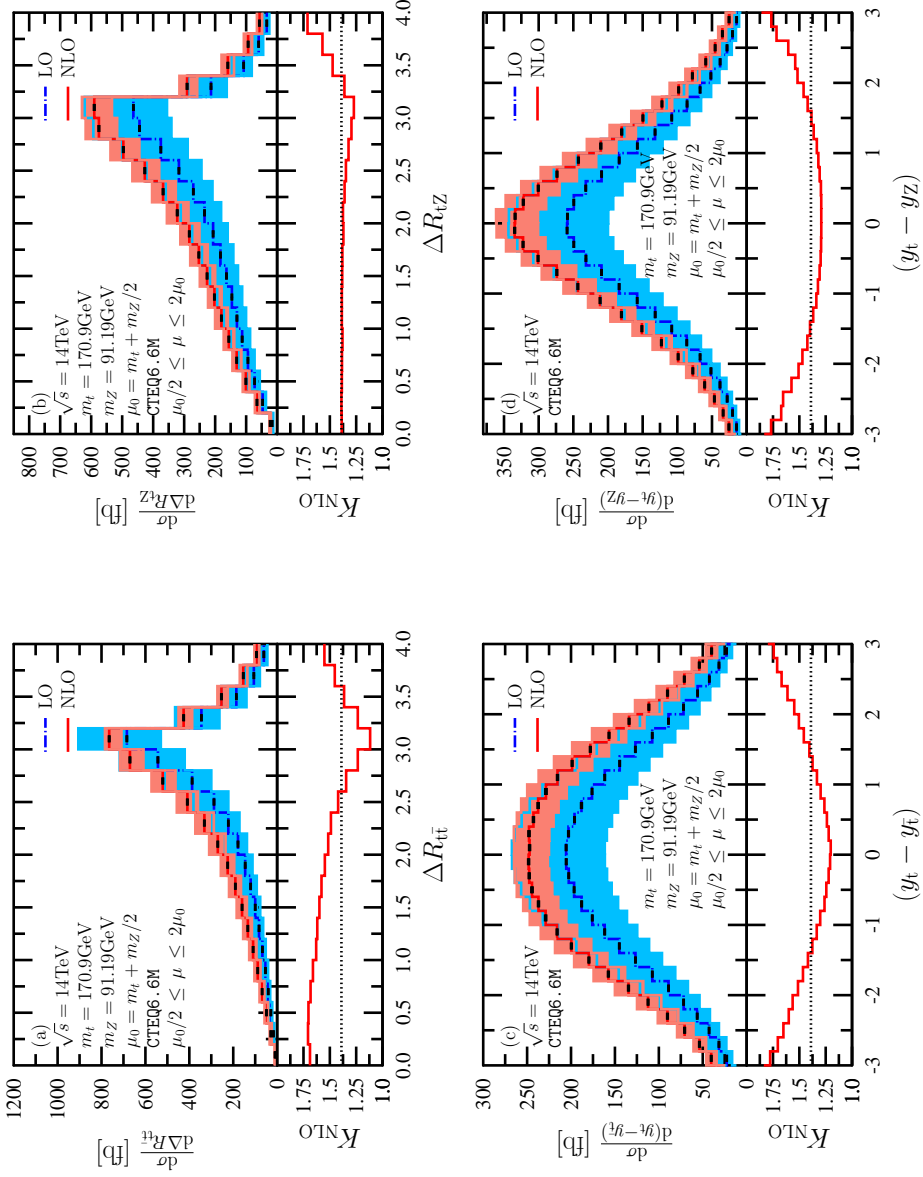


Figure 5.4: ΔR separations and rapidity differences for the 14 TeV LHC. The lower panel is the same as on the previous figure.

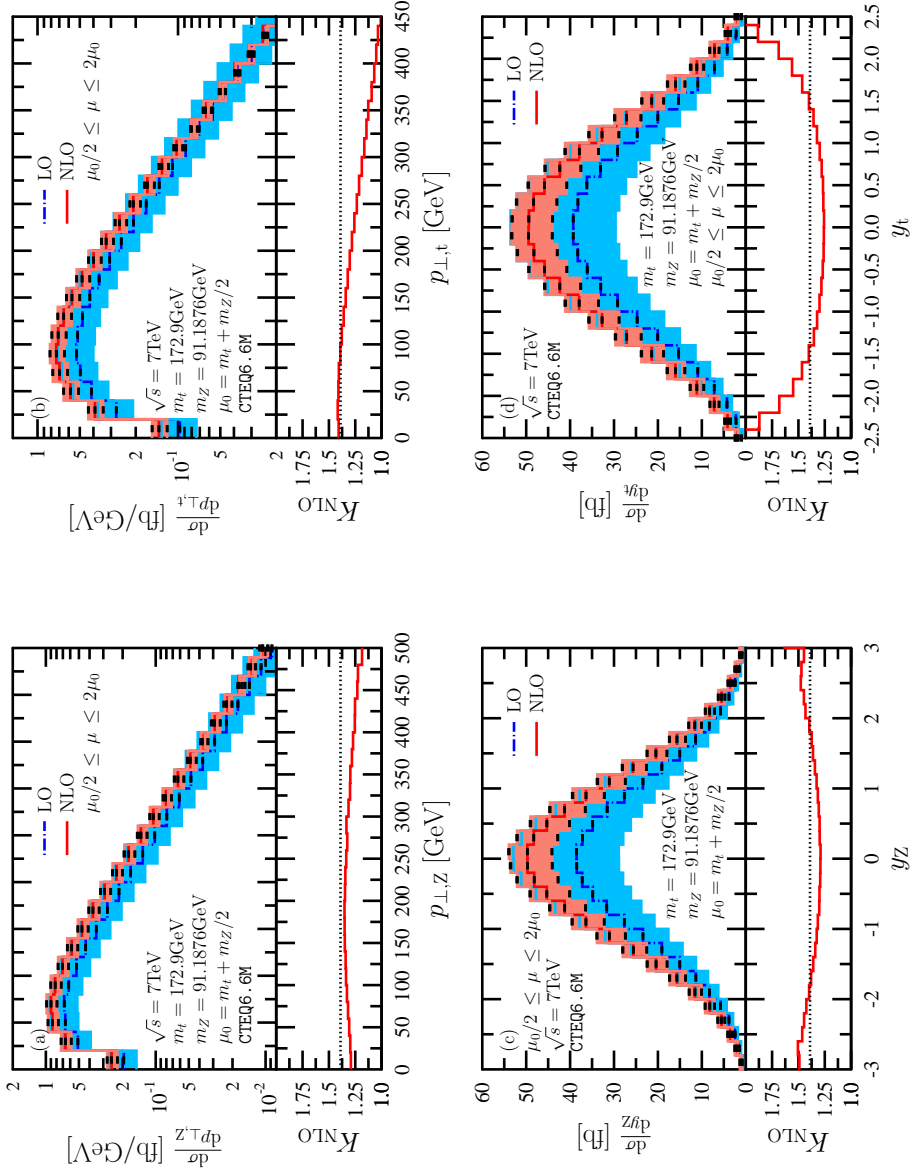


Figure 5.5: Top and Z p_{\perp} and rapidity distributions at the 7TeV LHC. The lower panel shows the NLO K -factor compared to the inclusive one $K_{\text{inc}} = 1.39$ obtained at 14TeV.

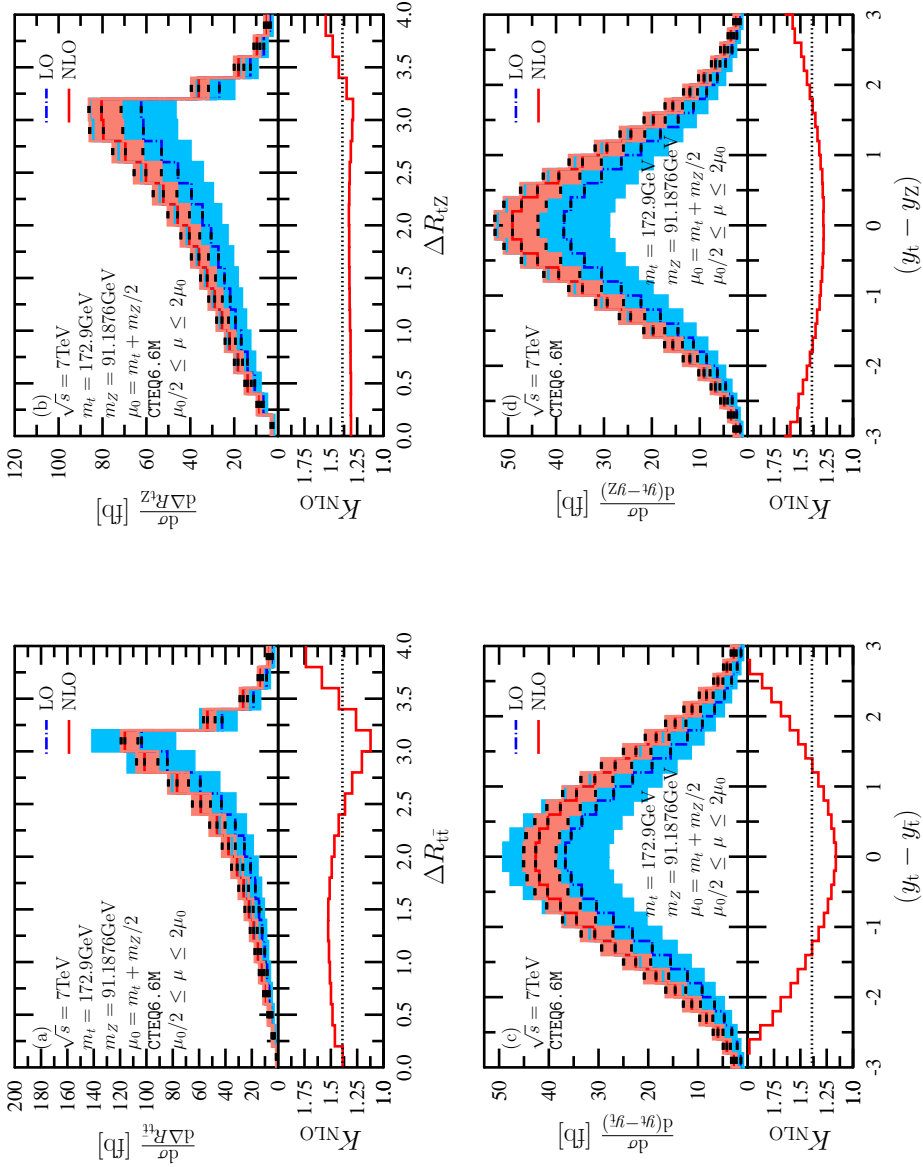


Figure 5.6: ΔR and rapidity separations of the $t\bar{t}$ and tZ systems at 7 TeV. The lower panels coincide with the ones on the previous figure.

5.3 Phenomenology

In the NLO calculation of $t\bar{t} + Z$ we considered the top-pair and also the Z -boson on-shell, e.g. as final state particles. In principle in an experiment it is possible to reconstruct the momenta for these particles, thus the plots presented above can also be measured by the experiments. However, we might not overcome the fact, that these particles decay, while the NLO calculation only can provide a partonic prediction. In a detector apparatus jets are observed with $\mathcal{O}(10)$ hadrons inside, hence a more precise prediction could be made if the partonic result could incorporate parton showering (e.g. filling the final state with soft and collinear partons emitted from the hard ones) and hadronization. Thus our aim is to use the capabilities of the PowHe1 framework to match the NLO calculation to parton shower algorithms.

To merge an NLO calculation to a parton shower algorithm we have to provide events which can be further showered. An event can have a Born- or real-emission-like kinematical configuration. These events should resemble NLO accuracy, that is the plots made with them should coincide with those obtained during the NLO integration. As we already pointed out higher order terms can turn up if the K -factor is too large.

The implementation of matching is checked at $\sqrt{s} = 7\text{TeV}$ LHC, with CTEQ6.6M PDF set from the LHAPDF library, with a 2-loop running α_s , 5 light flavors and $\Lambda_5^{\overline{\text{MS}}} = 226\text{MeV}$, $m_t = 172.9\text{GeV}$, $m_Z = 91.1876\text{GeV}$, $G_F = 1.16639 \times 10^{-5}\text{GeV}^{-2}$, the renormalization and factorization scale were chosen to the default $\mu_0 = m_t + m_Z/2$. To make the comparison we generated 3 million unweighted events, the plots are contained by Fig. 5.7. On this figure the p_\perp spectra and rapidity of the Z -boson and the top-quark are depicted. Considering the p_\perp spectra of the Z and top the agreement between the NLO calculation and the generated events is within 1 – 2%, as p_\perp increases the agreement stays within 5%. Taking a look at the lower panels, showing the ratio (LHEF/ exact NLO) and the uncertainty of the two calculations, it seems, that the decreasing accuracy can be accounted for the lower statistics. This is also suggested by the fact that the ratio of the calculations is oscillating around one. Considering the rapidity plots, in the central region the agreement is well below 1%, and away it the agreement decreases, but still stays within 5 – 10% (the agreement gets around 10% when $|y_{t,Z}| \approx 3$, on these figures only the $[-2.5, 2.5]$ range is shown). This time the uncertainty cannot be entirely accounted for the worse agreement in the forward (backward) direction, it is more likely that the low statistics and the increasing K -factor together are

responsible for the decrease in the agreement. This is also suggested by the fact that the rapidity distributions obtained from the events overshoot those obtained during the NLO calculation. We can conclude that the agreement between the NLO calculation and the event generation shows similar behavior as compared to the previously discussed processes implemented already, and suggesting that we have a good control over the event generation.

Next, we studied the SMC effects by comparing distributions obtained at different stages of the calculation: at the decay-level, e.g. when our top quarks are already decayed, but no parton showering or hadronization taken place, and at the SMC-level with full parton showering and hadronization. For this comparison we used events generated for the 7TeV LHC, and by using two generators for the parton showering and hadronization: PYTHIA 6.425 [91, 122] and HERWIG 6.520 [92, 123]. In both cases muons and neutral mesons are considered stable, for all the other particles the original setup was kept in both SMC programs. The total widths and masses are tuned to be the same in the two codes. The partial widths are determined by each code according to the built-in decay modes. Multiparticle interactions were turned off, and the intrinsic p_{\perp} spread of the valence partons in the incoming hadrons in HERWIG was assumed to be 2.5GeV.

The comparison is done without any selection cuts, since the particle content in the decayed and showered cases are different, e.g. at the decay-level we deal with partons, but at the full SMC-level we deal with hadrons. Only jet clustering is applied with the anti- k_{\perp} algorithm provided by FASTJET [113, 124] with $R = 0.4$. The comparison is depicted on Fig. 5.8 for various distributions. By taking a look at the p_{\perp} -spectrum of the hardest jet (p_{\perp, j_1}) an almost uniform softening is visible as going from the decay-level to the full-SMC, the amount of softening in the high- p_{\perp} region is around 20%, while at the low- p_{\perp} range the softening can reach a factor of 2 – 10. Roughly speaking it can be stated, that the softening realizes as an almost uniform one-bin shift to the softer region. In the case of the rapidity of the hardest jet the effect of parton showering and hadronization looks negligible and the small effect of parton showering seems to be homogeneous. This is expected, since the multiple soft and/or collinear emissions produced by the parton shower should not change the orientation of a jet, only its energy and p_{\perp} should be affected. On Fig. 5.8 we also plotted the H_{\perp} and the lepton p_{\perp} -distributions. For the H_{\perp} -distribution the following definition is used:

$$H_{\perp} = \sum_j p_{\perp}^j + p_{\perp}^{\ell^+} + p_{\perp}^{\ell^-} + \not{p}_{\perp}, \quad (5.2)$$

where the first term sums the transverse momenta of jets, $p_{\perp}^{\ell^-}$ ($p_{\perp}^{\ell^+}$) is the p_{\perp} of the (anti)lepton, while \cancel{p}_{\perp} is the missing transverse momentum. Taking a look at this distribution the effect of the parton showering looks apparent, that is a non-homogeneous hardening can be seen. Below 500GeV the agreement between the two parton shower programs decreases and reaches a difference in the order of 50%. Finally on the $p_{\perp,\ell}$ -distribution we can see that no effect is coming from the parton showering. This is expected, since the fine structure constant is much less than α_s , hence the photon radiation coming from fermions is suppressed compared to the parton showering coming from the original hard partons. In the low p_{\perp} -region the increase in the rate can be accounted for being due to soft lepton-pair production coming from photon radiation.

With this setup used for the SMC programs we were able to find agreement among them. Even though these SMC's show conceptual differences regarding the ordering variables and the hadronization models, the deviation was within a few percents. We report worse agreement in the low lying region of the H_{\perp} -distribution and in the rapidity distribution for the hardest jet. For the H_{\perp} -distribution PYTHIA predicts a larger rate for small H_{\perp} , while for the rapidity the HERWIG prediction looks more central compared to the PYTHIA one.

After a rigorous check of the matching procedure we turn our attention to make the first predictions for the LHC at 7TeV. We do this by applying a set of cuts inspired by the actual ones employed by the experiments. In order to make our predictions we used the Perugia 2011 tune for PYTHIA, which is considered the latest LO tune available [125] in the time of writing this thesis. This tune is made by taking into account recent LHC data as well. Additionally it turns PYTHIA into a k_{\perp} -ordered PS. The original PYTHIA was a virtuality ordered shower, where the shower evolution was governed by the virtuality (t) of the partons, while in the case of a k_{\perp} ordered shower the ordering variable is the relative k_{\perp} of the splitting parton pair. The effect of this tune was visible in the rate, since the showered results produced by PYTHIA show an increase of about 10% compared to the original HERWIG, which is an angular ordered shower algorithm.

Considering the $t\bar{t} + Z$ hadroproduction as a signal process a large background comes from the $t\bar{t} + j$ process. As it is stated in [72] the missing energy can be used on events having missing transverse momentum, a b- and an anti-b-jet and 4 ordinary jets to isolate the signal from the background. As we will see below the proposed cuts are exclusive and aim to select the $Z \rightarrow \nu\bar{\nu}$ decay-channel with hadronically decaying top and antitop. This set of cuts was originally proposed for measuring the Z coupling to the top and tested at LO without the effect of parton

showering, hadronization and higher order effects. It is a useful task to test its viability to be used with higher order corrections including parton showering and hadronization. When this original set of cuts was proposed only the 14TeV LHC was considered, hence it is interesting to analyze the behavior of these cuts with a presently available LHC energy.

In the 7TeV LHC case the cross section obtained after cuts decreased almost one order of magnitude, hence to reach reasonable results it would demand really large statistics from the experiments.

Since in this calculation several cuts are used, which can strongly affect the cross section, we considered two sets, one is the complete set of cuts used by Ref. [72], while the other is a less restrictive one. When we constructed the less restrictive set of cuts we tried to isolate those ones, which significantly decrease the cross section and only keep the remaining ones. The subset of cuts is the following:

1. At least six jets are demanded with $|y_j| < 2.5$.
2. Among the reconstructed jets a b and an \bar{b} jet are demanded.
3. For b and \bar{b} jets $p_{\perp}^b > 20\text{GeV}$.
4. For the non-b jets $p_{\perp}^{\text{non-b}} > 30\text{GeV}$.
5. For at least three jets (b or non-b) $p_{\perp}^j > 50\text{GeV}$.
6. For jet reconstruction $\Delta R(j, j) > 0.4$, where $\Delta R = \sqrt{\Delta\phi^2 + \Delta y^2}$, where $\Delta\phi$ is the azimuth angle separation and Δy is the rapidity separation.
7. $\Delta\phi(p_{\perp}, p_{\perp j}) > 100^\circ$, where $p_{\perp j} = p_{\perp}(\hat{b}_1) + p_{\perp}(\hat{b}_2)$ for an explanation on \hat{b}_1, \hat{b}_2 see the text below.
8. $\Delta\phi(p_{\perp}, p_{\perp j}) > 100^\circ$, where $p_{\perp j} = p_{\perp}(\hat{j}_1) + p_{\perp}(\hat{j}_2) + p_{\perp}(\hat{j}_3) + p_{\perp}(\hat{j}_4)$, for an explanation on $\hat{j}_1, \hat{j}_2, \hat{j}_3, \hat{j}_4$ see the next paragraph.

This set of cuts are created to enhance the $Z \rightarrow \nu \bar{\nu}$ decay-channel with hadronically decaying top and antitop. Hence we should have a b-, an \bar{b} - and four additional jets, which allow for the best $t \rightarrow b W^+ \rightarrow b j j$ and $\bar{t} \rightarrow \bar{b} W^- \rightarrow \bar{b} j j$ reconstruction. These jets are labeled as $\hat{b}_1, \hat{b}_2, \hat{j}_1, \hat{j}_2, \hat{j}_3, \hat{j}_4$. This reconstruction is

done by minimizing

$$\chi^2(b_1 j_1 j_2; \bar{b}_2 j_3 j_4) = \frac{(m_{j_1 j_2} - m_W)^2}{\sigma_W^2} + \frac{(m_{j_3 j_4} - m_W)^2}{\sigma_W^2} + \frac{(m_{b_1 j_1 j_2} - m_t)^2}{\sigma_t^2} + \frac{(m_{\bar{b}_2 j_3 j_4} - m_t)^2}{\sigma_t^2}, \quad (5.3)$$

where $m_{j_k j_l}$ and $m_{b_i j_k j_l}$ are the invariant masses corresponding to jet combinations j_k, j_l and b_i, j_k, j_l respectively. To identify the jets coming from the top and antitop decays the resolution of the reconstruction should be defined. During this calculation we used the values $\sigma_W = 7.8\text{GeV}$ and $\sigma_t = 13.4\text{GeV}$ taken from Ref. [126]. In our analysis we select the b and \bar{b} jets by means of MCTRUTH, although in an experiment a b jet cannot be distinguished from an \bar{b} jet, hence in an experimental analysis the demand of a b and an \bar{b} jet has to be changed to two b jets.

On Fig. 5.9 we depicted four sample distributions for the restricted set of cuts. On these plots we compared the result after parton showering and hadronization (full SMC) to the result obtained by only performing the top and antitop decays. The p_\perp -distribution for the hardest jet shows a softening and a decrease in the total rate due to the presence of parton showering. The decrease of the total rate can be seen on its rapidity distribution too, though the decrease looks uniform. The uniform decrease can be accounted for the parton showering not changing the rapidity of the jet only it's particle content and energy is affected. We also tried to reconstruct the top and W^+ mass. To do so we tried to identify those jets that come from the top, antitop, W^+ and W^- decays by minimizing the χ^2 in Eq. (5.3). On Fig. 5.9.(c) we plotted the invariant mass of those three jets which are identified as the top decay products. When only decay is used without any further hadronization or parton showering a clear peak is visible, but this is completely washed away by the parton shower. The parton shower can put partons outside of the jet cone. Hence it can push the invariant mass of the three candidate jets away from the top quark mass. Furthermore the R parameter used for jet reconstruction is small. Hence the parton shower can introduce further jets, thus the decay products of the top quark, considering a hadronic decay, can tend to resemble more than three jets. This makes impossible to reconstruct the top mass out of three jets. By taking a look at Fig. 5.9.(d) we can conclude that the efficiency of the reduced set of cuts is low because we not only select those two jets that are the decay products of the W^+ (or W^-) decay, but also those that come from the hadronic decay of the Z . The result obtained with full SMC shows

exactly the same behavior as already seen in the case of the three-jet invariant mass. The parton shower smears the peaks. As apparent from the presence of the Z -peak in m_{jj} the used subset of cuts is not efficient enough in selecting events with Z decaying into a neutrino-pair. Thus further cuts are needed to enhance the selection of the $Z \rightarrow \nu \bar{\nu}$ channel.

We would like to measure the coupling of the Z to the top quark in the $Z \rightarrow \nu \bar{\nu}$ channel, although several other processes can contribute as background such a process is the $t\bar{t} + j$ production, (for the full list of possible background processes see Ref. [72]). To illustrate the size of the background contribution on Fig. 5.10 we showed the m_{bjj} invariant mass again for signal and for one important background process, $t\bar{t} + j$ production, at various levels with two different cut setups. As we can see from the green dashed line, which spans over the whole abscissa range the background overwhelms the signal by more than two orders of magnitude. Thus further cuts should be applied to decrease the background well below the signal. Following the footsteps of Ref. [72] we introduced the following two cuts:

- Cut on the missing transverse momentum: $p_{\perp} > 5\text{GeV}^{1/2} \sqrt{\sum_j p_{\perp}^j}$. This, together with the cut on the minimal number of jets, can more efficiently select those events where the Z decays into a neutrino and antineutrino pair.
- To accept an event we impose $\chi_{\min}^2 < 3$, where χ_{\min}^2 is the minimal value of χ^2 defined in Eq. (5.3).

Since in an experiment individual neutrinos cannot be detected, the missing transverse momentum is calculated from the visible objects, e.g. jets, leptons and antileptons. Considering the momenta of all final state particles, the transverse component of the vectorial sum of these momenta should be zero, hence due to momentum conservation the transverse momentum of the system of invisible particles should coincide with the transverse momentum of the remaining ones, which can be detected. In an experiment, or at the full SMC level, determination of missing transverse momentum is hampered by the possible contribution from the decay of B hadrons. Furthermore the event can have several jets with low energy, hence not contributing to the visible sum of momenta. At the decay-level or at the parton-level of Ref. [72] there was no such a problem since no hadronization took place in these cases.

On Fig. 5.10 we also listed the plots obtained with the additional two cuts. These distributions span only in a limited abscissa range. On this figure the full

SMC prediction is depicted as well for the signal process with the full set of cuts applied. As apparent when the parton showering is turned on, the reconstructed top peak is completely smeared away. On the other hand the efficiency of selecting those events where the Z decays into a neutrino-pair is raised. By only judging from this figure, although the efficiency is increased to select the certain decay mode of the Z , the background is still overwhelming it. By having a look at the missing transverse momentum plot on Fig. 5.11 it seems that the background overwhelms the signal at low and moderate p_{\perp} values, but the background is steeper, hence at around 300GeV the signal overcomes it providing the possibility of measurement. On Fig. 5.11 we only listed the case where decay was employed only, but the same effect can be seen also when the full SMC is applied to the background and signal, although the p_{\perp} -distribution for $t\bar{t} + j$ isn't so steep as in the decay case.

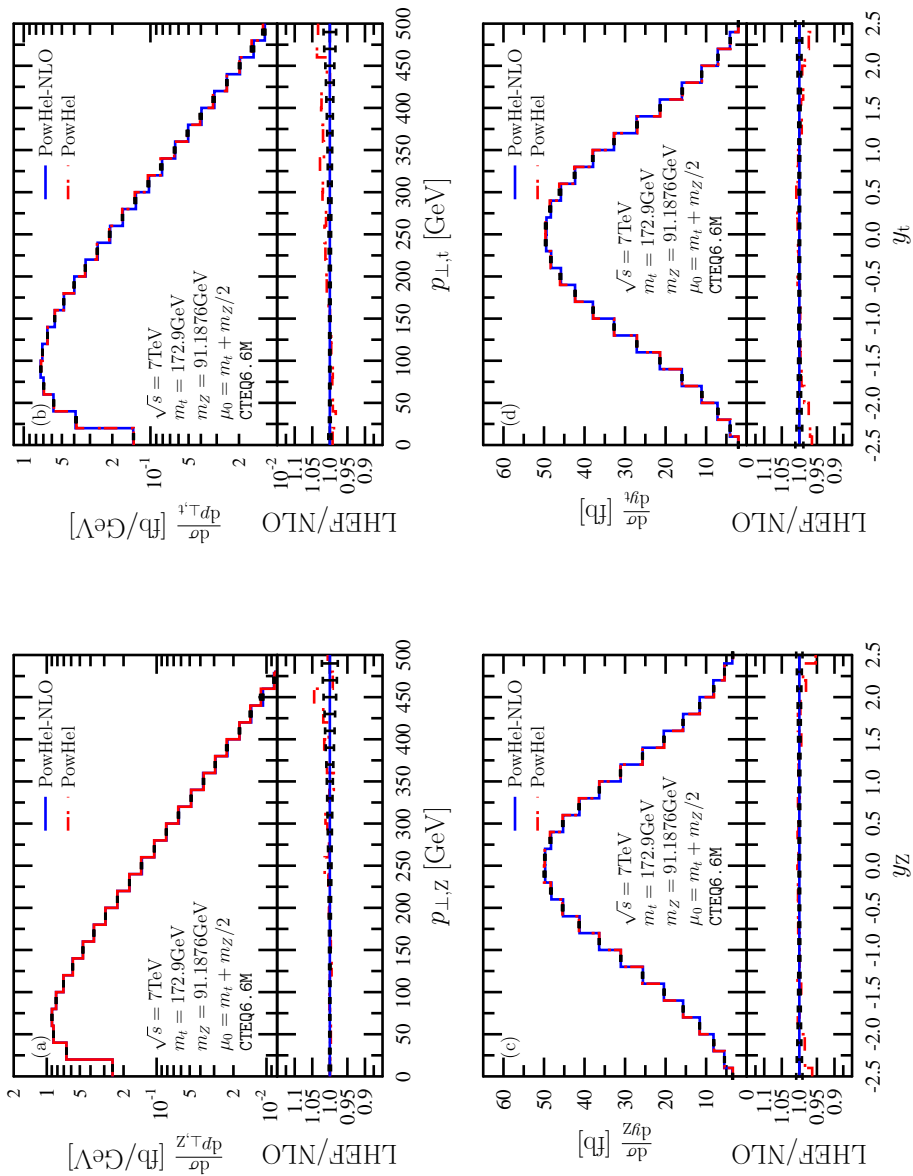


Figure 5.7: This figure shows the comparison of the exact NLO calculation to generated events at $\sqrt{s} = 7\text{TeV}$ at the LHC. The p_{\perp} and rapidity are shown for the Z-boson and for the top quark.

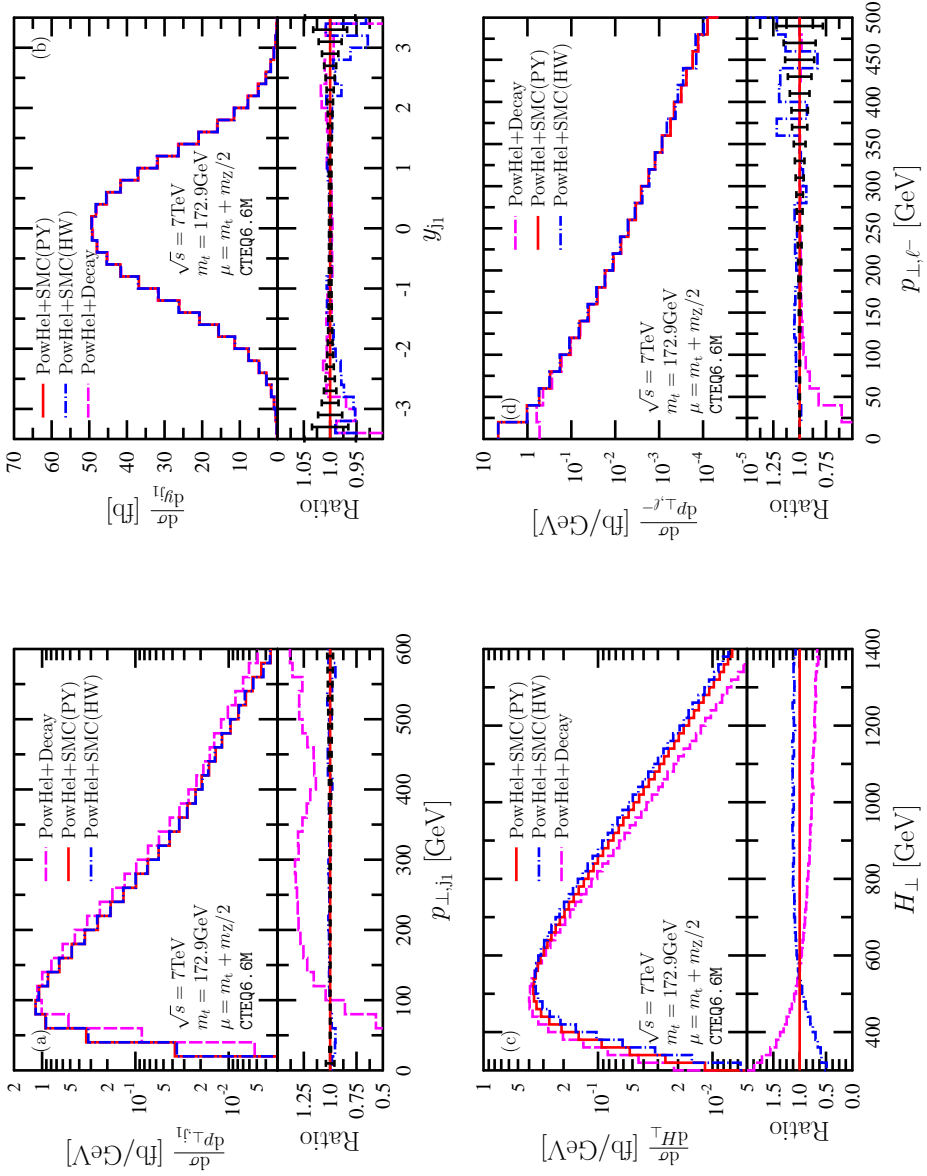


Figure 5.8: Distributions obtained for the 7 TeV LHC in the case when only jet reconstruction was applied. On the lower panel the following ratios are shown: Decay/SMC(PY) and SMC(HW)/SMC(PY).

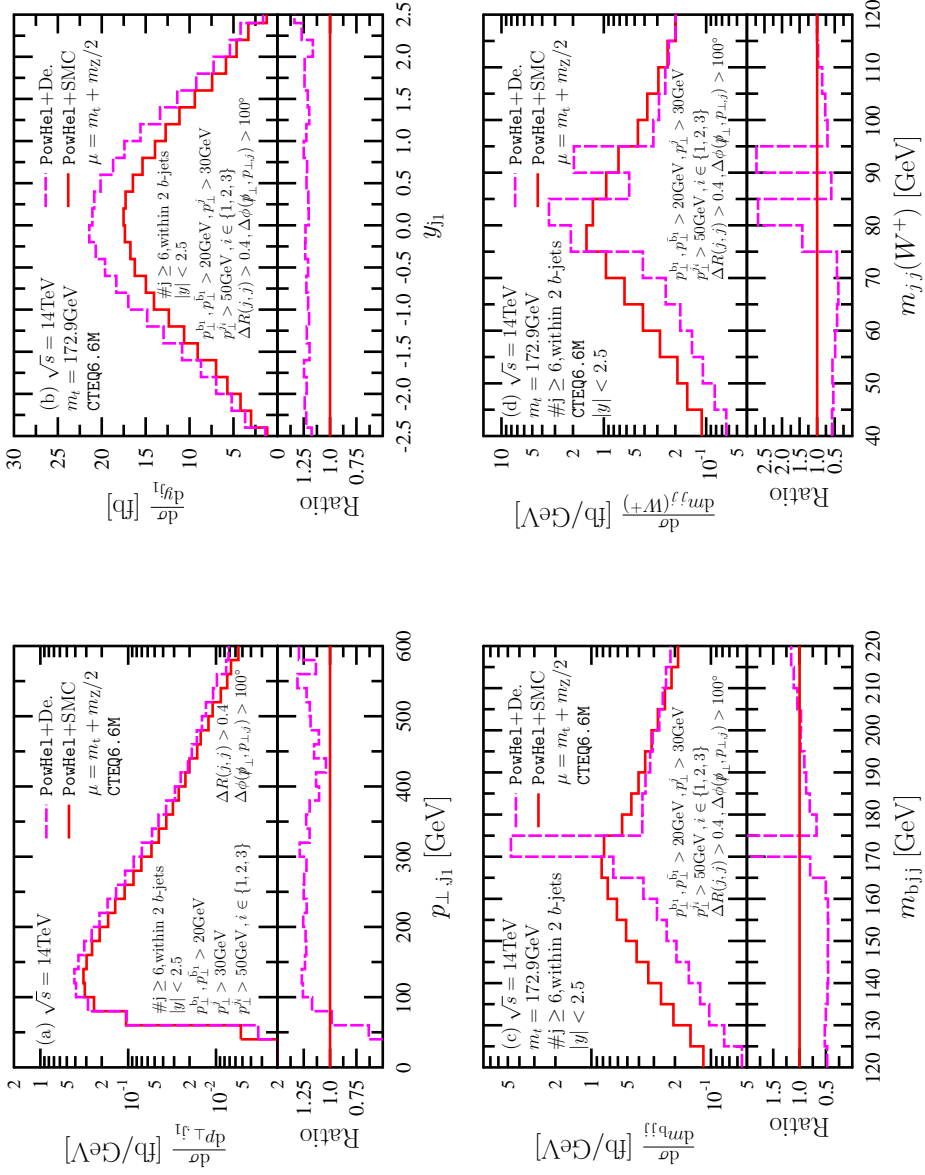


Figure 5.9: Sample distributions obtained for the 14 TeV LHC with the restricted set of cuts.

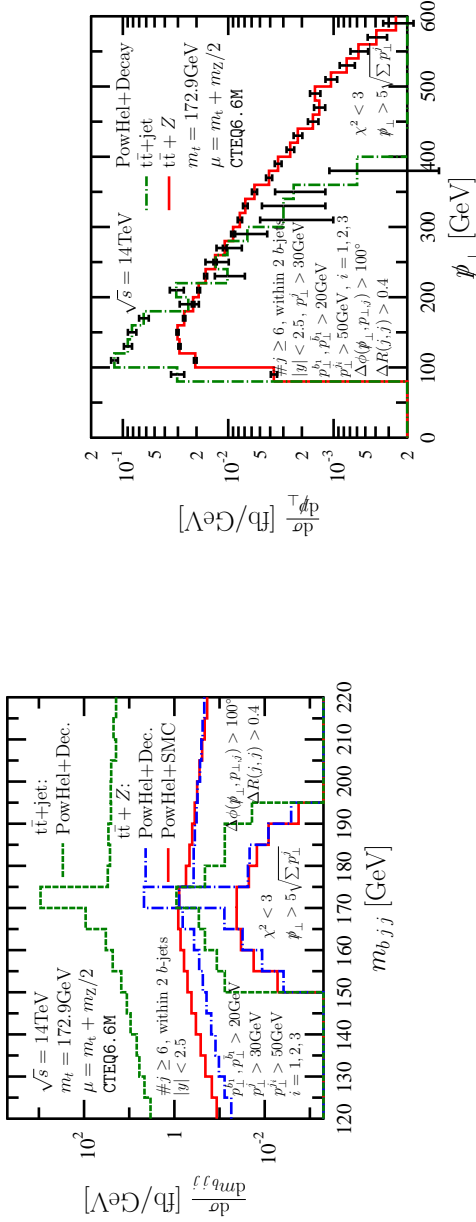


Figure 5.10: Invariant mass distribution for the reconstructed top quark at the decay (blue dashed-dotted lines) and the full SMC level (solid red lines) for the $t\bar{t} + Z$ production, and at the decay level for the $t\bar{t} + j$ background (green dashed lines) with the reduced set of cuts (distributions spans over the whole abscissa range) and with the full set of cuts (distributions spans only over a limited abscissa range).

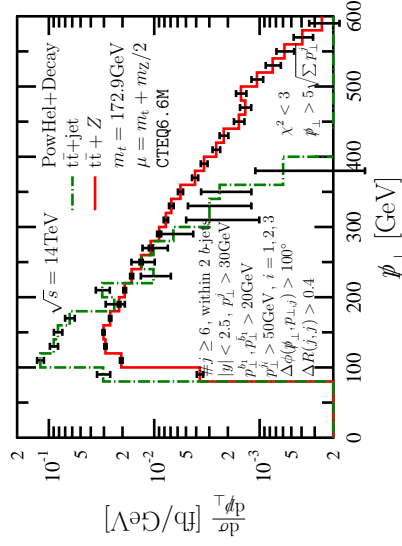


Figure 5.11: Missing transverse momentum distribution for the signal ($t\bar{t} + Z$, solid line) and one possible background ($t\bar{t} + j$, dash-dotted line) after decay with the full set of cuts.

Chapter 6

$t\bar{t} + W^\pm$ production

The hadroproduction of $t\bar{t}$ -pairs in association with vector bosons is an important process for measuring top couplings, and detecting if anomalies, possibly related to physics beyond the Standard Model (SM), can manifest themselves. Furthermore, it can be considered a background process for new physics searches. In particular, the dilepton decay channel with two same-sign leptons, accompanied by missing energy and jets, is a relatively rare channel in the SM, but largely exploited in recent supersymmetry searches [127]. From the experimental point of view, these studies are becoming feasible thanks to the increasing amount of data collected at the LHC, that has already reached an integrated luminosity large enough to permit the disentangling of $t\bar{t} + V$ signals over other SM backgrounds [128]. Such an investigation can certainly benefit from high accuracy theoretical tools, involving the inclusion of radiative corrections, at least in QCD, and the matching to Parton Shower (PS) approaches.

The aim of this chapter is to provide predictions for $t\bar{t} + V$ production (with $V = W^+, W^-, Z$) at LHC at both NLO and NLO + PS accuracy. In case of NLO we also include uncertainties due to factorization and renormalization scale variation, always assumed being equal to each other for this process. This is achieved by PowHel, our event generator relying on the POWHEG-BOX [68] computer framework designed for matching predictions at NLO accuracy in QCD to a PS evolution, according to the POWHEG method [64, 129]. As we saw in earlier chapters the input matrix elements are obtained from the HELAC-NLO package [130]. With such an input, the POWHEG-BOX is capable of making predictions at both NLO accuracy, and at NLO accuracy matched to a PS evolution. We especially concentrate

on the $\sqrt{s} = 7$ and 8 TeV energies, but the approach can easily be extended to other ones (and to other colliders). So far, in an earlier chapter, we also presented some theoretical results on $t\bar{t} + Z$ production itself, at NLO accuracy, and a phenomenological study limited to its decay channel in six jets plus missing energy, at NLO + PS accuracy.

In this chapter we produce predictions for $t\bar{t} + W^\pm$ hadroproduction, and we concentrate on the (semi)leptonic decay channels of $t\bar{t} + Z$, the same channels that are nowadays preferred by the experimental collaborations, as much cleaner signals can be obtained with respect to the fully hadronic decay one. The $t\bar{t} + W^\pm$ hadroproduction has already been recently investigated by MCFM at the NLO accuracy in QCD [131]. Our study provides a completely independent confirmation of their results at the parton level, with which we found agreement within the quoted uncertainties. Furthermore, we give predictions for this process at the hadron level, by the matching the NLO predictions to the PYTHIA [91] and HERWIG [92] Shower Monte Carlo (SMC) programs, describing PS emissions, hadronization and hadron decays.

6.1 Implementation and checks

We address the problem of matching $t\bar{t} + V$ ($V = Z, W^\pm$) production at NLO level to PS programs. To this end the POWHEG approach [64, 129] was chosen as implemented in POWHEG-BOX [68]. Details on the implementation of $t\bar{t} + Z$ in this framework were introduced in the previous chapter. The following ingredients, needed by POWHEG-BOX, were provided in case of $t\bar{t} + W^\pm$ hadroproduction:

- The phase space corresponding to three massive particles in the final state was provided in full analogy with our previous computations of the $t\bar{t} + Z$ and $t\bar{t} + H$ processes at the same accuracy [105, 132].
- The Born and real-emission matrix elements corresponding to the $q\bar{q}'t\bar{t}W^\pm \rightarrow 0$ and $q\bar{q}'t\bar{t}W^\pm g \rightarrow 0$ processes, respectively, with $q, q' \in \{u, d, c, s\}$, were provided by HELAC-NLO [130].
- The finite part of the virtual amplitudes was computed by HELAC-1LOOP [71] for the $q\bar{q}'t\bar{t}W^\pm \rightarrow 0$ processes.
- At both tree- and one-loop-level the remaining matrix elements were obtained by crossing.

- The spin- and color-correlated Born squared matrix elements were also provided by HELAC-NLO.

The PowHel (= POWHEG-BOX + HELAC-NLO) code implemented this way is capable of generating Les Houches Events (LHE's), including up to first radiation emission, for both $t\bar{t} + W^+$ and $t\bar{t} + W^-$. A selection between these two cases can simply be achieved by setting the `Wmode` keyword in the input card to ± 1 .

In order to make comparison with the available NLO predictions [131], we had to use a non-diagonal CKM matrix in the calculation. We thus extended HELAC-1LOOP in this respect. This process can then be considered the first one, among those computed with HELAC-1LOOP, where a non-diagonal CKM matrix was used. A check of the correctness of the implementation was provided by comparing our results with those already available in the literature (see the next paragraph), obtained in the same non-diagonal conditions. We make available the PowHel implementation, where the user has the possibility of switching from the diagonal CKM matrix to a non-diagonal one by specifying a positive value of the `sin2cabibbo` keyword in the input card, which declares $\sin^2 \theta_C$.

In order to assess the correctness of the implementation, the standard set of checks was performed also in this case. The consistency between the real emission matrix elements, the Born part, and the real counterterms automatically computed according to the FKS subtraction scheme [56], was checked by investigating the behavior of these terms in all kinematically singular regions of phase space. The original and crossed matrix elements computed by PowHel were checked against those provided by HELAC-PHEGAS and HELAC-1LOOP in various randomly chosen phase space points. As for $t\bar{t} + W^\pm$, the Born results were checked against MCFM [133, 134], and the NLO ones against the predictions quoted in Ref. [131], using the same set of parameters mentioned therein and $\sin^2 \theta_C = 4.9284 \cdot 10^{-2}$, as in the default version of MCFM. In all cases we found full agreement.

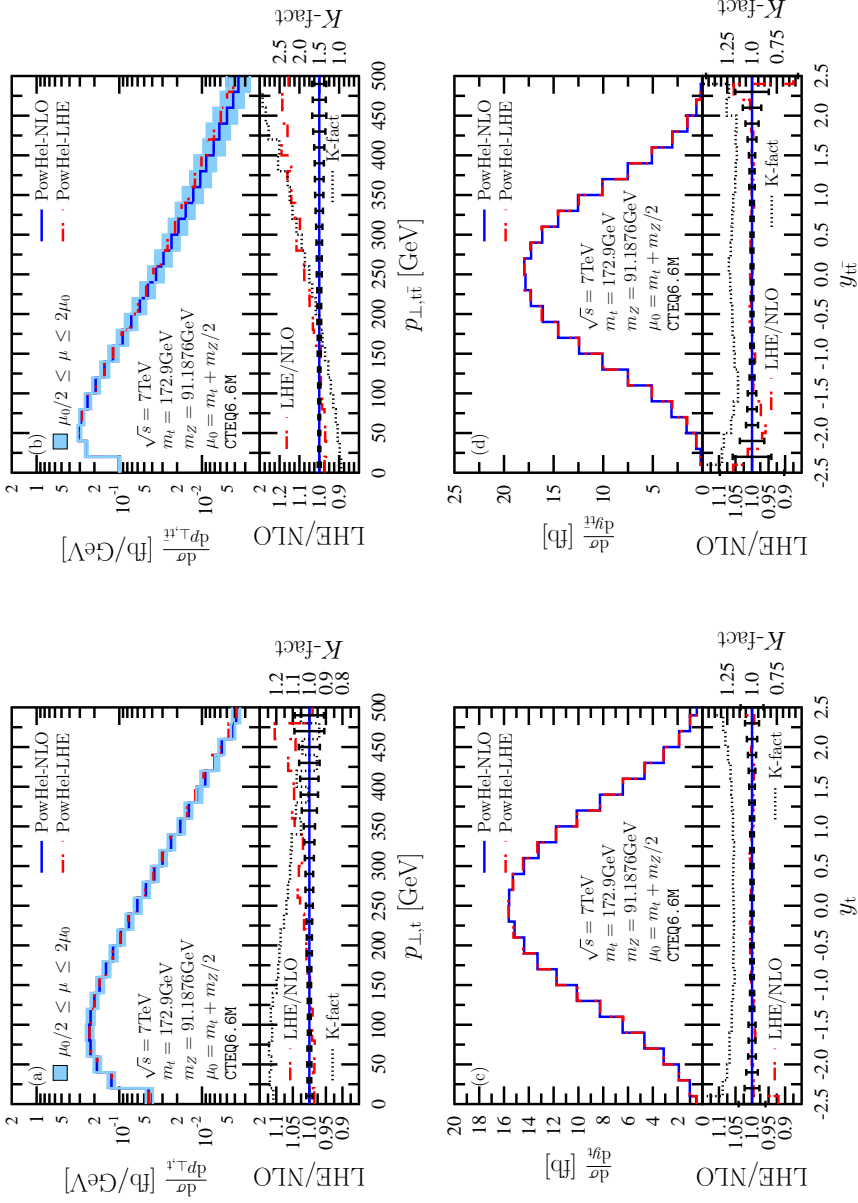
We also compute NLO $t\bar{t} + W^\pm$ cross-sections at the LHC for a different static central scale choice, by considering the interval $[\mu_0/2, 2\mu_0]$ centered around $\mu_0 = m_t + m_V/2$, and the following set of parameters: $\sqrt{s} = 7$ and 8 TeV, the CTEQ6.6M PDF set with a 2-loop running α_s and 5 active flavors, taken from LHAPDF [110], $m_b = 0$, whereas as for heavy particle masses, the latest available values provided by the PDG [96], i.e. $m_t = 173.5$ GeV, $m_W = 80.385$ GeV and $m_Z = 91.1876$ GeV, were adopted. For the whole calculation a non-diagonal CKM-matrix was used, in the first two families, with $\sin^2 \theta_C = 4.9284 \cdot 10^{-2}$. The renormalization and factorization scales were fixed to μ_0 . The predictions for the total NLO cross-sections in these conditions are shown in Table 6.1. The

considered scale choice turned out to provide a flatter scale dependence with respect to the case $\mu_0 = m_t$, as can be understood by comparing the results quoted in Table 6.1 to those provided in Ref. [131].

Although the K-factor associated to the $t\bar{t} + W^\pm$ process is close to one, it is also informative to compare NLO differential cross-sections to those obtained from the LHE's, which checks the correctness of the matching procedure. Sample distributions can be found in Figs. 6.1 and 6.2, where the transverse momenta and the rapidities of both the t-quark and the $t\bar{t}$ -pair are shown in case of $t\bar{t} + W^+$ and $t\bar{t} + W^-$, respectively, together with the ratio of the predictions from the LHE's to the NLO ones. In the figures in the lower panels the red dash-dotted line corresponds to the LHE/NLO ratio, whereas the differential K-factor (NLO/LO) is depicted with a dotted line. The error-bars refer to the statistical uncertainties on the LHE/NLO ratio. In case of p_\perp -distributions, the scale dependence is also superimposed as a light-blue band, which represents a scale variation between $\mu_0/2$ and $2\mu_0$. The agreement between the NLO and the LHE distributions is quite remarkable, as can be seen from the two rapidity plots and from the p_\perp -distribution of the t-quark. The small deviation visible in the $p_{\perp,t}$ tail is within the increased statistical uncertainty in that region, also plotted in the lower inset of each panel. For the $p_{\perp,t\bar{t}}$ -distribution the agreement is within 5% up to $\simeq 220$ GeV, but worsens in the high momentum tail. We attribute this increasing difference to the increasing K-factor that reaches 2 around 400 GeV (also depicted in the lower panel of the plot). This 10% deviation however, is well within the NLO scale dependence, as seen from the upper panel, where the uncertainty band, corresponding to a scale-variation in the $[\mu_0/2, 2\mu_0]$ interval, is shown as well.

| | \sqrt{s} (TeV) | μ | σ^{LO} (fb) | σ^{NLO} (fb) | \mathcal{K} -fact. |
|------------------|------------------|-----------|---------------------------|----------------------------|----------------------|
| $t\bar{t} + W^+$ | 7 | $\mu_0/2$ | 121.8(1) | 114.3(1) | 1.13 |
| | | μ_0 | 93.1(1) | 104.7(1) | |
| | | $2\mu_0$ | 72.7(1) | 93.8(1) | |
| | 8 | $\mu_0/2$ | 159.3(1) | 156.2(2) | 1.16 |
| | | μ_0 | 122.9(1) | 142.6(2) | |
| | | $2\mu_0$ | 96.7(1) | 127.5(1) | |
| $t\bar{t} + W^-$ | 7 | $\mu_0/2$ | 46.7(1) | 46.9(1) | 1.20 |
| | | μ_0 | 35.6(1) | 42.6(1) | |
| | | $2\mu_0$ | 27.8(1) | 38.0(1) | |
| | 8 | $\mu_0/2$ | 64.1(1) | 67.1(1) | 1.23 |
| | | μ_0 | 49.4(1) | 60.5(1) | |
| | | $2\mu_0$ | 38.9(1) | 53.9(1) | |
| $t\bar{t} + Z$ | 7 | $\mu_0/2$ | 141.6(1) | 149.4(2) | 1.32 |
| | | μ_0 | 103.5(1) | 136.9(1) | |
| | | $2\mu_0$ | 77.8(1) | 120.8(1) | |
| | 8 | $\mu_0/2$ | 209.5(1) | 224.9(4) | 1.34 |
| | | μ_0 | 153.9(1) | 205.7(2) | |
| | | $2\mu_0$ | 116.2(1) | 181.7(2) | |

Table 6.1: PowHel predictions for the inclusive $t\bar{t} + W^+$, $t\bar{t} + W^-$ and $t\bar{t} + Z$ cross-sections at LO and NLO QCD accuracy at LHC for $\sqrt{s} = 7$ and 8 TeV, for various static scale choices, centered around $\mu_0 = m_t + m_V/2$, with $V = W$ for the $t\bar{t} + W^\pm$ cases and Z for the $t\bar{t} + Z$ one. The statistical uncertainties of our simulations are shown in parentheses.

Figure 6.2: Same as Fig. 6.1, as for $t\bar{t} + W^-$ production.

Differential K-factors and the comparison between NLO and LHE distributions in case of the $t\bar{t} + Z$ process can be found in the previous chapter and also in Ref. [132, 135]

6.2 Phenomenology

For our phenomenological studies the following parameters were adopted in PowHe1: the CTEQ6.6M PDF set, with a 2-loop running α_s , $m_t = 172.5$ GeV, $m_W = 80.385$ GeV, $m_Z = 91.1876$ GeV, $\sin^2 \theta_C = 4.9284 \cdot 10^{-2}$. The renormalization and factorization scales were fixed to $\mu_R = \mu_F = m_t + m_V/2$. Although the value of m_t is different from the most recent measurements at the LHC and also from that used in our NLO comparisons, it was also used in Ref. [131] and in several measurements performed by the LHC experiments so far.

The PowHe1 code generates LHE's of two kinds: Born-like events, and events including first radiation emission. Further emissions can be simulated by simply showering the events by SMC programs, under the condition that the first emission remains the hardest. We consider the last fortran version of both the PYTHIA and HERWIG SMC, providing a virtuality-ordered and an angular-ordered PS, respectively. As the ordering variable in the POWHEG method is the relative transverse momentum, in case of an angular-ordered PS parton emissions with larger transverse momentum than the first one have to be vetoed explicitly (done in HERWIG automatically). Furthermore, a truncated shower, simulating wide-angle soft emission before the hardest one ought to be included, too. However, the effect of the truncated shower in general turns out to be small, as shown e.g. in Ref. [136] and as we already verified in case of many different multiparticle production processes including a $t\bar{t}$ pair, where the predictions of PYTHIA and HERWIG turn out to agree one with each other within a few percent. Thus, we neglect truncated shower contributions in this analysis, as we already did in our previous ones.

These SMC codes were also used to generate t-quark and heavy boson decays (neglecting spin correlations), as well as hadronization and hadron decays. For consistency, heavy particle masses in the SMC setup were set to the same values used in the PowHe1 computation, whereas the light quark masses in HERWIG were set to the default values implemented in PYTHIA. Heavy particle decay widths were fixed to $\Gamma_t = 1.45775$ GeV, $\Gamma_W = 2.085$ GeV and $\Gamma_Z = 2.4952$ GeV. Decays of heavy bosons into electrons were assumed to have the same branching ratio as into muons. π^0 's were enforced to be stable in both SMC's, as they can be

easily reconstructed in the experiments from their decay products (2 γ 's), and muon stability is enforced in HERWIG, as in PYTHIA default configuration. All other particles and hadrons were assumed to be stable or to decay according to the default implementation of each SMC. Multiple interactions were neglected in both SMC's.

6.2.1 Inclusive analysis

We now present predictions at the SMC level, i.e. after PS, hadronization and hadron decay, in case of $t\bar{t} + W^+$, $t\bar{t} + W^-$ and $t\bar{t} + Z$ in the most general case, i.e. without applying any selection cut. This is possible since these processes are finite at the Born level, so we did not have to introduce any technical cut in the PowHel generation of LHE's. It is useful and instructive to present some theoretical distributions at this level, to better understand how the selection cuts that we will discuss in the following will modify these predictions. In particular, we focus on a few selected distributions that will also be shown again, in presence of cuts, in the following Subsections.

The inclusive cross-sections at the SMC level are the same as at the NLO level, since the POWHEG method ensures that the cross-sections from LHE's coincide with the exact NLO ones, i.e. $\sigma_{\text{LHE}} = \sigma_{\text{NLO}}$. We found that $\sigma_{t\bar{t}+Z} > \sigma_{t\bar{t}+W^+} > \sigma_{t\bar{t}+W^-}$, with $\sigma_{t\bar{t}+Z} = 137.21 \pm 0.01$ fb, $\sigma_{t\bar{t}+W^+} = 106.74 \pm 0.01$ fb and $\sigma_{t\bar{t}+W^-} = 43.472 \pm 0.005$ fb, respectively (uncertainties are statistical only). These values are slightly larger than those quoted in Table 6.1, due to the slightly smaller value of the t-quark mass (see the beginning of the previous subsection).

The invariant mass of all same-flavor (ℓ^+ , ℓ^-) pairs in all events is plotted in Fig. 6.3.a. Even in absence of cuts, a peak is well visible in the $t\bar{t} + Z$ distribution, around the Z pole mass, due to $Z \rightarrow \ell^+\ell^-$ decays. The e^+e^- and $\mu^+\mu^-$ channels both contribute with a similar shape to this distribution. The presence of this peak, absent in the $t\bar{t} + W^+$ and $t\bar{t} + W^-$ distributions also plotted in Fig. 6.3.a, will be exploited in the trilepton analysis discussed in Sect. 6.2.2. In the inclusive analysis we turned off photon radiation in PYTHIA, hence the Z peak visible in Fig. 6.3.a is well articulated at both sides. The rise in the beginning of all contributions in Fig. 6.3.a is coming from the decay of low-lying neutral mesons, for further discussion the reader is referred to Sect. 3.3. Looking at the invariant mass of all same-flavor same-sign (anti-)lepton pairs in all events, plotted in Fig. 6.3.b, an almost monotonically decreasing distribution is found. These lepton combinations can come from several possible sources: one from the (anti-)t-quark and the

other from the W or Z , a prompt and a secondary (anti-)leptons, two secondary (anti-)leptons.

The predictions using HERWIG as SMC, instead of PYTHIA, agree with the PYTHIA ones well below 5% in all the dilepton mass range considered (see the ratios plotted in both lower panels of Fig. 6.3).

In Fig. 6.4.a, the transverse momentum distribution of the hardest lepton of each event is shown. Here it is worth noting the different shapes of the $t\bar{t} + W^+$ and $t\bar{t} + W^-$ distributions, with the $t\bar{t} + W^-$ becoming larger than the $t\bar{t} + W^+$ one for $p_\perp > 260$ GeV, as expected because the high p_\perp tail is populated by prompt leptons emitted from primary $W^- \rightarrow \ell \nu_\ell$ decays, that are absent in case of W^+ decays. Leptons originated by primary Z decays can have even larger p_\perp as seen from the shape of the tail of the $t\bar{t} + Z$ distribution, with a slope flatter than previous ones.

Finally, the missing transverse momentum distribution due to all neutrinos is plotted in Fig. 6.4.b. The shape of the $t\bar{t} + W^+$ distribution is similar to the $t\bar{t} + W^-$ one, with a rescaling factor just due to the different cross-section, whereas the shape of the $t\bar{t} + Z$ distributions differs from the previous ones, with a larger contribution in the first two bins, due to events without neutrinos or with neutrinos from secondary decays with very small transverse energy and a flatter slope than the $t\bar{t} + W^\pm$ cases. The region around 50 GeV, where the $t\bar{t} + W^+$ and $t\bar{t} + Z$ distributions are closer together, is filled by neutrinos from prompt W^+ decays, absent in case of $t\bar{t} + Z$. The first bin is enhanced in all distributions due to the possibility of events without neutrinos (W decays in two light jets are indeed possible and not ruled out by any selection cut in this analysis).

For both distributions plotted in Fig. 6.4 we found that the differences between the cumulative predictions by PYTHIA and HERWIG, obtained by summing over the three $t\bar{t} + V$ processes, are within 5% (see the lower panels), with a slightly better agreement in case of the p_\perp -distribution.

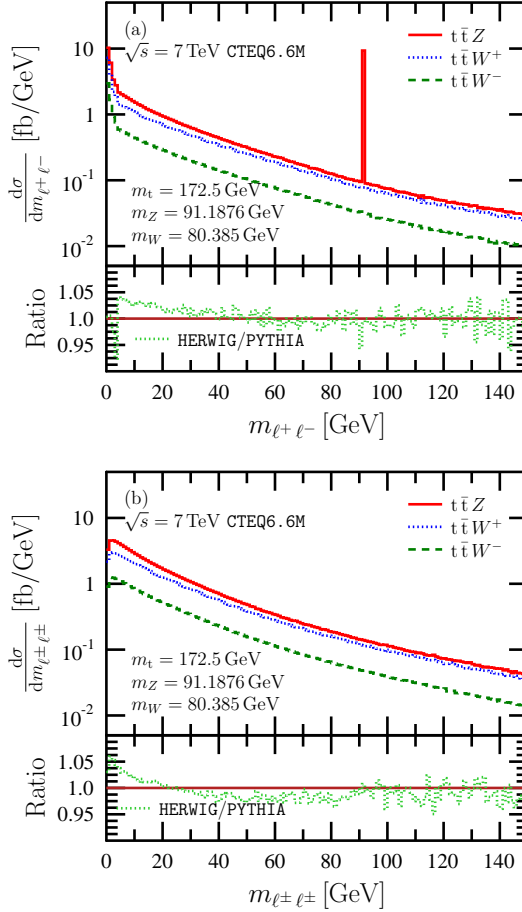


Figure 6.3: Invariant mass of a) all (ℓ^+, ℓ^-) same-flavor lepton-antilepton pairs and b) all (ℓ, ℓ) same-sign lepton and anti-lepton pairs from all events in the inclusive analysis, as obtained by PowHe1 + PYTHIA at the $\sqrt{s} = 7 \text{ TeV}$ LHC. Predictions for the three processes $t\bar{t} + Z$, $t\bar{t} + W^+$, and $t\bar{t} + W^-$ are shown separately. In the lower panel, the ratio between the cumulative predictions of PowHe1 + HERWIG and PowHe1 + PYTHIA is also shown.

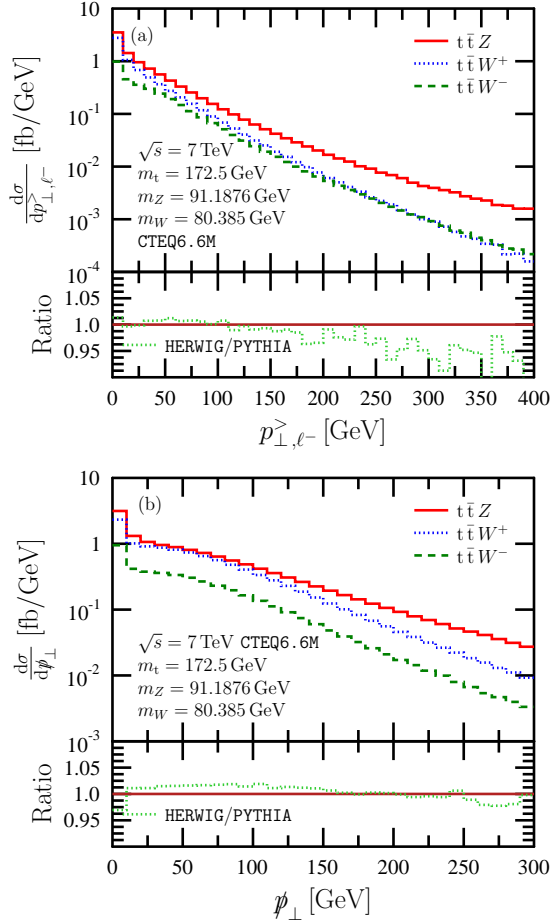


Figure 6.4: Distributions of a) the transverse momentum of the hardest lepton and b) the missing transverse momentum due to all neutrinos from all events in the no-cut analysis, as obtained by PowHe1 + PYTHIA at the $\sqrt{s} = 7$ TeV LHC. Predictions for the three processes $t\bar{t} + Z$, $t\bar{t} + W^+$, and $t\bar{t} + W^-$ are shown separately. In the lower panel, the ratio between the cumulative predictions of PowHe1 + HERWIG and PowHe1 + PYTHIA is also shown.

6.2.2 Trilepton-channel analysis

The aim of the trilepton channel analysis proposed in Ref. [128] is selecting $t\bar{t} + Z$ events, with Z decaying in two opposite-sign charged leptons, and one of the quarks of the $t\bar{t}$ -pair decaying leptonically, whereas the other one hadronically. In particular, we considered the following set of cuts:

1. at least two opposite-charge, same-flavor leptons with $p_{\perp,\ell} > 20$ GeV and within CMS acceptance ($|\eta_{\ell}| < 2.4$, with an additional cut on the electrons impinging on the barrel/endcap transition region of the electromagnetic calorimeter (ECAL), corresponding to the pseudorapidity interval $1.4442 < |\eta_{\ell}| < 1.566$),
2. constrain the invariant mass of the dilepton system (“reconstructed Z ”) within the $81 \text{ GeV}/c^2 < m_{\ell^+\ell^-} < 101 \text{ GeV}/c^2$ interval,
3. $p_{\perp,\ell^+\ell^-} > 35$ GeV, where $p_{\perp,\ell^+\ell^-}$ is the transverse momentum of the reconstructed Z ,
4. at least a third lepton in the event with $p_{\perp,\ell_3} > 10$ GeV and obeying the same pseudorapidity requirements as the other two leptons,
5. at least three jets with $p_{\perp,j} > 20$ GeV and $|\eta_j| < 2.4$, of which two positively b-tagged,
6. $H_T > 120$ GeV, defined as the scalar sum of the transverse momenta of all jets with $p_{\perp,j} > 20$ GeV and $|\eta_j| < 2.4$.

In our simulation, jets were reconstructed using the anti- k_{\perp} algorithm, with $R = 0.5$, using FASTJET [124]. b-tagging was done by means of the MCTRUTH parameter, allowing to trace back the origin of a jet to a b or a \bar{b} quark. In case of multiple dilepton pairs with opposite charge and same flavor satisfying cuts 1), 2) and 3), the pair with the invariant mass closest to the nominal Z mass was selected.

Predictions for the expected number of events after cuts at the $\sqrt{s} = 7$ TeV LHC, corresponding to an integrated luminosity $L = 4.98 \text{ fb}^{-1}$, as obtained by our PowHel+ PYTHIA simulations, are shown in Fig. 6.5, distinguishing the possible decay channels, labelled by the flavors of the two leptons entering the dilepton system plus the third lepton mentioned in cut 4). When more than one additional lepton satisfies cut 4), we choose that with the largest p_{\perp} . The sum of the

results in all channels is plotted in the last bin of the figure, as well. These predictions can be compared to the experimental results, presented in Ref. [128] for the same luminosity, with the caveat that we still do not include the predictions for background processes (like $Z + \text{jets}$, $t\bar{t}$ and diboson production) at the same accuracy. For an estimate of these background contributions at a lower accuracy, one can rely on Ref. [128]. One has also to take into account that the CMS Collaboration used an experimental b-jet tagging algorithm, instead of a purely theoretical one, as we did.

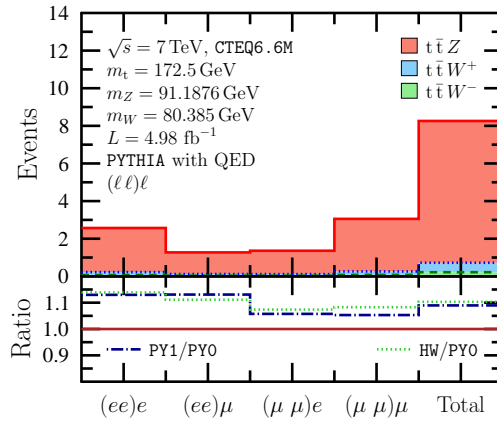


Figure 6.5: Number of events in the trilepton channels at the $\sqrt{s} = 7 \text{ TeV}$ LHC, as predicted by PowHel + PYTHIA, for an integrated luminosity amounting to $L = 4.98 \text{ fb}^{-1}$. The contribution in the $(e, e) e$, $(e, e) \mu$, $(\mu, \mu) e$ and $(\mu, \mu) \mu$ channels are shown separately, as well as their sum in the last bin. The contributions due to $t\bar{t} + Z$, $t\bar{t} + W^+$ and $t\bar{t} + W^-$ are cumulated one over the other. To be compared with the experimental data in Fig. 4 of the CMS technical report [128]. In the lower inset the ratios between cumulative results using different SMC (HERWIG/PYTHIA) and between cumulative results obtained by neglecting and including photon radiation off leptons (PYTHIA-no-brem/PYTHIA) are also shown.

As expected, as a result of the selection cuts, and in particular of the cut on the invariant mass of the dilepton system, both in the experiment and in our theoretical predictions the contributions to the total number of events due to the

$t\bar{t} + W^\pm$ processes are highly suppressed. We estimate a suppression factor of about 10 between the cross-sections after the cuts for the processes ($t\bar{t} + W^+ + t\bar{t} + W^-$) and $t\bar{t} + Z$, from our theoretical simulations. The invariant mass of the reconstructed Z is plotted for these three processes in Fig. 6.6.a, from where it is clear that the largest contribution of the $t\bar{t} + Z$ process is due to the peak around m_Z , completely absent in case of both $t\bar{t} + W^+$ and $t\bar{t} + W^-$.

In the lower inset of Fig. 6.6 the ratios of the results using different SMC's are plotted. In particular, using HERWIG instead of PYTHIA as SMC, leads to a larger number of events. This is due to the different physics implemented in the two SMC's. PYTHIA includes by default photon radiation off leptons, the stand-alone fortran version of HERWIG does not include it (unless one interfaces it with external packages). This photon radiation affects the dilepton invariant mass after SMC: as shown in Fig. 6.6.b, (that is the analogous of Fig. 6.3.a after cuts), the very narrow peak evident in case of HERWIG simulations is smeared by the default PYTHIA simulations (denoted by PY0). As a further check, we switched off this kind of emissions even in PYTHIA (denoted by PY1). The predictions of PYTHIA without photon radiation are superimposed on the same plot and look to be closer to the HERWIG ones. The modification on the number of events after cuts in the different channels, one gets by switching off this effect in PYTHIA, is also shown in the lower panel of Fig. 6.5.

The predictions presented in Fig. 6.5 are compatible with the experimental data of Ref. [128] within the error-bars of the latter. In our prediction a slight asymmetry can be seen comparing electron and muon final states. Our PYTHIA prediction contains QED radiation, which affects electron final states more, since electrons can radiate more photons compared to muons, due to the fact that the dead-cone of the muon is much larger than the one of the electron. The electrons in the final state are affected by one additional cut (see cut 1).

Our predictions for the cross-section contributions in the different tripleton channels (see Fig. 6.5), summing over the three processes $t\bar{t} + Z$, $t\bar{t} + W^+$ and $t\bar{t} + W^-$, in case of $\sqrt{s} = 7\text{ TeV}$ LHC, are as follows: $\sigma_{(e,e),e} = 0.516\text{ fb}$, $\sigma_{(e,e),\mu} = 0.255\text{ fb}$, $\sigma_{(\mu,\mu),e} = 0.273\text{ fb}$, $\sigma_{(\mu,\mu),\mu} = 0.613\text{ fb}$, $\sigma_\Sigma = 1.658\text{ fb}$, all with a statistical uncertainty below 10^{-5} fb .

The transverse momentum distributions of the leading and subleading (anti-)lepton of the (ℓ^+, ℓ^-) pairs selected by the considered system of cuts are shown separately in Fig. 6.7. These distributions have different shapes, as expected: those belonging to the leading lepton are peaked at $\sim 65\text{ GeV}$ for both $t\bar{t} + Z$, $t\bar{t} + W^+$ and $t\bar{t} + W^-$ while those belonging to the subleading lepton decrease

monotonically just above the $p_{\perp,\ell} > 20$ GeV cut. When considered together, the lepton and the anti-lepton give rise to a “reconstructed Z ”, whose p_\perp has a shape characterized by a smooth peak in the 50 GeV region. We also repeated the analysis in the trilepton channel in case of an LHC $\sqrt{s} = 8$ TeV center-of-mass energy, that can be useful in view of future data analysis on the basis of the events recorded in the present run. For future reference, we report here our cumulative predictions for the cross-section contributions of the three processes $t\bar{t} + Z$, $t\bar{t} + W^+$ and $t\bar{t} + W^-$ at $\sqrt{s} = 8$ TeV: $\sigma_{(e,e),e} = 0.782$ fb, $\sigma_{(e,e),\mu} = 0.388$ fb, $\sigma_{(\mu,\mu),e} = 0.420$ fb, $\sigma_{(\mu,\mu),\mu} = 0.934$ fb, $\sigma_\Sigma = 2.524$ fb, all with a statistical uncertainty below $5 \cdot 10^{-5}$ fb. Furthermore, predictions for the same differential distributions already discussed in the $\sqrt{s} = 7$ TeV case, were produced in the 8 TeV case, and we have found very similar results, except for a rescaling factor just given by the ratio of the cross-sections at 8 and 7 TeV. The LHE’s are freely available at our web repository: <http://www.grid.kfki.hu/twiki/bin/view/DbTheory/WebHome>.

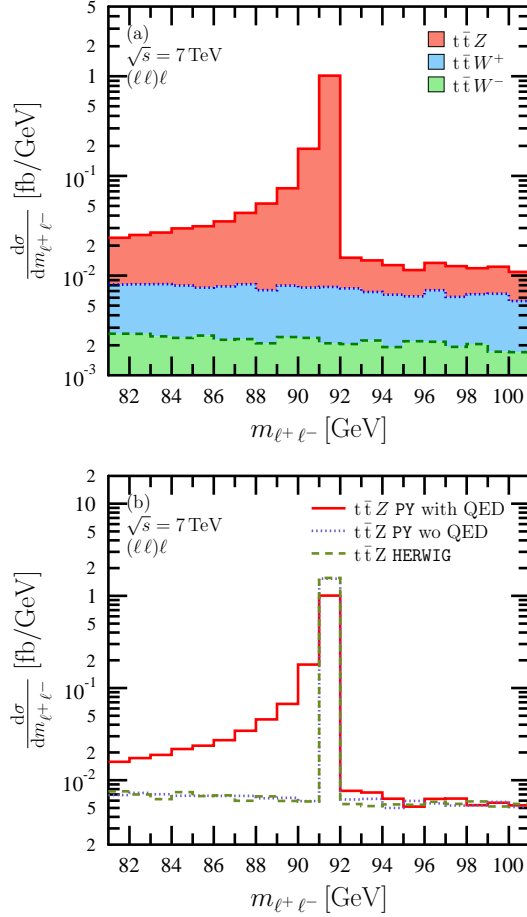


Figure 6.6: Invariant mass of the Z reconstructed from same-flavor (ℓ^+ , ℓ^-) pairs after the tripleton analysis, as obtained by PowHel1+ PYTHIA at the $\sqrt{s} = 7$ TeV LHC. a) Predictions corresponding to the different processes $t\bar{t} + Z$, $t\bar{t} + W^+$ and $t\bar{t} + W^-$ cumulated one over the other, b) distributions obtained by using different SMC (PYTHIA, HERWIG and PYTHIA without photon radiation off leptons) are also shown, limited to $t\bar{t} + Z$ -production.

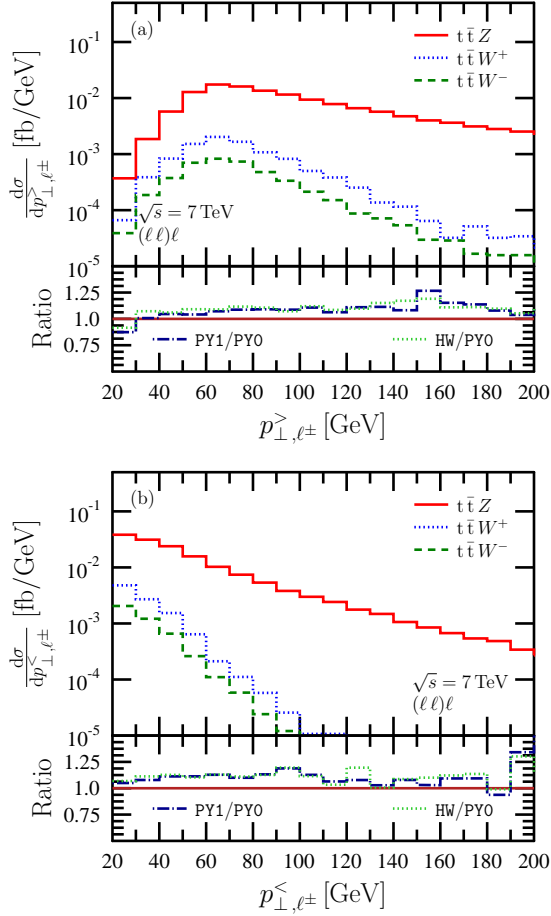


Figure 6.7: Transverse momentum distributions of a) the leading and b) the sub-leading (anti-)lepton of each (ℓ^+, ℓ^-) pair corresponding to a reconstructed Z boson. Predictions by PowHe1 + PYTHIA, corresponding to the different $t\bar{t} + Z$, $t\bar{t} + W^+$ and $t\bar{t} + W^-$ processes are shown separately. In the lower inset the ratios between cumulative results using different SMC HERWIG and PYTHIA (HW/PY0) and between cumulative results obtained by neglecting and including photon radiation off leptons in PYTHIA (PY1/PY0) are also shown.

6.2.3 Dilepton-channel analysis

As mentioned in the beginning of this chapter, studies of $t\bar{t} + V$ decays in the dilepton channel, with two same-sign leptons plus jets, have their original motivation that this kind of signature is hardly produced by SM processes, and can thus be used in searches for supersymmetry. In this case, $t\bar{t} + V$ can be considered as a background with respect to possible new physics processes. Other sizable backgrounds involve many different diboson and triboson production processes. An exhaustive list of backgrounds in this context can be found in Ref. [131]. New physics searches usually also involve a cut on missing energy. We explore the dilepton channel, without imposing any missing energy cut, as also done in the very recent CMS technical report [128], where the analysis was optimized on the basis of data collected at LHC at $\sqrt{s} = 7$ TeV corresponding to an integrated luminosity $L = 4.98 \text{ fb}^{-1}$. This way the relatively small number of $t\bar{t} + V$ events does not suffer any further suppression due to this cut.

The aim of this analysis is to select the events where one of the quarks of the $t\bar{t}$ -pair decays leptonically and the other one hadronically, and the vector boson decays leptonically giving rise to a lepton with the same sign of the lepton coming from the (anti-)quark. In case of $t\bar{t} + W^+$ -production this means that we are looking for $W^+ \rightarrow \ell^+ \nu_\ell$, accompanied by the leptonic decay of the t-quark, whereas, in case of $t\bar{t} + W^-$ -production we aim to select events with $W^- \rightarrow \ell^- \bar{\nu}_\ell$, accompanied by the leptonic decay of the \bar{t} -quark. In case of $t\bar{t} + Z$ -production $Z \rightarrow \ell^+ \ell^-$, and thus it is sufficient that either the t- or the \bar{t} -quark decays leptonically.

Following the CMS Collaboration, we considered the following set of cuts:

1. two same-sign isolated leptons with $p_{\perp, \ell_1} > 55$ GeV and $p_{\perp, \ell_2} > 30$ GeV, respectively, within CMS acceptance ($|\eta_\ell| < 2.4$, plus a further removal of the $[1.4442, 1.566]$ pseudorapidity range corresponding to the ECAL barrel/endcap transition region, applied in case of electrons),
2. dilepton invariant mass $m_{\ell_1, \ell_2} > 8$ GeV,
3. at least 3 jets with $p_{\perp, j} > 20$ GeV and $|\eta_j| < 2.4$, satisfying the additional cut $\Delta R(j, \ell) > 0.4$ on the distance in the pseudorapidity-azimuthal angle plane, for both $\ell = \ell_1, \ell_2$,
4. at least one of the previous 3 jets must be b-tagged,
5. $H_T > 100$ GeV, where H_T is computed as the scalar sum of the transverse momenta of all jets satisfying cut 3).

Jets were constructed using the anti- k_\perp algorithm, with $R = 0.5$, as implemented in FASTJET [124]. Lepton isolation was computed by making use of the standard isolation criterion mentioned in the CMS technical report [127]: we require a lepton relative isolation $I_{rel} > 0.15$, where I_{rel} is computed as the ratio between the scalar sum of the transverse momenta of all tracks within a distance $\Delta R < 0.3$ with respect to the selected lepton and the transverse momentum of the lepton itself (excluded from the sum at the numerator). Furthermore, in case of multiple dilepton pairs satisfying the cuts mentioned above, the pair was selected with the largest combined transverse momentum.

As also done in the CMS analysis [128], we explicitly exclude from this analysis all events that are selected in the trilepton channel analysis, in order to obtain two statistical independent samples (trilepton veto). As we will see in the following, the final predictions in the dilepton channel, for both the number of events and the shape of the distributions, will indeed be affected by this choice, especially as for the $t\bar{t} + Z$ process.

Differences between our theoretical analysis framework and the experimental conditions are listed in the following:

- Contrary to experimental reconstruction of the events, electron and muon detection efficiencies in our theoretical simulations were assumed to be 100 % and charge misidentification effects neglected.
- Also, while in the experiment b-jets were reconstructed as displaced vertices, making use of spatial tracking information, and a b-tagging algorithm was applied, ensuring a limited efficiency in the reconstruction of b-jets, accompanied by a non-negligible fake rate, in our simulations we identified b-jets using the MCTRUTH parameter which allows for tracking back b and \bar{b} quarks from $t\bar{t}$ -decay, but we lacked spatial information concerning the position of displaced vertices.

Despite the differences in the analysis, and perhaps other experimental detail we are not aware of, the theoretical predictions, shown in Fig. 6.8, are compatible with the experimental results.

The largest contribution to the total number of events is from the $t\bar{t} + W^+$ process, followed by the $t\bar{t} + Z$ and the $t\bar{t} + W^-$ ones. The contribution of the $t\bar{t} + W^+$ process is larger than the $t\bar{t} + W^-$ one already at the inclusive level (see Sect. 6.2.2), with the ratio between the two remaining almost the same after cuts (2.45 for the inclusive predictions and 2.42 after cuts). The contribution

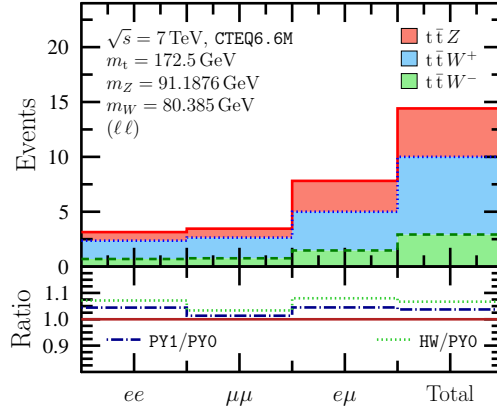


Figure 6.8: Number of events in the dilepton channel at $\sqrt{s} = 7 \text{ TeV}$ LHC, as predicted by PowHel + PYTHIA, for an integrated luminosity $L = 4.98 \text{ fb}^{-1}$. The contribution in the (e, e) , (μ, μ) , (e, μ) channels are shown separately, as well as their sum in the last bin. The contributions due to $t\bar{t} + Z$, $t\bar{t} + W^+$ and $t\bar{t} + W^-$ are cumulated one over the other. In the lower inset the ratios between cumulative results using different SMC HERWIG and PYTHIA (HW/PY0) and between cumulative results obtained by neglecting and including photon radiation off leptons in PYTHIA (PY1/PY0) are also shown.

of $t\bar{t} + W^+$ is enhanced with respect to that of $t\bar{t} + Z$ after cuts is an effect of the selection cuts and of the trilepton veto. For the $t\bar{t} + W^\pm$ processes, the contribution in the (e, μ) channel turns out to be almost twice the average of the (e, e) and (μ, μ) ones, as naively expected on the basis of the possible charge and flavor combinations. (An electron can come from the W and a muon with the same sign from one of the t-quarks, or vice versa.) For the $t\bar{t} + Z$ process, the contribution in the (e, μ) channel turns out to be $\simeq 3.5$ times the average of the (e, e) and (μ, μ) ones, i.e. larger than expected on the basis of the charge and flavor combinatorics. The reason has to be attributed to the trilepton veto. As seen in Fig. 6.5, the number of events in the trilepton channel in case of the (e, e) e and (μ, μ) μ combinations are larger than those in the (e, e) μ and (μ, μ) e bins. The former affects the (e, e) and (μ, μ) bins of the dilepton analysis, while

the latter affects the (e, μ) bins of the dilepton analysis. As a consequence, the contribution to the (e, μ) channel of the dilepton analysis is less suppressed than those in the (e, e) and (μ, μ) channels due to the trilepton veto. The predictions by different SMC programs, i.e. HERWIG and PYTHIA (PY1) are up to 8% and 5% larger than those of default PYTHIA (PY0), as seen from the lower panel of Fig. 6.8. These differences have the same sign, but are smaller, than those found in case of the trilepton analysis (see the lower panel of Fig. 6.5 for comparison).

The PowHel + PYTHIA predictions for the cross-section contributions in the different dilepton channels (see Fig. 6.8), summing over $t\bar{t} + Z$, $t\bar{t} + W^+$ and $t\bar{t} + W^-$, in case of $\sqrt{s} = 7$ TeV LHC are listed in the following, together with their sum: $\sigma_{(e,e)} = 0.631$ fb, $\sigma_{(e,\mu)} = 0.694$ fb, $\sigma_{(\mu,\mu)} = 1.569$ fb, $\sigma_\Sigma = 2.894$ fb, all with a statistical uncertainty below $3 \cdot 10^{-5}$ fb.

As for the comparison with the experimental data, we note that in the CMS technical report [128] a contribution to the number of events was assigned to the effect of charge misidentification for the leptons, in particular the electrons, and another additional contribution to the effect of non-prompt leptons, i.e. leptons not coming directly from heavy boson decays. In our theoretical simulations the background due to charge misidentification vanishes, whereas a possible contribution of non-prompt leptons to our final results relies on the effectiveness of the isolation criteria we adopted. In this respect, even if we lack a precise estimate, it can be interesting to observe the differential distributions of the hardest isolated (anti-)leptons of each event after cuts, plotted in Fig. 6.9.

We see from Fig. 6.9.a, in case of $t\bar{t} + W^+$ the hardest isolated anti-lepton after cuts has a minimum p_\perp of 50 GeV and a peak slightly above it, whereas in case of $t\bar{t} + W^-$ it has a minimum p_\perp of 30 GeV without a peak. In case of the hardest isolated lepton, instead, the behavior of $t\bar{t} + W^+$ and $t\bar{t} + W^-$ is the opposite, as can be seen in Fig. 6.9.b. This behaviour is compatible with cut 1) and means that the system of proposed cuts is effective in selecting prompt leptons, i.e. the selection of (ℓ^+, ℓ^+) pair in case of $t\bar{t} + W^-$ decay, or of (ℓ^-, ℓ^-) pair in the $t\bar{t} + W^+$ decay are actually suppressed by orders of magnitude, even if several leptons and anti-leptons can be present after PS, hadronization and hadron decays. In case of $t\bar{t} + Z$ decays, two opposite-charge leptons are produced by Z -decays, so both (ℓ^+, ℓ^+) and (ℓ^-, ℓ^-) pairs of prompt leptons could be selected. Thus a peak above 50 GeV is present in both the lepton and the anti-lepton distributions. In all cases, the peaks slightly above 50 GeV are related to the request of having at least one (anti-)lepton with $p_\perp > 55$ GeV in the selection cuts.

As examples of further distributions that can be measured in the experiment,

the cumulative transverse momentum distributions of the leading and subleading lepton or anti-lepton of the $(\ell, \bar{\ell})$ selected pairs are plotted in Fig. 6.10. At low p_{\perp} the sum is dominated by the $t\bar{t} + W^+$ contribution, whereas in the high p_{\perp} tail (i.e. above $\simeq 300$ GeV in case of the leading lepton and above $\simeq 150$ GeV in case of the subleading one), the contributions of $t\bar{t} + Z$ and $t\bar{t} + W^+$ become almost equal.

In view of the searches for new physics in the dilepton channel another interesting distribution is that of the missing transverse energy, plotted in Fig. 6.11. In Fig. 6.11.a, different shapes characterize the three $t\bar{t} + V$ processes. The distribution for $t\bar{t} + Z$ is peaked around 30 GeV, while that for $t\bar{t} + W^{\pm}$ is peaked around 50 GeV. This difference is related to the $W \rightarrow \ell \nu_{\ell}$ decay events selected in the dilepton analysis, that populate the peak region. The suppression in the first few bins, not present in the analogous inclusive p_{\perp} -distribution plotted in Fig. 6.4.b, is an effect of the set of cuts, aiming at the selection of two same-sign prompt (anti-)leptons. With this selection both the primary boson and either the t - or the \bar{t} -quark should decay leptonically, leading to a non-zero p_{\perp} . As expected, including further cuts on p_{\perp} , will enhance the relative contribution of the $t\bar{t} + W^{\pm}$ process with respect to the $t\bar{t} + Z$ one, and will reduce the number of observed $t\bar{t} + V$ events. In particular, integrating over the cumulative p_{\perp} -distribution, plotted in Fig. 6.11.b, we find that a cut of $p_{\perp} > 50$ GeV corresponds to a reduction on the total number of events, plotted in Fig. 6.8, by a factor of $\simeq 4$ and a cut of $p_{\perp} > 100$ GeV to a further reduction by a similar factor.

Looking forward to an analysis of data collected in the recent LHC energy upgrade, we repeated the whole analysis at $\sqrt{s} = 8$ TeV LHC. For future reference, we list our predictions for the cross-sections after cuts at this energy for each dilepton channel, together with their sum. We found $\sigma_{(e,e)} = 0.907$ fb, $\sigma_{(e,\mu)} = 0.991$ fb, $\sigma_{(\mu,\mu)} = 2.289$ fb, $\sigma_{\Sigma} = 4.187$ fb, all with a statistical uncertainty $< 5 \cdot 10^{-5}$. As for differential distributions at 8 TeV, we found that their general qualitative behaviour and their shapes are similar to those already shown at 7 TeV, thus we do not present them again here. These can just be obtained by a proper rescaling factor given by the ratio of the cross-sections at 8 and 7 TeV. The LHE's are freely available at our web repository.

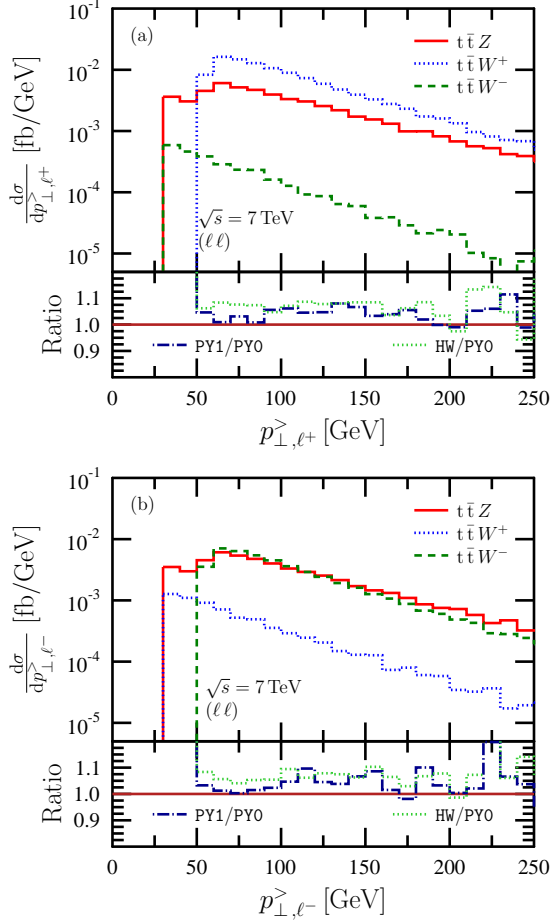


Figure 6.9: Transverse momentum distributions of a) the hardest anti-lepton and b) the hardest lepton of each event at $\sqrt{s} = 7 \text{ TeV}$ LHC, as predicted by PowHel + PYTHIA after the dilepton analysis. The distributions for $t\bar{t} + Z$, $t\bar{t} + W^+$ and $t\bar{t} + W^-$ are shown by solid (red), dotted (blue) and dashed (green) lines, respectively. In the lower inset the ratios between cumulative results using different SMC HERWIG and PYTHIA (HW/PY0) and between cumulative results obtained by neglecting and including photon radiation off leptons in PYTHIA (PY1/PY0) are also shown.

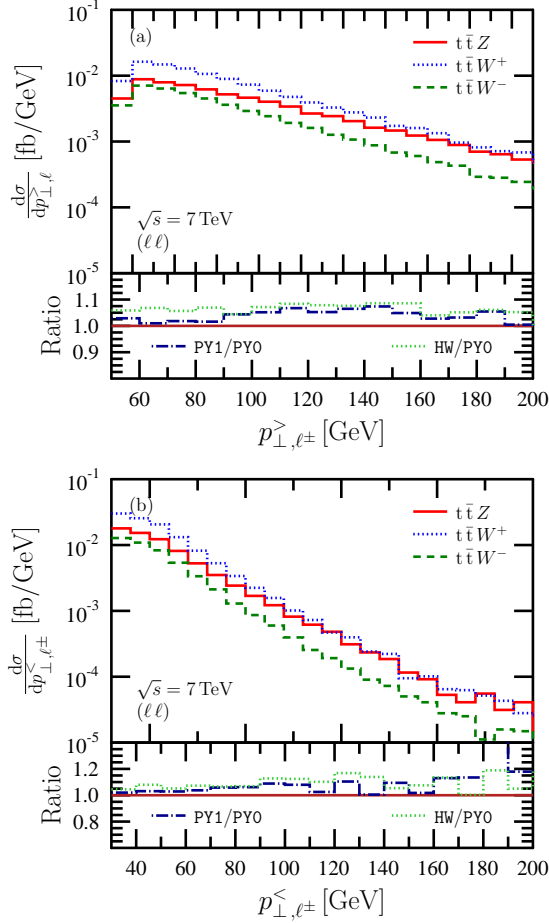


Figure 6.10: Transverse momentum distribution of a) the leading and b) the sub-leading (anti)-lepton of each same-sign (ℓ, ℓ) pair after the dilepton analysis. Predictions by PowHe1 + PYTHIA at $\sqrt{s} = 7$ TeV LHC corresponding to the different $t\bar{t} + Z$, $t\bar{t} + W^+$ and $t\bar{t} + W^-$ processes are shown separately. In the lower inset the ratios between cumulative results using different SMC HERWIG and PYTHIA (HW/PY0) and between cumulative results obtained by neglecting and including photon radiation off leptons in PYTHIA (PY1/PY0) are also shown.

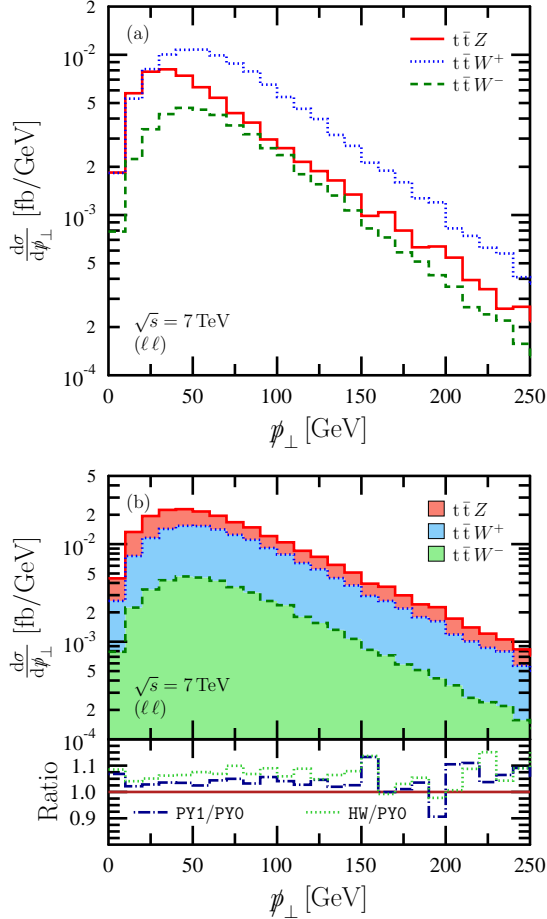


Figure 6.11: Missing transverse momentum distribution at $\sqrt{s} = 7$ TeV LHC, as predicted by PowHel1 + PYTHIA after the dilepton analysis. a) distributions for the processes $t\bar{t} + Z$ (red), $t\bar{t} + W^+$ (dotted) and $t\bar{t} + W^-$ (dashed) (red, dotted (blue) and slashed (green) lines. b) these different contributions are added one over the other in a cumulative way. In the lower inset the ratios between cumulative results using different SMC HERWIG and PYTHIA (HW/PY0) and between cumulative results obtained by neglecting and including photon radiation off leptons in PYTHIA (PY1/PY0) are also shown.

Chapter 7

Summary and outlook

The top quark has an important role in QCD, in Standard Model and in BSM physics. Thus predictions for top quark related processes at high precision are highly welcomed. Nowadays high precision means predictions beyond NLO accuracy. In this thesis I summarized my work on matching NLO QCD calculations with parton shower programs for processes with a top pair and one hard object in the final state.

I used the POWHEG method to match NLO QCD calculations with parton showers, as implemented in the POWHEG-BOX. I created a universal interface between the POWHEG-BOX and the HELAC-NLO programs, we called this framework PowHel. With the help of this I implemented five associated top quark pair hadroproduction processes in the POWHEG-BOX program. One important benefit of this program is the generation of unweighted events in standard Les Houches format, or in short Les Houches events (LHE's). Although these events are used as input to the parton shower programs, these can also be used to make comparisons at various stages of event evolution. The implementation and the accuracy can be checked comparing the predictions from LHE's against the NLO distributions. Decay can be performed on the heavy particles without showering or hadronization, hence the effect of decay can be analyzed too. By adding parton shower with hadronization we can clearly quantify the effect of those. The LHE's can also be used to reproduce my analysis or to implement a new one.

In my studies I analyzed the effect of the parton shower and hadronization for several processes. In all cases I found a softening in the H_{\perp} -distributions which was accompanied by a minute distortion in a few occasions. This softening

can be understood by the emission of soft particles which decrease the energy of the jets, if the emitted particles are outside of the jet-cone. I pointed out also that peaks are smeared due to the softening of jets. One important point of matching to parton showers is the possibility of making predictions for leptons since tops can be decayed by the parton shower program. I showed that the parton shower influences the lepton rapidity distributions negligibly, while the lepton p_{\perp} -distribution is only affected at low- p_{\perp} . In the low- p_{\perp} range the lepton transverse momentum is changed due to lepton-pairs of low transverse momentum created in the electromagnetic decay of low-lying neutral mesons and in photon conversion.

The POWHEG-BOX framework can be used for NLO calculations as well. By a fully detailed NLO analysis of $t\bar{t} + Z$ production I showed the importance of making NLO predictions by calculating differential K-factors for various distributions. In all cases the differential K-factors turned out to be non-uniform and in general sizable, hence making NLO predictions inevitable.

I demonstrated the usefulness of *event generation* by performing an analysis first done by the CMS collaboration in $t\bar{t} + V$ ($V = W^{\pm}, Z$) production and finding agreement with the experimental results.

This work, though extensive, cannot be considered complete. I only considered several, but not all three particle final states with a top quark-pair involved. There are several processes with four particles in the final state, a top pair and two additional particles, for which predictions would be desirable at higher precision than available in the literature. Among these we can find $t\bar{t} + b\bar{b}$ production which provides a non-negligible background to $t\bar{t} + H$ production, thus the investigation of both the signal and background can be fruitful to define an analysis which efficiently suppresses the background. The implementation of these processes could be useful, since they would allow a much more precise determination of background.

When NLO corrections are added the scale uncertainties are reduced, but not vanished from the calculation. For each process several possible scale definitions can be defined, these can result in different dependence upon the scales. The analysis of scale choices may shed light on particular definitions which minimize the dependence, hence result in more precise results.

To obtain my predictions I used the SMC programs to perform the decay of heavy particles. This approach works well when spin correlations can be neglected, because it is not included in the SMC program. As a possible extension I would like to include spin correlated decays into these processes and analyze the effect of these correlations on various distributions.

Chapter 8

Magyar nyelvű összefoglaló

A kvantum-színdinamika (QCD) az erős kölcsönhatás kvantum térelméleti modellje. Az elmélet anyagterei az $SU(N_c)$ csoport lokális transzformációival szembeni invarianciájuk folytán egy nem-Ábeli mértéktérrel hatnak kölcsön. A renormálási csoport egyenlet szerint az elmélet aszimptotikusan szabad, azaz megfelelően nagy energián az anyagtér (kvarktér) nem kölcsönható, ami lehetővé teszi a perturbációszámítás alkalmazhatóságát megfelelően nagy energián. Habár az aszimptotikus szabadság lehetővé teszi a perturbációs megközelítést, a számolás bonyolultsága gyorsan nő. Magasabb rendű korrekciók kiszámítása azonban elkerülhetetlen, hiszen a perturbatív sorfejtés csonkolása nem-fizikai paraméterek megjelenéséhez vezet az elméletben, az ezektől való függés pedig csak egyre több és több tag figyelembevételével csökkenthető.

A természetben eddig még nem figyeltek meg szabad kvarkokat, csak kötött állapotokat, a hadronokat. Ezek szerint a kvarkok nem pusztán aszimptotikus szabadságot, de alacsony energián bezárást is mutatnak. Míg nagy energián lehetséges a kvarkok és gluonok (összefoglaló néven partonok) szintjén a perturbatív számolás, addig a bezárás precíz elméleti leírása még várat magára, leírására pusztán *modellek* állnak rendelkezésre. A nagyenergiájú szórás kísérletekben nem hadronok, hanem azok kollimált pászmaí, jetjei, figyelhetőek meg, amelyek kialakulása a QCD sugárzással magyarázható. A kezdetben jelenlevő partonok színtöltésüknél fogva további partonokat emittálnak, ami egészen addig folyik, míg minden parton energiája megfelelően alacsony nem lesz, ahol a hadronizáció megtörténik.

A perturbációszámítás valamelyik rögzített rendjében a jeteket partonokkal

közelítjük, de ezek számban meg sem közelítik a kísérletekben a jetek belsejében észlelt hadronokét. A perturbációs számítás legalacsonyabb rendjében ugyanis egy jetnek pontosan egy parton felel meg. A perturbációs sorban minden további tag bevétele pusztán eggyel növeli meg a jeteket alkotó partonok számát. Továbbá a jetek leírása partonokkal történik, míg a detektor hadronokat érzékel. Egy elméleti számolásban jóslat pusztán ún. infravörös véges mennyiségekre tehető, tehát olyanokra, melyek invariánsak, ha a végállapotban további lágy és/vagy kollineáris részecskék jelennek meg. Mindazonáltal még ezek a mennyiségek is kaphatnak korrekciókat az általános QCD sugárzástól, vagy akár a hadronizációtól. Noha nem várunk nagy járulékokat ezektől az effektusoktól, a nagy pontosságú megfigyelések nagy pontosságú jóslatokat igényelnek, melyekhez ezen járulékok figyelembevétele elkerülhetetlen.

A QCD elméletében hat különböző kvark típus (zamat) létezik. A számolások során pusztán a legnehezebb, a top kvark, van tömegesként kezelve. A top nem pusztán a kvarkok, de az összes eddig észlelt elemi részecske közül a legnehezebb. Tömege megközelíti egy aranyatom tömegét. Köszönhetően nagy tömegének bomlása hamarabb megtörténik, minthogy hadronizálódni tudna. A Standard Modellbeli domináns bomlása a b kvarkba történik, ez elősegíti detektálását. A top kvark-pár keletkezés hatáskeresztmetszete elegendően nagy a várható LHC energiákon, ahhoz, hogy a top-pár és top-párhoz köthető további folyamatok nem elhanyagolható háttérrel és izgalmas lehetséges jelcsatornákat jelentenek. Így a kísérleti eredmények kiértékeléséhez pontos elméleti jóslatok szükségesek.

A top kvark nem pusztán a QCD-ben tölt be fontos szerepet, de az elemi részek Standard Modelljében is, hiszen csatolásainál fogva alkalmas a Standard Modell ellenőrzésére is. A top lehetséges egzotikus bomlási csatornáit pedig lehetőséget adhatnak a jövőben a Standard Modellen túli fizika megfigyelésére is. Számtalan modell számol ugyanis a top különböző egzotikus bomlásaival, továbbá top kvark párok keletkezésével egzotikus közvetítő részecskék által.

Az előbb elmondottakból kiviláglik, hogy a top kvark lényeges szerepet tölt be nem pusztán a QCD-ben, de a Standard Modellben és az azon túli fizikában is. Így aztán elengedhetetlen, hogy nagy pontosságú jóslatok álljanak a kísérletek rendelkezésére az adatok megbízható kiértékelése végett. Mainapság nagy pontosságú jóslat NLO-n (Next-to-Leading-Order, első sugárzási korrekciók figyelembevétele) túli pontosságot jelent. Dolgozatomban összefoglaltam munkámat, amelyet az NLO QCD számolások és a parton zápor programok egymással való egyesítése céljából végeztem. Olyan folyamatokat vizsgáltam melyek végállapotában egy top kvark pár mellett egy további nehéz részecske volt megtalálható.

Munkám során a POWHEG eljárást használtam fel NLO QCD számolások és a parton záporok illesztéséhez, ehhez a POWHEG-BOX nevű programot használtam fel, mely eme eljárás numerikus implementációja. Egy univerzális interfészt hoztam létre a POWHEG-BOX és a HELAC-NLO programok között, melynek a PowHel nevet adtuk. Az interfész felhasználásával öt top kvark párhoz köthető hadroprodukciónak implementáltam a POWHEG-BOX programban. Az egyik legnagyobb előnye ennek a programnak a súly nélküli események generálásában rejlik, melyeket a Les Houches standard szerint tárol el. Ezek a Les Houches Események (LHE) szolgálnak bemenet gyanánt a parton zápor programokhoz, viszont emellett változatos összehasonlításokra adnak lehetőséget az eseménygenerálás különböző fázisaiban. Az implementáció és annak pontossága is leellenőrizhető az NLO és a LHE-kből származó eloszlások összehasonlítása által. A nehéz részecskék elbomlasztathatóak a parton zápor és a hadronizáció figyelembevétele nélkül is, így lehetőség nyílik a bomlás hatásainak vizsgálatára. A parton zápor és hadronizáció bevétele pedig lehetővé teszi ezen hatások kvantitatív számolását. A LHE-ek eltárolhatóak és újra felhasználhatóak az analízis megismétlésére, vagy pedig egy új analízis elvégzésére is akár.

Vizsgálódásaimban tanulmányoztam a parton zápor és a hadronizáció hatását több folyamatnál. Minden esetben a H_{\perp} -eloszlások lágyulását találtam, ami néhány esetben együtt járt az eloszlás torzulásával is. A lágyulás a végállapotban megjelenő lágy részecskék következménye, melyek csökkentik a jetek energiáját, amennyiben kibocsátásuk a jeten kívülre történik. Továbbá rámutattam, hogy az esetleges rezonanciacsúcsok, köszönhetően a jetek lágyulásának, kiszélesednek. Lényeges előnye a parton zápor programokhoz való illesztésnek, hogy jóslatok tehetőek leptonokra, mivel a parton zápor program segítségével a top kvarkok elbomlasztathatóak. Megmutattam, hogy a parton zápor elhanyagolható mértékben változtatja meg a lepton rapiditás eloszlásokat, addig a lepton transzverz impulzus eloszlások esetében pedig csak az alacsony- p_{\perp} tartományában történik változás. Az alacsony- p_{\perp} tartományában megjelenő többletet kis p_{\perp} -jú lepton-párok okozzák, melyek kis tömegű semleges mezonok elektromágneses bomlásából, továbbá fotonkonverzióból származnak.

A POWHEG-BOX rendszer felhasználható NLO számítások végzésére is. A $t\bar{t} + Z$ keletkezés minden részletre kiterjedő NLO vizsgálata során megmutattam az NLO számolás fontosságát számos eloszlás differenciális K-faktorának kiszámítása segítségével, melyek nagyok és nem-állandónak adódtak, sugallva az NLO számolások elkerülhetetlenségét.

Megmutattam az *eseménygenerálás* hasznosságát egy olyan analízisen, melyet

a CMS kollaboráció végzett el elsőnek $t\bar{t} + V$ ($V = W^\pm, Z$) keletkezésén. A kapott jóslataim megegyeztek a kísérleti eredményekkel.

Ez a munka, noha terjedelmes, korántsem tekinthető teljesnek. Pusztán néhány olyan folyamatot vizsgáltam a sok közül, melynek végállapotában egy top kvark pár is megjelenik. Számos olyan folyamat ismeretes, ahol a végállapotban négy részecske, egy top pár és két további részecske, keletkezik, amelyekhez nagyobb pontosságú jóslatok szükségesek, mint amilyenek a szakirodalomban fellelhetők. Ezek között találjuk a $t\bar{t} + b\bar{b}$ keletkezést is, mely nem elhanyagolható háttérrel jelent a $t\bar{t} + H$ keletkezéshez, tehát felmerül az igény egy olyan analízisre, mely hatékonyan nyomja el ezt a háttérrel. Ezen folyamatok implementálása elősegítené a hátterek pontosabb meghatározását.

Az NLO korrekciók figyelembevétele csökkenti, de nem tünteti el a nem-fizikai skáláktól való függést. Minden folyamathoz számtalan skálaválasztással lehet élni, amelyek tanulmányozása fényt vethet olyan optimális skálákra, melyek minimalizálhatják a fennmaradó skála bizonytalanságot, ezáltal hozzájárulhatnak pontosabb eredményekhez.

Jóslataim megtételéhez a parton zápor programokat használtam a nehéz töltött részecskék bomlásához. Ez a megközelítés csak akkor helytálló, ha a spin-korrelációk elhanyagolhatóak, mivel ezek nincsenek jelen a parton zápor által elvégzett bomlásokban. Egy lehetséges továbblépésként szeretném figyelembe venni a spin korrelációkat, hogy azok hatásait is tanulmányozhassam különféle eloszlásokon.

Bibliography

- [1] O. Greenberg, *QUARKS: RESOURCE LETTER Q-1*, *Am.J.Phys.* **50** (1982) 1074–1089.
- [2] O. Greenberg, *Spin and Unitary Spin Independence in a Paraquark Model of Baryons and Mesons*, *Phys.Rev.Lett.* **13** (1964) 598–602.
- [3] D. Lichtenberg, *Unitary Symmetry and Elementary Particles*, .
- [4] J. C. Collins, D. E. Soper, and G. F. Sterman, *Factorization of Hard Processes in QCD*, *Adv.Ser.Direct.High Energy Phys.* **5** (1988) 1–91, [[hep-ph/0409313](#)].
- [5] Y. I. Azimov, Y. L. Dokshitzer, V. A. Khoze, and S. Troyan, *Similarity of Parton and Hadron Spectra in QCD Jets*, *Z.Phys.* **C27** (1985) 65–72.
- [6] Y. I. Azimov, Y. L. Dokshitzer, V. A. Khoze, and S. Troian, *The String Effect and QCD Coherence*, *Phys.Lett.* **B165** (1985) 147–150.
- [7] S. Catani, F. Krauss, R. Kuhn, and B. Webber, *QCD matrix elements + parton showers*, *JHEP* **0111** (2001) 063, [[hep-ph/0109231](#)].
- [8] A. Buckley, J. Butterworth, S. Gieseke, D. Grellscheid, S. Hoche, *et. al.*, *General-purpose event generators for LHC physics*, *Phys.Rept.* **504** (2011) 145–233, [[arXiv:1101.2599](#)].
- [9] R. K. Ellis, W. J. Stirling, and B. R. Webber, *QCD and collider physics*, *Camb. Monogr. Part. Phys. Nucl. Phys. Cosmol.* **8** (1996) 1–435.
- [10] R. Feynman, *Photon-hadron interactions*, *Westview Press* (1973).

- [11] R. Field and R. Feynman, *Quark Elastic Scattering as a Source of High Transverse Momentum Mesons*, *Phys.Rev.* **D15** (1977) 2590–2616.
- [12] X. Artru and G. Mennessier, *String model and multiproduction*, *Nucl.Phys.* **B70** (1974) 93–115.
- [13] M. Bowler, *$e^+ e^-$ Production of Heavy Quarks in the String Model*, *Z.Phys.* **C11** (1981) 169.
- [14] B. Andersson, G. Gustafson, and B. Soderberg, *A General Model for Jet Fragmentation*, *Z.Phys.* **C20** (1983) 317.
- [15] B. Andersson, G. Gustafson, and B. Soderberg, *A PROBABILITY MEASURE ON PARTON AND STRING STATES*, *Nucl.Phys.* **B264** (1986) 29.
- [16] B. Webber, *A QCD Model for Jet Fragmentation Including Soft Gluon Interference*, *Nucl.Phys.* **B238** (1984) 492.
- [17] **Particle Data Group** Collaboration, J. Beringer *et. al.*, *Review of Particle Physics (RPP)*, *Phys.Rev.* **D86** (2012) 010001.
- [18] **CDF Collaboration** Collaboration, F. Abe *et. al.*, *Observation of top quark production in $\bar{p}p$ collisions*, *Phys.Rev.Lett.* **74** (1995) 2626–2631, [[hep-ex/9503002](#)].
- [19] **D0 Collaboration** Collaboration, S. Abachi *et. al.*, *Search for high mass top quark production in $p\bar{p}$ collisions at $\sqrt{s} = 1.8$ TeV*, *Phys.Rev.Lett.* **74** (1995) 2422–2426, [[hep-ex/9411001](#)].
- [20] J. R. Ellis and G. L. Fogli, *The Mass of the Top Quark from Electroweak Radiative Corrections*, *Phys.Lett.* **B213** (1988) 526.
- [21] J. R. Ellis and G. L. Fogli, *New bounds on $m(t)$ and first bounds on $M(H)$ from precision electroweak data*, *Phys.Lett.* **B249** (1990) 543–550.
- [22] A. Bilal, J. R. Ellis, and G. L. Fogli, *Could stops lighten the top?*, *Phys.Lett.* **B246** (1990) 459–465.
- [23] **OPAL Collaboration** Collaboration, G. Abbiendi *et. al.*, *Precise determination of the Z resonance parameters at LEP: 'Zedometry'*, *Eur.Phys.J.* **C19** (2001) 587–651, [[hep-ex/0012018](#)].

-
- [24] **Tevatron Electroweak Working Group, for the CDF and D0 Collaborations** Collaboration, *Combination of CDF and D0 results on the mass of the top quark using up to 5.8 fb⁻¹ of data*, arXiv:1107.5255. 16 pages, 2 figures.
- [25] **ATLAS Collaboration** Collaboration, G. Aad *et. al.*, *Observation of a new particle in the search for the Standard Model Higgs boson with the ATLAS detector at the LHC*, arXiv:1207.7214.
- [26] **CMS Collaboration** Collaboration, S. Chatrchyan *et. al.*, *Observation of a new boson at a mass of 125 GeV with the CMS experiment at the LHC*, *Phys.Lett.B* (2012) [arXiv:1207.7235].
- [27] S. Dimopoulos and G. Giudice, *Naturalness constraints in supersymmetric theories with nonuniversal soft terms*, *Phys.Lett.* **B357** (1995) 573–578, [hep-ph/9507282].
- [28] R. Barbieri, G. Dvali, and L. J. Hall, *Predictions from a U(2) flavor symmetry in supersymmetric theories*, *Phys.Lett.* **B377** (1996) 76–82, [hep-ph/9512388].
- [29] A. G. Cohen, D. Kaplan, and A. Nelson, *The More minimal supersymmetric standard model*, *Phys.Lett.* **B388** (1996) 588–598, [hep-ph/9607394].
- [30] S. Bar-Shalom and A. Rajaraman, *Models and phenomenology of maximal flavor violation*, *Phys.Rev.* **D77** (2008) 095011, [arXiv:0711.3193].
- [31] S. Bar-Shalom, A. Rajaraman, D. Whiteson, and F. Yu, *Collider Signals of Maximal Flavor Violation: Same-Sign Leptons from Same-Sign Tops at the Tevatron*, *Phys.Rev.* **D78** (2008) 033003, [arXiv:0803.3795].
- [32] M. Papucci, J. T. Ruderman, and A. Weiler, *Natural SUSY Endures*, arXiv:1110.6926. 55 pages, 21 figures.
- [33] E. L. Berger, Q.-H. Cao, C.-R. Chen, C. S. Li, and H. Zhang, *Top Quark Forward-Backward Asymmetry and Same-Sign Top Quark Pairs*, *Phys.Rev.Lett.* **106** (2011) 201801, [arXiv:1101.5625].
- [34] M. R. Buckley, D. Hooper, J. Kopp, and E. Neil, *Light Z' Bosons at the Tevatron*, *Phys.Rev.* **D83** (2011) 115013, [arXiv:1103.6035].

- [35] C. Csaki, L. Randall, and J. Terning, *Light Stops from Seiberg Duality*, arXiv:1201.1293.
- [36] **D0 Collaboration** Collaboration, V. M. Abazov *et. al.*, *Determination of the width of the top quark*, *Phys.Rev.Lett.* **106** (2011) 022001, [arXiv:1009.5686].
- [37] M. Jezabek and J. H. Kuhn, *QCD Corrections to Semileptonic Decays of Heavy Quarks*, *Nucl.Phys.* **B314** (1989) 1.
- [38] M. Jezabek and J. H. Kuhn, *The Top width: Theoretical update*, *Phys.Rev.* **D48** (1993) 1910–1913, [hep-ph/9302295].
- [39] K. Chetyrkin, R. Harlander, T. Seidensticker, and M. Steinhauser, *Second order QCD corrections to $\Gamma(t \rightarrow j W b)$* , *Phys.Rev.* **D60** (1999) 114015, [hep-ph/9906273].
- [40] J. M. Campbell and R. K. Ellis, *Top-quark processes at NLO in production and decay*, arXiv:1204.1513.
- [41] A. Denner, S. Dittmaier, S. Kallweit, and S. Pozzorini, *NLO QCD corrections to off-shell top-antitop production with leptonic decays at hadron colliders*, arXiv:1207.5018.
- [42] J. H. Kuhn and G. Rodrigo, *Charge asymmetry in hadroproduction of heavy quarks*, *Phys.Rev.Lett.* **81** (1998) 49–52, [hep-ph/9802268].
- [43] **CDF Collaboration** Collaboration, T. Aaltonen *et. al.*, *Evidence for a Mass Dependent Forward-Backward Asymmetry in Top Quark Pair Production*, *Phys.Rev.* **D83** (2011) 112003, [arXiv:1101.0034].
- [44] P. Ferrario and G. Rodrigo, *Massive color-octet bosons and the charge asymmetries of top quarks at hadron colliders*, *Phys.Rev.* **D78** (2008) 094018, [arXiv:0809.3354].
- [45] G. Rodrigo and P. Ferrario, *Charge asymmetry: A Theory appraisal*, *Nuovo Cim.* **C033N4** (2010) 221–228, [arXiv:1007.4328].
- [46] D. Gross and F. Wilczek, *Ultraviolet Behavior of Nonabelian Gauge Theories*, *Phys.Rev.Lett.* **30** (1973) 1343–1346.

-
- [47] H. D. Politzer, *Reliable Perturbative Results for Strong Interactions?*, *Phys.Rev.Lett.* **30** (1973) 1346–1349.
- [48] M. L. Mangano and S. J. Parke, *Multiparton amplitudes in gauge theories*, *Phys.Rept.* **200** (1991) 301–367, [hep-th/0509223].
- [49] L. J. Dixon, *Calculating scattering amplitudes efficiently*, hep-ph/9601359.
- [50] D. Maitre and P. Mastrolia, *S@M, a Mathematica Implementation of the Spinor-Helicity Formalism*, *Comput.Phys.Commun.* **179** (2008) 501–574, [arXiv:0710.5559].
- [51] Z. Kunszt, *From scattering amplitudes to cross-sections in QCD*, hep-ph/9603235.
- [52] Z. Nagy and D. E. Soper, *General subtraction method for numerical calculation of one loop QCD matrix elements*, *JHEP* **0309** (2003) 055, [hep-ph/0308127].
- [53] S. Becker, C. Reuschle, and S. Weinzierl, *Numerical NLO QCD calculations*, *JHEP* **1012** (2010) 013, [arXiv:1010.4187].
- [54] S. Becker, C. Reuschle, and S. Weinzierl, *Efficiency improvements for the numerical computation of NLO corrections*, *JHEP* **1207** (2012) 090, [arXiv:1205.2096].
- [55] Z. Kunszt and D. E. Soper, *Calculation of jet cross-sections in hadron collisions at order α_s^3* , *Phys.Rev.* **D46** (1992) 192–221.
- [56] S. Frixione, Z. Kunszt, and A. Signer, *Three jet cross-sections to next-to-leading order*, *Nucl. Phys.* **B467** (1996) 399–442, [hep-ph/9512328].
- [57] S. Frixione, *A General approach to jet cross-sections in QCD*, *Nucl. Phys.* **B507** (1997) 295–314, [hep-ph/9706545].
- [58] S. Frixione, E. Laenen, P. Motylinski, and B. R. Webber, *Single-top production in MC@NLO*, *JHEP* **03** (2006) 092, [hep-ph/0512250].
- [59] S. Catani and M. H. Seymour, *A general algorithm for calculating jet cross sections in NLO QCD*, *Nucl. Phys.* **B485** (1997) 291–419, [hep-ph/9605323]. [Erratum-ibid.B510:503-504,1998].

- [60] S. Catani, S. Dittmaier, M. H. Seymour, and Z. Trocsanyi, *The dipole formalism for next-to-leading order QCD calculations with massive partons*, *Nucl. Phys.* **B627** (2002) 189–265, [[hep-ph/0201036](#)].
- [61] G. Somogyi and Z. Trocsanyi, *A new subtraction scheme for computing QCD jet cross sections at next-to-leading order accuracy*, [hep-ph/0609041](#).
- [62] A. Daleo, T. Gehrmann, and D. Maitre, *Antenna subtraction with hadronic initial states*, *JHEP* **04** (2007) 016, [[hep-ph/0612257](#)].
- [63] A. Gehrmann-De Ridder and M. Ritzmann, *NLO Antenna Subtraction with Massive Fermions*, *JHEP* **07** (2009) 041, [[arXiv:0904.3297](#)].
- [64] S. Frixione, P. Nason, and C. Oleari, *Matching NLO QCD computations with Parton Shower simulations: the POWHEG method*, *JHEP* **11** (2007) 070, [[arXiv:0709.2092](#)].
- [65] S. Catani, M. L. Mangano, P. Nason, and L. Trentadue, *The Resummation of Soft Gluon in Hadronic Collisions*, *Nucl. Phys.* **B478** (1996) 273–310, [[hep-ph/9604351](#)].
- [66] R. Bonciani, S. Catani, M. L. Mangano, and P. Nason, *NLL resummation of the heavy-quark hadroproduction cross-section*, *Nucl. Phys.* **B529** (1998) 424–450, [[hep-ph/9801375](#)].
- [67] P. Nason and B. Webber, *Next-to-Leading-Order Event Generators*, [arXiv:1202.1251](#).
- [68] S. Alioli, P. Nason, C. Oleari, and E. Re, *A general framework for implementing NLO calculations in shower Monte Carlo programs: the POWHEG BOX*, *JHEP* **06** (2010) 043, [[arXiv:1002.2581](#)].
- [69] M. Garzelli, A. Kardos, C. Papadopoulos, and Z. Trocsanyi, *t tbar W and t tbar Z Hadroproduction at NLO accuracy in QCD with Parton Shower and Hadronization effects*, *Accepted for publication in JHEP* (2012) [[arXiv:1208.2665](#)].
- [70] S. Alioli, P. Nason, C. Oleari, and E. Re, *NLO vector-boson production matched with shower in POWHEG*, *JHEP* **0807** (2008) 060, [[arXiv:0805.4802](#)].

-
- [71] A. van Hameren, C. Papadopoulos, and R. Pittau, *Automated one-loop calculations: A Proof of concept*, *JHEP* **0909** (2009) 106, [arXiv:0903.4665].
- [72] U. Baur, A. Juste, D. Rainwater, and L. Orr, *Improved measurement of ttZ couplings at the CERN LHC*, *Phys.Rev.* **D73** (2006) 034016, [hep-ph/0512262].
- [73] F. Halzen, P. Hoyer, and C. Kim, *FORWARD - BACKWARD ASYMMETRY OF HADROPRODUCED HEAVY QUARKS IN QCD*, *Phys.Lett.* **B195** (1987) 74.
- [74] J. H. Kuhn and G. Rodrigo, *Charge asymmetry of heavy quarks at hadron colliders*, *Phys.Rev.* **D59** (1999) 054017, [hep-ph/9807420].
- [75] M. Czakon, C. Papadopoulos, and M. Worek, *Polarizing the Dipoles*, *JHEP* **0908** (2009) 085, [arXiv:0905.0883].
- [76] G. Ossola, C. G. Papadopoulos, and R. Pittau, *CutTools: a program implementing the OPP reduction method to compute one-loop amplitudes*, *JHEP* **03** (2008) 042, [arXiv:0711.3596].
- [77] Z. Bern, L. J. Dixon, D. C. Dunbar, and D. A. Kosower, *Fusing gauge theory tree amplitudes into loop amplitudes*, *Nucl.Phys.* **B435** (1995) 59–101, [hep-ph/9409265].
- [78] A. Brandhuber, S. McNamara, B. J. Spence, and G. Travaglini, *Loop amplitudes in pure Yang-Mills from generalised unitarity*, *JHEP* **0510** (2005) 011, [hep-th/0506068].
- [79] C. Anastasiou, R. Britto, B. Feng, Z. Kunszt, and P. Mastrolia, *Unitarity cuts and Reduction to master integrals in d dimensions for one-loop amplitudes*, *JHEP* **0703** (2007) 111, [hep-ph/0612277].
- [80] G. Ossola, C. G. Papadopoulos, and R. Pittau, *Reducing full one-loop amplitudes to scalar integrals at the integrand level*, *Nucl.Phys.* **B763** (2007) 147–169, [hep-ph/0609007].
- [81] R. K. Ellis, W. Giele, and Z. Kunszt, *A Numerical Unitarity Formalism for Evaluating One-Loop Amplitudes*, *JHEP* **0803** (2008) 003, [arXiv:0708.2398].

- [82] Z. Bern, L. J. Dixon, and D. A. Kosower, *On-Shell Methods in Perturbative QCD*, *Annals Phys.* **322** (2007) 1587–1634, [arXiv:0704.2798].
- [83] G. Ossola, C. G. Papadopoulos, and R. Pittau, *On the Rational Terms of the one-loop amplitudes*, *JHEP* **0805** (2008) 004, [arXiv:0802.1876].
- [84] P. Draggiotis, M. Garzelli, C. Papadopoulos, and R. Pittau, *Feynman Rules for the Rational Part of the QCD 1-loop amplitudes*, *JHEP* **0904** (2009) 072, [arXiv:0903.0356].
- [85] J. Alwall, P. Demin, S. de Visscher, R. Frederix, M. Herquet, *et. al.*, *MadGraph/MadEvent v4: The New Web Generation*, *JHEP* **0709** (2007) 028, [arXiv:0706.2334].
- [86] S. Alioli, P. Nason, C. Oleari, and E. Re, *Vector boson plus one jet production in POWHEG*, *JHEP* **1101** (2011) 095, [arXiv:1009.5594].
- [87] S. Alioli, K. Hamilton, P. Nason, C. Oleari, and E. Re, *Jet pair production in POWHEG*, *JHEP* **1104** (2011) 081, [arXiv:1012.3380].
- [88] S. Dittmaier, P. Uwer, and S. Weinzierl, *NLO QCD corrections to t anti- t + jet production at hadron colliders*, *Phys.Rev.Lett.* **98** (2007) 262002, [hep-ph/0703120].
- [89] S. Dittmaier, P. Uwer, and S. Weinzierl, *Hadronic top-quark pair production in association with a hard jet at next-to-leading order QCD: Phenomenological studies for the Tevatron and the LHC*, *Eur.Phys.J.* **C59** (2009) 625–646, [arXiv:0810.0452].
- [90] K. Melnikov and M. Schulze, *NLO QCD corrections to top quark pair production in association with one hard jet at hadron colliders*, *Nucl.Phys.* **B840** (2010) 129–159, [arXiv:1004.3284].
- [91] T. Sjostrand, S. Mrenna, and P. Z. Skands, *PYTHIA 6.4 Physics and Manual*, *JHEP* **0605** (2006) 026, [hep-ph/0603175].
- [92] G. Corcella, I. Knowles, G. Marchesini, S. Moretti, K. Odagiri, *et. al.*, *HERWIG 6.5 release note*, hep-ph/0210213.

-
- [93] S. Catani, Y. L. Dokshitzer, M. Seymour, and B. Webber, *Longitudinally invariant K_t clustering algorithms for hadron hadron collisions*, *Nucl.Phys.* **B406** (1993) 187–224.
- [94] M. Schulze private communication.
- [95] M. Cacciari and G. P. Salam, *Dispelling the N^3 myth for the k_t jet-finder*, *Phys.Lett.* **B641** (2006) 57–61, [[hep-ph/0512210](#)].
- [96] **Particle Data Group** Collaboration, K. Nakamura *et. al.*, *Review of particle physics*, *J.Phys.G* **G37** (2010) 075021.
- [97] **ATLAS Collaboration** Collaboration, G. Aad *et. al.*, *Combined search for the Standard Model Higgs boson using up to 4.9 fb⁻¹ of pp collision data at $\sqrt{s} = 7$ TeV with the ATLAS detector at the LHC*, *Phys.Lett.* **B710** (2012) 49–66, [[arXiv:1202.1408](#)].
- [98] **CMS Collaboration** Collaboration, S. Chatrchyan *et. al.*, *Combined results of searches for the standard model Higgs boson in pp collisions at $\sqrt{s} = 7$ TeV*, [arXiv:1202.1488](#).
- [99] **ALEPH Collaboration, CDF Collaboration, D0 Collaboration, DELPHI Collaboration, L3 Collaboration, OPAL Collaboration, SLD Collaboration, LEP Electroweak Working Group, Tevatron Electroweak Working Group, SLD Electroweak and Heavy Flavour Groups** Collaboration, *Precision Electroweak Measurements and Constraints on the Standard Model*, [arXiv:1012.2367](#).
- [100] W. Beenakker, S. Dittmaier, M. Kramer, B. Plumper, M. Spira, *et. al.*, *Higgs radiation off top quarks at the Tevatron and the LHC*, *Phys.Rev.Lett.* **87** (2001) 201805, [[hep-ph/0107081](#)].
- [101] W. Beenakker, S. Dittmaier, M. Kramer, B. Plumper, M. Spira, *et. al.*, *NLO QCD corrections to t anti- t H production in hadron collisions*, *Nucl.Phys.* **B653** (2003) 151–203, [[hep-ph/0211352](#)].
- [102] L. Reina and S. Dawson, *Next-to-leading order results for t anti- t h production at the Tevatron*, *Phys.Rev.Lett.* **87** (2001) 201804, [[hep-ph/0107101](#)].

- [103] L. Reina, S. Dawson, and D. Wackerroth, *QCD corrections to associated t anti- t h production at the Tevatron*, *Phys.Rev.* **D65** (2002) 053017, [hep-ph/0109066].
- [104] S. Dawson, L. Orr, L. Reina, and D. Wackerroth, *Associated top quark Higgs boson production at the LHC*, *Phys.Rev.* **D67** (2003) 071503, [hep-ph/0211438].
- [105] M. Garzelli, A. Kardos, C. Papadopoulos, and Z. Trocsanyi, *Standard Model Higgs boson production in association with a top anti-top pair at NLO with parton showering*, *Europhys.Lett.* **96** (2011) 11001, [arXiv:1108.0387]. 14 pages, 9 figures.
- [106] A. Cafarella, C. G. Papadopoulos, and M. Worek, *Helac-Phegas: a generator for all parton level processes*, *Comput. Phys. Commun.* **180** (2009) 1941–1955, [arXiv:0710.2427].
- [107] V. Hirschi, R. Frederix, S. Frixione, M. V. Garzelli, F. Maltoni, *et. al.*, *Automation of one-loop QCD corrections*, *JHEP* **1105** (2011) 044, [arXiv:1103.0621].
- [108] R. Frederix private communication.
- [109] F. Maltoni and T. Stelzer, *MadEvent: Automatic event generation with MadGraph*, *JHEP* **0302** (2003) 027, [hep-ph/0208156].
- [110] M. R. Whalley, D. Bourilkov, and R. C. Group, *The Les Houches Accord PDFs (LHAPDF) and Lhaglu*, hep-ph/0508110.
- [111] S. Dawson, C. Jackson, L. Orr, L. Reina, and D. Wackerroth, *Associated Higgs production with top quarks at the large hadron collider: NLO QCD corrections*, *Phys.Rev.* **D68** (2003) 034022, [hep-ph/0305087].
- [112] S. Alioli, P. Nason, C. Oleari, and E. Re, *NLO Higgs boson production via gluon fusion matched with shower in POWHEG*, *JHEP* **0904** (2009) 002, [arXiv:0812.0578].
- [113] M. Cacciari, G. P. Salam, and G. Soyez, *The Anti- $k(t)$ jet clustering algorithm*, *JHEP* **0804** (2008) 063, [arXiv:0802.1189].

-
- [114] **SM and NLO Multileg Working Group** Collaboration, J. Andersen *et. al.*, *The SM and NLO Multileg Working Group: Summary report*, arXiv:1003.1241.
- [115] C. Oleari and L. Reina, *W +- b b-bar production in POWHEG*, *JHEP* **1108** (2011) 061, [arXiv:1105.4488].
- [116] A. Lazopoulos, K. Melnikov, and F. J. Petriello, *NLO QCD corrections to the production of t anti-t Z in gluon fusion*, *Phys. Rev.* **D77** (2008) 034021, [arXiv:0709.4044].
- [117] A. Lazopoulos, T. McElmurry, K. Melnikov, and F. Petriello, *Next-to-leading order QCD corrections to t anti-t Z production at the LHC*, *Phys. Lett.* **B666** (2008) 62–65, [arXiv:0804.2220].
- [118] **CMS Collaboration** Collaboration, S. Chatrchyan *et. al.*, *Search for new physics in events with same-sign dileptons and b-tagged jets in pp collisions at sqrt(s) = 7 TeV*, arXiv:1205.3933.
- [119] P. Mastrolia, G. Ossola, T. Reiter, and F. Tramontano, *Scattering Amplitudes from Unitarity-based Reduction Algorithm at the Integrand-level*, *JHEP* **08** (2010) 080, [arXiv:1006.0710].
- [120] G. Cullen *et. al.*, *Automated One-Loop Calculations with GoSam*, arXiv:1111.2034.
- [121] F. Petriello, “The estimated uncertainty is about 1.5 %.” private communication.
- [122] T. Sjostrand, P. Eden, C. Friberg, L. Lonnblad, G. Miu, *et. al.*, *High-energy physics event generation with PYTHIA 6.1*, *Comput.Phys.Commun.* **135** (2001) 238–259, [hep-ph/0010017].
- [123] G. Corcella, I. Knowles, G. Marchesini, S. Moretti, K. Odagiri, *et. al.*, *HERWIG 6: An Event generator for hadron emission reactions with interfering gluons (including supersymmetric processes)*, *JHEP* **0101** (2001) 010, [hep-ph/0011363].
- [124] M. Cacciari, G. P. Salam, and G. Soyez, *FastJet user manual*, *Eur.Phys.J.* **C72** (2012) 1896, [arXiv:1111.6097].

- [125] P. Z. Skands, *Tuning Monte Carlo Generators: The Perugia Tunes*, *Phys.Rev.* **D82** (2010) 074018, [arXiv:1005.3457].
- [126] M. Beneke, I. Efthymiopoulos, M. L. Mangano, J. Womersley, A. Ahmadov, *et. al.*, *Top quark physics*, hep-ph/0003033.
- [127] **CMS** Collaboration, *Search for new physics with same-sign isolated dilepton events with jets and missing energy*, . Available on the CERN CDS information server, Tech. Rep. CMS PAS SUS-11-010.
- [128] **CMS** Collaboration, *First measurement of vector boson production associated with top-antitop pairs at 7 tev*, . Available on the CERN CDS information server, Tech. Rep. CMS PAS TOP-12-014.
- [129] P. Nason, *A New method for combining NLO QCD with shower Monte Carlo algorithms*, *JHEP* **0411** (2004) 040, [hep-ph/0409146].
- [130] G. Bevilacqua, M. Czakon, M. Garzelli, A. van Hameren, A. Kardos, *et. al.*, *HELAC-NLO*, arXiv:1110.1499.
- [131] J. M. Campbell and R. K. Ellis, *$t\bar{t}W^{+-}$ production and decay at NLO*, *JHEP* **1207** (2012) 052, [arXiv:1204.5678].
- [132] M. Garzelli, A. Kardos, C. Papadopoulos, and Z. Trocsanyi, *$Z0$ - boson production in association with a top anti-top pair at NLO accuracy with parton shower effects*, *Phys.Rev.* **D85** (2012) 074022, [arXiv:1111.1444].
- [133] J. M. Campbell and R. Ellis, *MCFM for the Tevatron and the LHC*, *Nucl.Phys.Proc.Suppl.* **205-206** (2010) 10–15, [arXiv:1007.3492].
- [134] R. E. J. M. Campbell and C. Williams, “MCFM.”
<http://mcfm.fnal.gov>.
- [135] A. Kardos, Z. Trocsanyi, and C. Papadopoulos, *Top quark pair production in association with a Z-boson at NLO accuracy*, *Phys.Rev.* **D85** (2012) 054015, [arXiv:1111.0610]. 9 pages, 5 figures.
- [136] O. Latunde-Dada, S. Gieseke, and B. Webber, *A Positive-Weight Next-to-Leading-Order Monte Carlo for $e^+ e^-$ Annihilation to Hadrons*, *JHEP* **0702** (2007) 051, [hep-ph/0612281].